UNIVERSIDADE DO ESTADO DE SANTA CATARINA
CENTRO DE CIÊNCIAS TECNOLÓGICAS
PROGRAMA DE PÓS-GRADUAÇÃO EM ENGENHARIA MECÂNICA

VÍTOR SAVAGNAGO

NUMERICAL SIMULATION OF VERTICAL CHURN AND ANNULAR FLOWS

JOINVILLE
2022

Ficha catalográfica elaborada pelo programa de geração automática da Biblioteca Setorial do CCT/UDESC,
com os dados fornecidos pelo(a) autor(a)

Savagnago, Vítor
Numerical Simulation of Vertical Churn and Annular Flows / Vítor Savagnago. -- 2022.
92 p.

Orientador: Marcus Vinícius Canhoto Alves
Coorientador: Rafael Rodrigues Francisco
Dissertação (mestrado) -- Universidade do Estado de Santa Catarina, Centro de Ciências Tecnológicas, Programa de Pós-Graduação em Engenharia Mecânica, Joinville, 2022.

1. Computational Fluid Dynamics. 2. Churn flow. 3. Annular flow. I. Canhoto Alves, Marcus Vinícius. II. Rodrigues Francisco, Rafael. III. Universidade do Estado de Santa Catarina, Centro de Ciências Tecnológicas, Programa de Pós-Graduação em Engenharia Mecânica. IV. Titulo.

VÍTOR SAVAGNAGO

NUMERICAL SIMULATION OF VERTICAL CHURN AND ANNULAR FLOWS

Dissertação apresentada ao Programa de Pós-Graduação em Engenharia Mecânica, do Centro de Ciências Tecnológicas da Universidade do Estado de Santa Catarina, como parte dos requisitos necessários para a obtenção do título de Mestre em Engenharia Mecânica.
Área de concentração: Modelamento e Simulação Numérica

Orientador: Prof. Dr. Marcus Vinícius Canhoto Alves.
Coorientador: Prof. Dr. Rafael Rodrigues Francisco.

JOINVILLE

2022

VÍTOR SAVAGNAGO

NUMERICAL SIMULATION OF VERTICAL CHURN AND ANNULAR FLOWS

Dissertação apresentada ao Programa de Pós-Graduação em Engenharia Mecânica, do Centro de Ciências Tecnológicas da Universidade do Estado de Santa Catarina, como parte dos requisitos necessários para a obtenção do título de Mestre em Engenharia Mecânica.
Área de concentração: Modelamento e Simulação Numérica

BANCA EXAMINADORA

Prof. Dr. Marcus Vinícius Canhoto Alves
Universidade do Estado de Santa Catarina, UDESC
(Presidente/orientador)

Membros:

Prof. Dr. Oscar Mauricio Hernandez Rodriguez
Universidade de São Paulo, USP

Prof. Dr. Rigoberto Eleazar Melgarejo Morales
Universidade Tecnológica Federal do Paraná, UTFPR

Joinville, 17 de fevereiro de 2022.

ACKNOWLEDGEMENTS

This work is dedicated to my parents, who made it all possible, and to all my family for the support. To my girlfriend, Mariana, for the love and companionship during these years. To all my friends, for the great partnership.

To my advisor and mentor, Professor Marcus, for the trust and all the shared knowledge. To the professors and colleagues from PPGEM-UDESC, especially Willian, for all insights, discussions, and coffees shared.

This research was supported by Santa Catarina State University; "Fundação de Amparo à Pesquisa e Inovação do Estado de Santa Catarina (FAPESC)", through the concessions 2019TR000779, 2019TR000783, and 2019TR000843; and the scholarship FAPESC 05/2019; "Conselho Nacional de Desenvolvimento Científico e Tecnológico (CNPq)" grant 433820/2018-7. This worked used the computational resources of "Centro Nacional de Processamento de Alto Desempenho em São Paulo (CENAPAD-SP)" and "Fundação de Amparo à Pesquisa do Estado de São Paulo (FAPESP)".

ABSTRACT

Gas-liquid flows are encountered in many industrial processes, such as the oil and gas industry, nuclear reactors, heat exchangers, and others. These flows are divided in flow patterns, according to the structure of the interface between the two phases. Important flow parameters, such as pressure gradient and void fraction, depend on the existing flow pattern. Thus, predicting these patterns and the flow parameters at each of them is crucial on industrial projects. In this research, numerical simulations of churn and annular flows, and the transition between them, are conducted. Simulations are performed in the free open-source software OpenFOAM®, using a hybrid methodology, which combines the Eulerian two-fluid model with the volume-of-fluid (VOF) method for interface capturing. An analysis of the ability of the method to predict flow parameters and characteristics is performed. The influence of the maximum Courant number of the simulation, the inlet geometry, and turbulence modelling in the results is evaluated. Also, differences between versions 7 and 9 of the OpenFOAM® software are addressed. In general, the methodology can capture some physical characteristics of churn and annular flows, as the wavy interface and droplet formation. However, some unphysical phenomena are seen, such as liquid film pulverization. Besides that, droplet, and filament formation are underestimated by the simulations, and the oscillatory liquid behavior, characteristic of churn flows, is not captured. This work shows that inlet geometry significantly influences the flow void fraction and pressure gradient, and that a trueful representation of the experimental test section is crucial for obtaining accurate results. It is shown that the use of extremely small Courant numbers is not necessary, as it might not provide better results, despite requiring much longer times. From the analysis of turbulence models, considering water as a laminar fluid and modelling air with the $k-\omega$ SST model has provided the best results from the models tested when compared to experimental data.

Keywords: Computational Fluid Dynamics, churn flow, annular flow.

RESUMO

Escoamentos gás-líquido podem ser encontrados em diversos processos industriais, como na indústria de óleo e gás, em reatores nucleares, trocadores de calor, entre outros. Esses escoamentos são divididos em padrões, de acordo com a estrutura da interface entre as fases. Parâmetros importantes desses escoamentos, como o gradiente de pressão e a fração de vazio, dependem do padrão de escoamento existente. Portanto, prever a ocorrência desses padrões e os parâmetros do escoamento em cada um deles é crucial em projetos industriais. Nesse trabalho são realizadas simulações numéricas de escoamentos nos padrões agitante e anular, e na transição entre eles. As simulações são realizadas no programa OpenFOAM®, utilizando uma metodologia híbrida que combina o método Euleriano de dois fluidos com o método de volume-of-fluid (VOF) para acompanhamento da interface. Analisa-se a capacidade do método de prever os parâmetros e características do escoamento. A influência do número de Courant, da geometria de entrada, e da modelagem da turbulência nos resultados é avaliada. Em geral, o método é capaz de capturar alguns fenômenos do escoamento nos padrões agitante e anular, como a interface ondulada e a formação de gotas. Entretanto, alguns fenômenos não-físicos são observados, como a pulverização do filme líquido. Além disso, a formação de gotas e filamentos é subestimada nas simulações, e a característica oscilatória de escoamentos no padrão agitante não é observada. A geometria de entrada utilizada influencia significativamente os resultados das simulações; uma representação correta da geometria desejada é crucial para a obtenção de bons resultados. É mostrado também que valores muito baixos para o número de Courant não são necessários, já que não fornecem necessariamente melhores resultados, apesar de requererem simulações muito mais demoradas. Quanto à turbulência, simulações considerando água como um fluido laminar e modelando o ar com o modelo $k-\omega$ SST forneceram os melhores resultados dentre os modelos testados.

Palavras chaves: Fluidodinâmica computacional, escoamento agitante, escoamento anular.

LIST OF FIGURES

LIST OF TABLES

LIST OF ABBREVIATIONS

CFD	Computational Fluid Dynamics;
CFL	Courant-Friedrichs-Lewis;
DNS	Direct Numerical Simulation;
ID	Internal diameter;
LOCA	Loss Of Coolant Accidents;
MULES	Multidimensional Universal Limiter with Explicit Solution;
PDF	Probability Density Function;
PISO	Pressure-Implicit Splitting of Operators;
RANS	Reynolds Average Navier-Stokes;
SCMM	Split Coefficient Matrix Method;
SST	Shear Stress Tensor;
VOF	Volume-of-Fluid.

LIST OF SYMBOLS

A	Area;
C	Droplets concentration;
C_α	Compression coefficient of VOF;
C_D	Drag coefficient;
Co	Courant number;
C_W	Wall lubrication coefficient;
D	Pipe diameter;
d_b	Bubble diameter;
Eo	Eotvos number;
$\vec{F}_D$	Drag forces;
$\vec{F}_S$	Surface tension force;
$\vec{F}_W$	Wall lubrication forces;
$\vec{g}$	Acceleration of gravity;
I	Turbulence intensity;
j	Superficial velocity;
j^*	Dimensionless superficial velocity;
k	Turbulent kinetic energy;
$\dot{m}$	Mass flux;
$\vec{M}_k$	Interfacial momentum transfer to phase k;
$\hat{n}_W$	Vector normal to the wall;
p	Pressure;
q	Volumetric flow rate;
Re	Reynolds number;
S	Dimensionless interfacial shear stress group;
t	Time;
$\vec{u}$	Velocity;
$\vec{u}_c$	Compression velocity;
$\vec{U}_r$	Relative velocity;
U_m	Mixture velocity;
U_g^*	Dimensionless gas velocity;

V	Volume;
y_W	Distance to the wall;
α	Volumetric fraction;
δ	Film thickness;
Δx	Mesh cell size;
ε	Turbulent dissipation rate;
γ	Normalized volumetric fraction gradient;
κ	Local interface curvature;
μ	Dynamic viscosity;
ρ	Density;
σ	Surface tension;
τ_i	Interfacial shear stress;
ω	Turbulent specific dissipation rate.

Subscripts

c	Continuous phase;
d	Dispersed phase;
g	Gas phase;
i	Coordinates x, y, z;
k	Phase k, gas or liquid;
l	Liquid phase.

TABLE OF CONTENTS

1 INTRODUCTION

Two-phase gas-liquid flows are encountered in many different applications, such as the oil and gas industry, nuclear reactors, thermal and chemical industry, among others. Gas-liquid flows in ducts assume different patterns, according to the topological structure of the interface between phases. In vertical pipes, the main patterns are bubble, slug, churn, and annular flow. Important flow parameters, such as pressure gradient, void fraction, and phase velocity, highly depend on the flow pattern. Thus, the correct prediction of these patterns is crucial in projecting processes and equipment that work under gas-liquid flow conditions.

Most existing methods for the prediction of flow pattern and determination of flow parameters are based on empirical data, which cannot be generalized to a wide range of applications, or have significant simplifications, usually considering the flow one-dimensional and in steady state. With the increase of computational capacities in the last decades, Computational Fluid Dynamics (CFD) methodologies have been developed to simulate gas-liquid flows, with less simplifications. The volume-of-fluid (VOF) method with interface capturing, for instance, provides a way of accompanying the interface between phases and allows the visualization of free-surface or segregated flows, in which interface capturing is crucial. On the other hand, for dispersed flows, where many small particles are present and interface capturing cannot be accomplished with a viable computational mesh, an Eulerian-Eulerian approach can be used, solving the transport equations for both phases separately. A Lagrangian-Eulerian approach, in which the flow of dispersed particles is tracked with a Lagrangian model, is also frequently used.

However, gas-liquid flows present a challenge even to complex CFD models due to their complex characteristics and variety of flow patterns, which might present dispersed or segregated phase distributions, thus requiring a previous determination of flow pattern for the selection of an adequate CFD method. Besides that, complex patterns such as churn and annular flow present both dispersed and segregated characteristics simultaneously (TOCCI, 2016). These patterns are widely seen in engineering processes, and the transition between them – from annular to churn flow, mainly – can cause problems such as liquid loading in gas wells and Lost of Coolant Accidents (LOCA) in nuclear reactors. This drives the development of efficient methods to determine flow parameters and pattern transition, which is a transient phenomenon and therefore cannot be accurately predicted with steady-state models (ALVES et al., 2017).

To overcome the challenge of simulating complex gas-liquid systems, a hybrid method has been developed, combining the Eulerian-Eulerian approach with the interface capturing method (WARDLE; WELLER, 2013). This hybrid method applies the interface capturing in regions of sharp interface, where its knowledge is crucial, and applies a pure Eulerian-Eulerian method where the interface is too small to be captured by the computational mesh used.

The hybrid methodology has been implemented in the multiphaseEulerFoam algorithm in the software OpenFOAM®, which is a free open-source program for CFD applications. It might be a solution for the simulation of complex multiphase systems, such as gas-liquid vertical flows, which are the scope of this work.

1.1 RESEARCH OBJECTIVES

The present research intends to investigate numerically gas-liquid flows in the churn and annular patterns, as well as their transition, with three-dimensional transient simulations. The hybrid methodology, which combines the Eulerian-Eulerian and VOF methods, is used in the simulations, which are compared to experimental data available in literature.

Three different gas and liquid mass fluxes are simulated, corresponding to the churn and annular patterns, and their transition. These flow patterns were visualized in the experiments from Govan et al. (1991), and the simulations are performed with the same mass fluxes as in the experiments. The geometry used in the simulation intends to reproduce the liquid inlet and the pipe length from the test section of the Govan et al. (1991) experiments. Results for pressure gradient and void fraction obtained from the simulations are compared with the experimental data. To address the influence of the inlet region in the flow parameters, results are also compared with the simulations performed by Freitas (2021), that reproduced only the upper region of the Govan et al. (1991) experiments, without considering the porous-wall liquid inlet. Physical characteristics of the flows in different patterns and gas-liquid phenomena are analyzed, the maximum Courant number of the simulations investigated, and a comparison of some turbulence modeling options available in OpenFOAM® is performed. Finally, a preliminary discussion on the influence of different drag coefficient and wall lubrication models is conducted.

This work is part of a research project developed in the Mechanical Engineering Department of the Santa Catarina State University, which intends to obtain more detailed information about churn and annular flows, the transition between them and how to best simulate the transient 3D behavior of these flow patterns.

1.2 STRUCTURE OF THE DISSERTATION

This work is divided in seven chapters as follows: the next chapter presents a literature review; the third and fourth chapters bring the numerical modelling of the gas-liquid flow and numerical simulation setup; chapters five and six present the results obtained with the simulations presented and a discussion of these results considering the Govan et al. (1991) data and the overall physical and topological behavior of the flow patterns. Chapter seven brings concluding remarks and recommendations for future work.

2 LITERATURE REVIEW

This chapter provides a literature review on the research subject. First, two-phase gas-liquid flow parameters, fundamentals and patterns are addressed. Then, the main experimental works on churn and annular flows are presented, with a special focus on the experiments performed by Govan et al. (1991), which is taken as the main reference in this research for results comparison. Finally, an evolution on numerical works and the state-of-art in two-phase flow simulations are shown.

2.1 MULTIPHASE FLOW PARAMETERS

Multiphase flows are characterized by having more than one macroscopically distinguishable phase. In this section, some important parameters on the analysis of multiphase flow are presented, based mainly on the definitions proposed by Rosa (2012) and Michaelides, Crowe and Schwarzkopf (2015).

2.1.1 Phase Velocities and Superficial Velocities

The instantaneous velocity of phase k, U_k, is given as the ratio between the volumetric flow rate of the phase, q_k, and the cross-sectional area occupied by the phase, A_k.

$$u_k = \frac{q_k}{A_k} = \frac{\dot{m}_k}{\rho_k A_k} \tag{1}$$

The terms $\dot{m}_k$ and ρ_k represent the mass flow rate and density of phase k, respectively.

The superficial velocity of phase k, j_k, represents the velocity that the phase would have if it flowed alone in the pipe.

$$j_k = \frac{q_k}{A} = \frac{\dot{m}_k}{\rho_k A} \tag{2}$$

A dimensionless superficial gas and liquid velocity can be obtained with the superficial velocity as shown in equations 3 and 4, where g, D, ρ_l and ρ_g are the acceleration of gravity, the pipe diameter and the liquid and gas densities, respectively.

$$j_g^* = j_g \sqrt{\frac{\rho_g}{gD(\rho_l - \rho_g)}} \tag{3}$$

$$j_l^* = j_l \sqrt{\frac{\rho_l}{gD(\rho_l - \rho_g)}} \tag{4}$$

2.1.2 Volumetric Fraction

The volumetric fraction of the phase k, α_k, represents the ratio between the volume occupied by the phase, V_k, within a volume V (MICHAELIDES; CROWE; SCHWARZKOPF, 2015).

$$\alpha_k = \frac{V_k}{V} \tag{5}$$

This parameter can also be referred to as the probability of occurrence of each phase in a volume or cross-sectional area (ROSA, 2012). It can be calculated for a flow in a pipe as the ratio between the cross-sectional area occupied by the phase, A_k, and the total cross-sectional area of the pipe, A.

$$\alpha_k = \frac{A_k}{A} \tag{6}$$

Considering a two-phase gas-liquid system, the sum of the volumetric fraction of the gas, α_g, usually referred as void fraction, and the volumetric fraction of the liquid, α_l, equals 1, as both phases constitute the whole system.

$$\alpha_g + \alpha_l = 1 \tag{7}$$

For a general multiphase system, with n phases, the sum of the volumetric fractions of all phases equals 1.

$$\sum_{k=1}^{n} \alpha_k = 1 \tag{8}$$

2.1.3 Mixture Velocity

The mixture velocity can be defined as the sum of the superficial velocities of all phases. For a gas-liquid flow:

$$U_m = j_g + j_l \tag{9}$$

The addressed parameters are the most important in the analysis performed in this research. More parameters are presented in Rosa (2012) and Michaelides, Crowe and Schwarzkopf (2015).

2.2 VERTICAL GAS-LIQUID FLOW PATTERNS

Gas-liquid flows are present, under different conditions, in several engineering processes, such as the oil and gas industry, heat exchangers (evaporators and condensers), nuclear reactors, among other relevant applications. These flows are divided in flow patterns, characterized by the different morphological structure of each phase (interfacial topology). The spatial distribution of the phases depends on fluid properties, such as viscosity and density, and on the interaction between gravity, inertia, and buoyant forces on the flow (MICHAELIDES; CROWE; SCHWARZKOPF, 2015). The most usual definition of flow patterns in vertical flow is the one shown in Figure 1, where the flow is divided in bubble, slug, churn, and annular flow patterns.

Bubble flow is characterized by the presence of small gas bubbles in a continuous liquid core (MCQUILLAN; WHALLEY, 1985). Slug flow arises from the bubble flow with the increase in gas mass flow rate, which enhances the number of bubbles and causes coalescence. It is characterized by the alternate flow of large bullet-shaped gas bubbles, called Taylor bubbles, and liquid slugs. Taylor bubbles, which have a similar diameter as the pipe, are surrounded by a descending liquid film which often contain small bubbles (AZZOPARDI; HILLS, 2003; TAITEL; BARNEA; DUKLER, 1980).

Figure 1 – Upward vertical gas-liquid flow patterns.

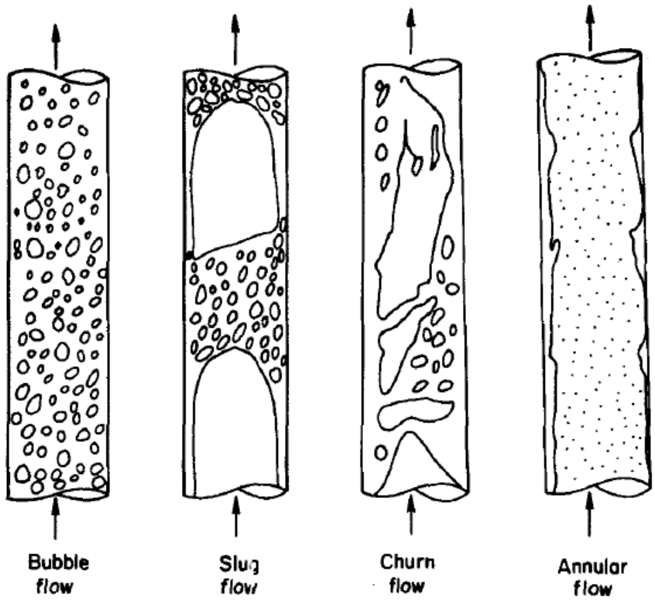

Source: Taitel, Barnea and Dukler (1980).

Churn flow is a chaotic, disordered pattern, that emerges at higher gas velocities, with the liquid film reversal and the Taylor bubbles breakdown. It is characterized by an oscillatory liquid movement, i.e., the liquid film, which flowed downwards in slug flow, flows alternately upwards and downwards, and the presence of liquid drops and filaments which arise from the increase in interfacial friction (AZZOPARDI; HILLS, 2003).

Annular flow is characterized by a continuous gas core, surrounded by a liquid film. Small drops or filaments of liquid can flow upwards entrained in the gas core. It is a turbulent flow, and the interface between gas core and liquid film is wavy (MICHAELIDES; CROWE; SCHWARZKOPF, 2015).

Another pattern frequently seen in gas-liquid systems is the countercurrent annular flow. In this pattern, a liquid film flows downwards, around an ascending gas core (BHARATHAN; WALLIS, 1983). Here the interface between phases is also wavy, causing challenges for the complete understanding of interface dynamics (TEKAVČIČ; KONČAR; KLJENAK, 2016; ZABARAS; DUKLER, 1988).

There is little consensus in literature on the matter of flow patterns. Some authors use different names for the same patterns, while other consider a greater number of patterns, or subdivisions to the presented ones. The spherical cap, for instance, which would lie between the bubble and slug flows, can be found as a flow pattern (ROSA, 2012) or as transition between patterns (MICHAELIDES; CROWE; SCHWARZKOPF, 2015). Bubble flow can also be further divided into dispersed and discrete bubbles (MICHAELIDES; CROWE;

SCHWARZKOPF, 2015; ROSA, 2012). In the former, bubbles are spherical, with uniform size and straight trajectories. The latter have non-uniform size, distorted form, and paths that collide.

Even churn flow has been widely considered as the transition between slug and annular flow, and not as a pattern itself (MAO; DUKLER, 1993; TAITEL; BARNEA; DUKLER, 1980). Churn flow can also be divided into “churn-slug” and “churn-annular” flow. As this pattern happens in a wide range of gas flow rates, presenting characteristics similar to slug flow for the lower end of this range, and similar to annular flow at the higher end, this might be an accurate way of describing these flows, allowing a more realistic modelling (HEWITT; JAYANTI, 1993).

The divergences on pattern description began due to difficulties on flow observation. At high velocities, visualization of the flow characteristics inside a tube is difficult. Also, in wider tubes, only the near-wall region can be easily observed (AZZOPARDI; HILLS, 2003). Only with more advanced instrumentation for obtaining void fraction, velocity and pressure gradient, the flow characteristics became more detailed. X-ray measurements of void fraction with a Probability Density Function (PDF) treatment provided good results for a quantitative determination of flow patterns (JONES; ZUBER, 1975). Costigan and Whalley (1997) showed that the PDF is useful for obtaining signature characteristics of different flow patterns, which makes this method still useful for pattern prediction.

Even with instrumentation developments, flow pattern transitions models are still not of general consensus. These transitions are often estimated with flow pattern maps, which provide regions in which each pattern occur, as function of flow and fluid properties. Figure 2 shows one of these flow pattern maps, provided by Hewitt and Roberts (1969). Azzopardi and Hills (2003), Rosa (2012) and Michaelides, Crowe and Schwarzkopf (2015) provide more details on this matter.

A vast amount of research can be found on pattern transition. Divergencies on the mechanisms involved in the transition between slug and churn flow, countercurrent annular flow and churn flow, and churn and annular flow occur due to the difficulties in visualizing and understanding these phenomena. This results in different possible transition criteria.

The transition between churn and annular flows can be considered as the point of flow reversal, at which there is no more oscillatory movement of the liquid; the point of minimum pressure gradient, as can be seen in Figure 3; the point of zero average wall shear stress; or when local wall shear stress becomes continuously positive, which can be considered analogous to the flow reversal criterion, as continuously positive wall shear stress occur when flow is entirely upwards (ALVES, 2014).

Figure 2 – Flow pattern map for gas-liquid vertical upward flow.

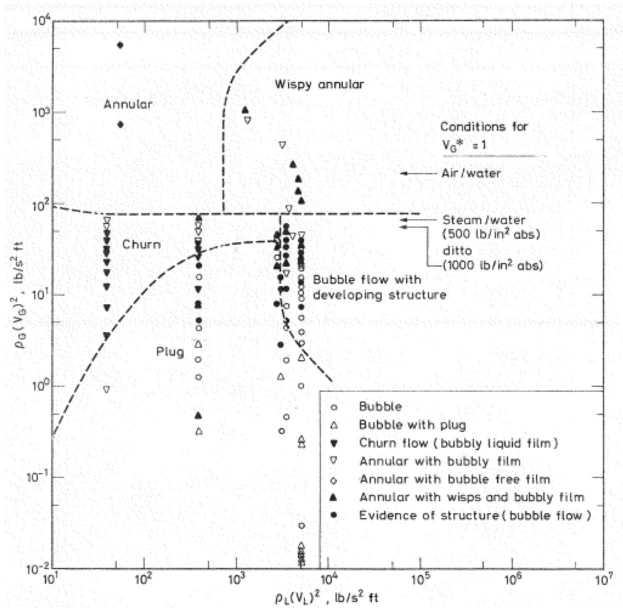

Source: Hewitt and Roberts (1969).

Figure 3 – Dimensionless pressure gradient and flow pattern as function of dimensionless air flowrate.

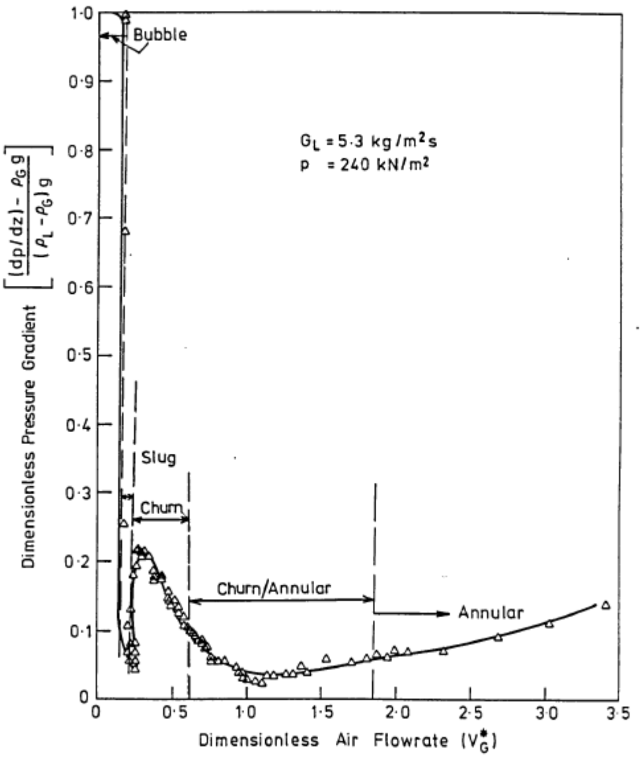

Source: Owen (1986).

Transition between slug and churn flow – or between countercurrent annular flow and churn flow – occur with the onset of the flooding phenomenon, i.e., the point at which the descending liquid film that circulates the Taylor bubble – or the gas core, in countercurrent annular flow – starts moving upwards. This causes the oscillatory movement of the liquid, characteristic of churn flow. There is no general agreement on the mechanisms for the occurrence of flooding, as different models have been proposed (GOVAN et al., 1991; ZABARAS; DUKLER, 1988).

Important properties of gas-liquid flows, such as void fraction, pressure gradient, superficial velocities and heat transfer coefficients depend directly on the flow pattern. Thus, the determination and detailed knowledge of each pattern is crucial in projecting engineering processes.

2.3 EXPERIMENTAL WORKS ON CHURN AND ANNULAR FLOW

Many experimental works have been performed to investigate properties of gas-liquid flows. Research on annular flow started on the early decade of 1960, with simple analytical or empirical models for modelling different two-phase flow parameters, such as film thickness and flow rate, pressure gradient, shear stress, droplets entrainment and deposition, among others (ALVES, 2014).

Initial models involved the use of a triangular relationship, which interrelates the film thickness, liquid flow rate in the film and pressure gradient (HEWITT, 1961). Hewitt and Hall-Taylor (1970) present different forms of triangular relationships, most considering an ideal annular flow, i.e., a flow in which all the liquid flows in the film, without entrainment in the gas core.

Various models can be found for droplet entrainment and deposition. Hutchinson and Whalley (1973) proposed an entrainment correlation considering that the shear stress in the interface dominates the phenomenon of droplets formation and entrainment, although various mechanisms influence the interaction between phases. Their results, which are shown in Figure 4, indicate this consideration might be accurate, as they were able to relate the concentration of droplets in the gas core, C, with the dimensionless group $S = \tau_i \delta / \sigma$, with τ_i, δ and σ being the interfacial shear stress, the film thickness, and the surface tension respectively. This consideration also based the empirical correlation for droplet entrainment proposed by Whalley and Hewitt (1978), who also provide a droplet deposition rate correlation, considering this parameter proportional to a deposition coefficient, which depends on physical properties of the fluids, and to the core droplets concentration. Dallman (1979) provide another correlation, introducing the concept of critical film mass flow rate, below which no entrainment is considered.

Figure 4 – Effect of dimensionless group *S* on the concentration of entrained droplets in the gas core.

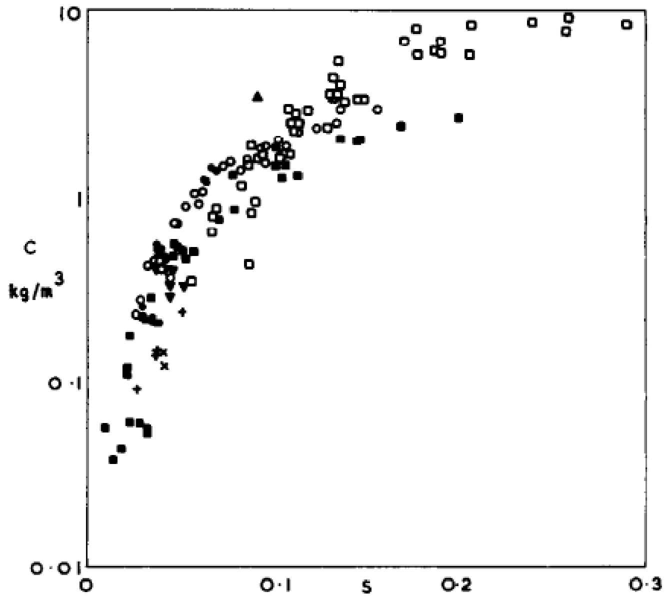

Source: Hutchinson and Whalley (1973).

Interfacial shear stress in annular flow have been addressed since late 1960's. Initially, models considered friction proportional to liquid film thickness, which acted as an equivalent pipe roughness (WALLIS, 1969; WHALLEY; HEWITT, 1978). Different models have been proposed to consider the turbulence generated at the liquid film (DOBRAN, 1983; JENSEN, 1987) and by the liquid droplets (OWEN, 1986).

Interface dynamics between liquid film and gas core, and characteristics of the disturbance waves have also been widely studied (AZZOPARDI, 1986; HALL TAYLOR, 1967). Owen (1986) provide a thorough description of models and correlations for determination of various properties of annular flow.

Antal, Lahey and Flaherty (1991), Tomiyama et al. (1998) and Frank (2005) proposed different models for the wall lubrication forces, which is responsible for driving bubbles away from the pipe walls. In general, wall lubrication models consider a dispersed flow, but can be adapted to other patterns.

Research on churn flow is much scarcer than on annular flow. The complexity of this pattern and difficulty on understanding the mechanisms involved in it resulted in models that are not of general agreement. Different models for the onset of churn flow have been proposed, considering it an extension of slug flow (MAO; DUKLER, 1993), an entry region phenomenon, i.e., a pattern seen in near-entry regions associated with slug flow along the pipe (TAITEL; BARNEA; DUKLER, 1980), a phenomenon strictly associated with the flooding phenomenon (GOVAN et al., 1991; MCQUILLAN; WHALLEY, 1985), among other approaches. Investigations on churn flow properties, such as pressure gradient, void fraction and shear stress have also been performed (GOVAN et al., 1991; MAO; DUKLER, 1993). Jayanti and Brauner (1994) provide a detailed review of the main studies available until mid-1990’s on churn flow, addressing the transition between patterns, the conditions under which churn flow exists, and a model for the prediction of pressure gradient and holdup.

In the last decades, many experimental works have been performed on annular and churn flow, increasing the availability of data on these patterns. Hewitt and Govan (1990) performed and extensive analysis of 32 sources to provide correlations for deposition and entrainment rates in annular flow. Nigmatulin et al. (1996) provided new correlations based on the ones presented by Hewitt and Govan (1990), including a term for the gas core velocity. This approach was also used by Kataoka, Ishii and Nakayama (2000), who presented a correlation for the entrainment rate, taking into account the momentum flux in the gas core. Each of these correlations present more accurate results when compared to the dataset that originated them, precluding definitive conclusions on which should be used.

Okawa and Kataoka (2005) presented new correlations for entrainment and deposition rates. Differently of the primary models on deposition rates (OWEN, 1986), the authors considered that, at low concentrations, deposition was more influenced by the gas velocity than the concentration of droplets, while, at high concentrations, deposition depended on the concentration. Simpler correlations for entrained fraction have also been presented, without the need for separate correlations for entrainment and deposition (CIONCOLINI; THOME, 2010; SAWANT; ISHII; MORI, 2009).

Wolf, Jayanti and Hewitt (2001) investigated flow development in annular flow, by performing experiments in long pipes with 10.8 meters (m) of length, and 31.8 milimiters (mm) of internal diameter (ID). Figure 5 shows the dimensionless pressure gradient at different axial distances of the pipe inlet, for air mass fluxes of (a) 71 kg/m² and (b) 154 kg/m², at different liquid mass fluxes. It can be seen that for low air and liquid mass fluxes, full development is reached at a length of near 100 diameters, while for higher air and liquid mass fluxes, full development is reached much farther from the pipe inlet, which is in accordance to the results from Brown, Jensen and Whalley (1975). Similar resuls can be found for wall shear stress, film flow rate and film thickness, although film flow rate reaches full development at lower lengths than pressure gradient, and film thickness present wider variations than the other parameters.

Figure 5 – Variation of dimensionless pressure gradient with axial distance for air mass fluxes of (a) 71 kg/m² and (b) 154 kg/m² at different liquid mass fluxes.

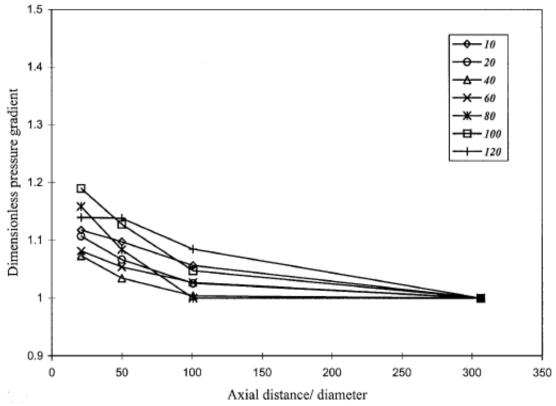

(a)

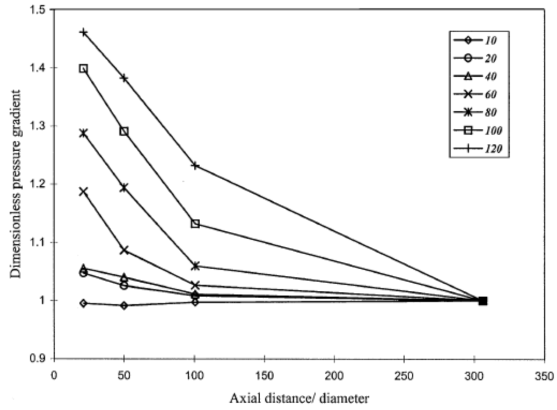

(b)

Source: Wolf, Jayanti and Hewitt (2001).

Figure 6 – Measured pressure gradient as function of superficial gas and liquid velocities.

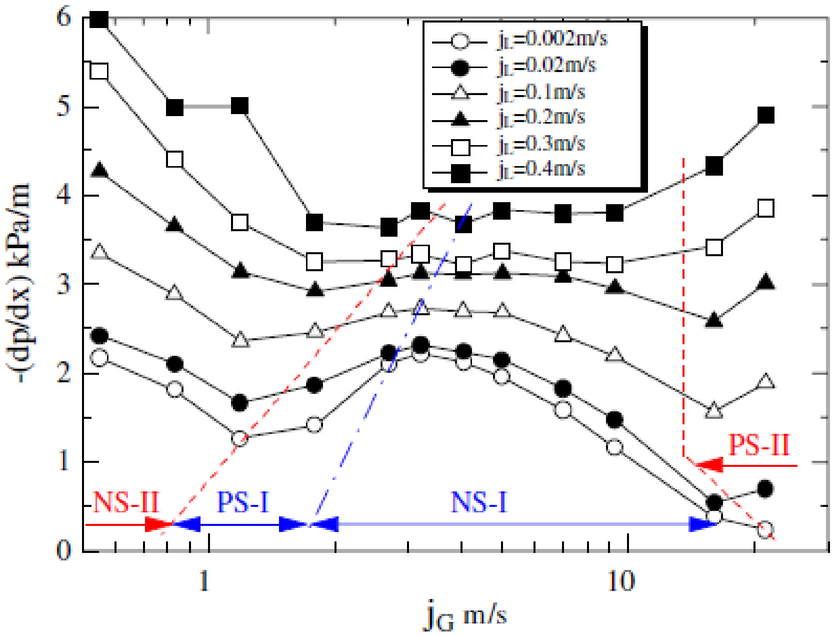

Source: Sawai et al. (2004).

Sawai et al. (2004) investigated interface behavior in churn flow. Measurements of interfacial pressure gradient showed that previous correlations significantly underestimated this parameter. Figure 6 shows the measured pressure gradient for different superficial gas and liquid velocities, which was used to calculate interfacial pressure gradient. The regions PS-II and NS-II correspond to annular and slug flow, respectively, while PS-I and NS-I correspond to churn flow. In slug flow, pressure gradient decreases with the increase on gas superficial velocity, due to the decrease in the mixture density. In the onset of churn flow, because of the change in interface dynamics, pressure gradient increases with the increase in superficial gas velocity. In terms of interface structure, churn flow was characterized by the oscillatory liquid movement and the presence of flooding-type large waves, which was the dominant factor on the interfacial pressure gradient. A correlation for the frictional pressure gradient is proposed by the authors.

Belt, van't Westende and Portela (2009) provide improvements to the Walli's correlation for the interfacial friction in annular flow, which considers the liquid film as a pipe roughness for predicting friction as in a single-phase flow. The authors show that this roughness is proportional to the wave height. Belt et al. (2010) provides a description of interfacial waves in vertical annular flow. Characteristics of these waves and measurements of their length, height, velocity and frequency are presented.

Ahmad et al. (2010) performed a series of experiments to determine droplet entrainment in churn flow, developing a method for predicting the entrained fraction at the onset of annular flow. Authors accompanied the entrainment processes from the onset of churn flow into the annular pattern. This work was later basis for the model proposed by Wang, Bai and Ma (2013) for droplet entrainment in churn flow.

Waltrich, Falcone and Barbosa (2013) studied the development of annular, churn and slug flows in 42 m long pipes, with 48 mm ID. Through Probability Density Functions (PDF) of liquid holdup, the authors were able to visuallize that churn flow occur far from the pipe inlet, contradicting the argument that it is a near-entry region effect (TAITEL; BARNEA; DUKLER, 1980), although PDF of holdup in the non-developed region of slug flow were very similar to the churn flow. Authors showed also that liquid holdup varies significantly with axial distance for a high liquid mass flux (310 kg/m^2s), while reaching development early for a low liquid mass flux (19 kg/m^2s).

Aliyu et al. (2017) carried out experiments to investigate interfacial friction on annular flow in 101.6 mm ID pipes. The authors evaluated several correlations available in litetature, most of them proposed for pipes with small diameters, which presented significant discrepancies. A new correlation have been proposed, introducing a dependance of the core Reynolds and Froude number, which provides better results for thicker films.

Wang, Ye and Bai (2017) investigated droplet entrainment in churn flow in 19 mm ID pipes. The authors provide images of the flow, allowing the visualization of the interface. Mechanisms for the generation of droplets are discussed, and the authors propose a correlation for droplet size prediction by adjusting to churn flow conditions the correlation proposed by Azzopardi (2006), originally for annular flow. Zhang et al. (2019) also studied droplet entrainment, proposing five different mechanisms for droplet formation, and indicating that gas velocity is the main factor for droplet entrainment, while the liquid velocity can be neglected. The authors provide also the distribution of droplet size and velocity under different flowrates, and show that momentum transfer between gas core and droplets is higher in annular flow than in churn flow.

2.3.1 The Govan et al. (1991) Experiments

The experiments performed by Govan et al. (1991) are of particular interest in the present research, as it intends to reproduce part of their test section and to simulate some of the flow conditions analyzed by the authors, comparing results with the experiments. The authors performed a series of experiments to analyze the flooding phenomenon and churn flow. Their work can be divided in two parts, namely experiments on flooding, and churn flow experiments. In the first part, the authors determine the flooding point, i.e., the gas flowrate at which the liquid film starts flowing upwards, for different liquid flowrates, and for different liquid outlet geometries, also providing a qualitative interpretation of the mechanisms involved in flooding. In the second part, churn flow properties were investigated. Authors provide measures of pressure gradient, holdup, and shear stress for different flowrates.

The test section used on the Govan et al. (1991) experiments can be seen in Figure 7. It consists of a 31.8 mm ID pipe. Air flows into the pipe through a 10 mm ID inlet, which allows the outflow of any liquid that might reach the inlet. The liquid inlet consists of a porous wall of 50 mm length. Before flow reversal, i.e., while the film still flows downwards, it leaves the pipe through an outlet sinter of 75 mm length. After flooding, liquid leaves the pipe along with the air at the pipe outlet. The region right above the liquid inlet is made of acrylic resin, allowing the visualization of the flow, which is used to determine the flooding point. Above the inlet two simultaneously closing valves are positioned with 0.92 m apart from each other, for measurements of void fraction and liquid holdup. Devices for pressure measurement, separated by 846 mm, are used to provide the pressure gradient. Pressure is maintained at 1.33 bar at the point ‘P’ in the test section using valve ‘V2’. Experiments were conducted with air and water.

Figure 7 – Experimental test section used in the experiments from Govan et al. (1991).

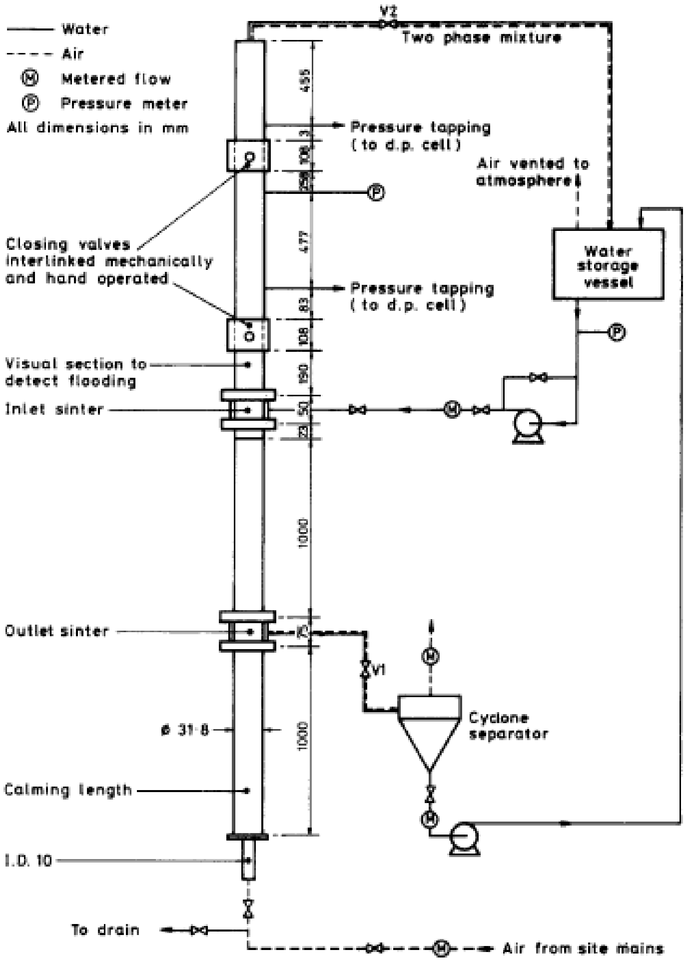

Source: Govan et al. (1991).

Measures for pressure gradient under different flowrates are shown in Figure 8. Figure 9 shows the measured liquid holdup. Curves were interpolated for liquid flowrates of 47.7 and 31.8 kg/m²s.

Values in brackets correspond to liquid up flow, which is lower than the inlet flowrate when liquid down flow is present, before flow reversal. In the points without brackets, upwards flow is equal to the injection flowrate, corresponding to flows above flow reversal point. Data obtained for flow reversal in their experiments agree with the Wallis (1969) criterion, $U_g^* = 1$, represented by the straight vertical line, which is often used as transition criterion between churn and annular flow.

Figure 8 – Measured pressure gradient for different water and air mass fluxes.

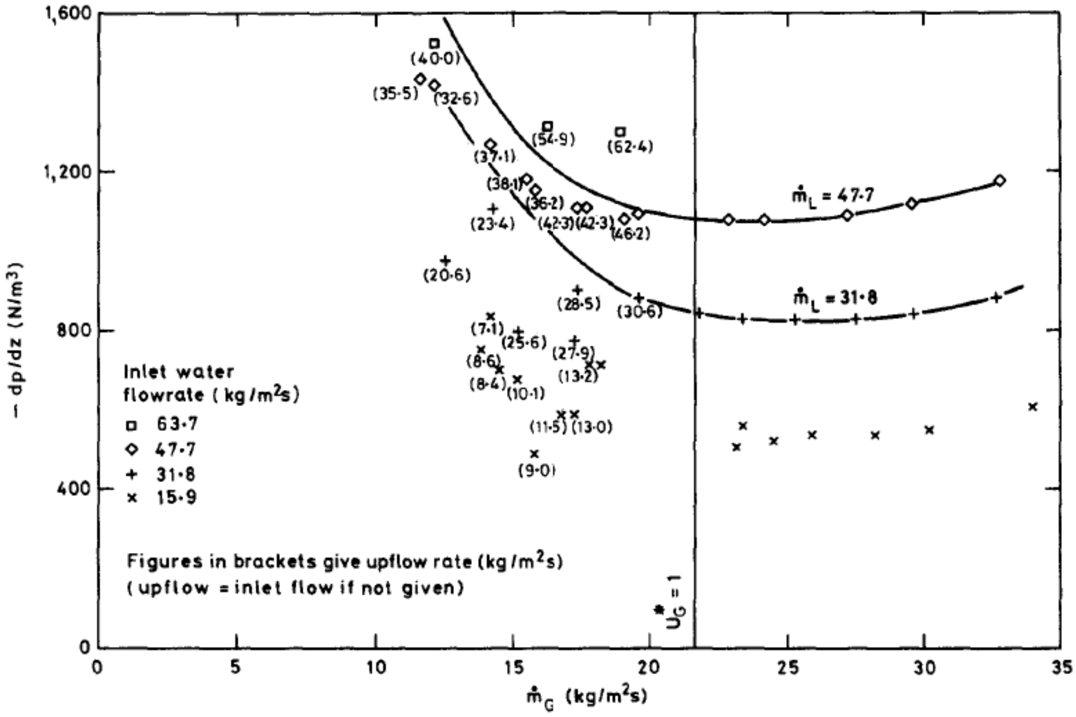

Source: Govan et al. (1991).

Figure 9 - Measured void fraction for different water and air mass fluxes.

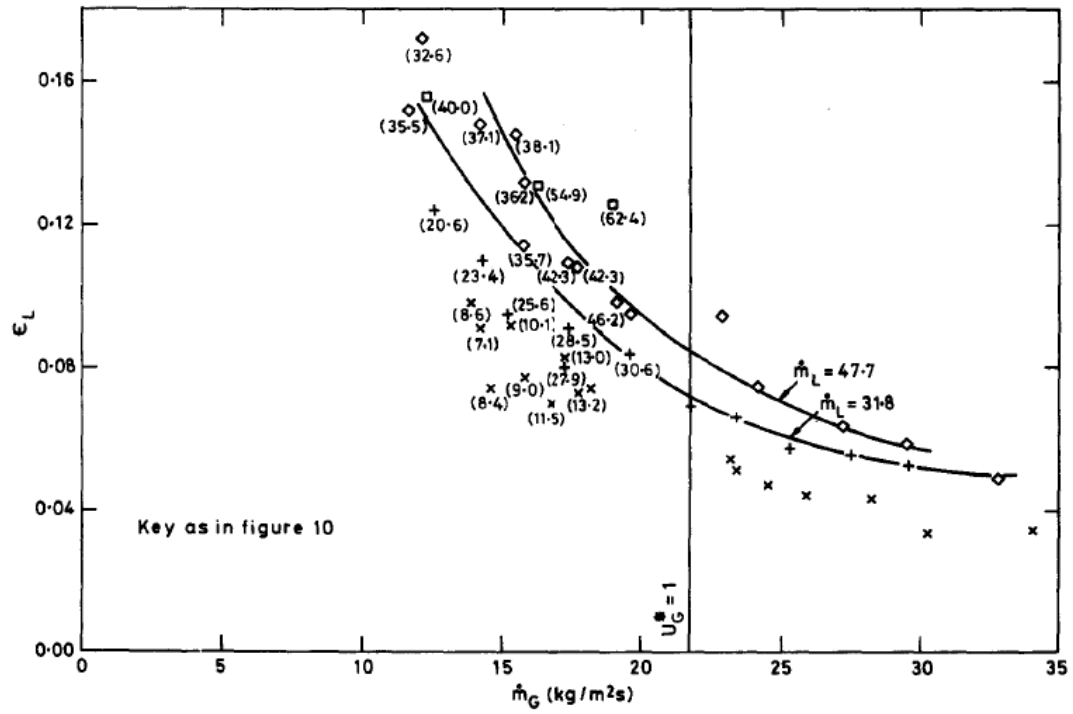

Source: Govan et al. (1991).

In churn flow, pressure gradient decreases with the increase in gas flowrate, mainly due to a decrease in the interfacial friction as flow becomes more stabilized; in annular flow, on the other hand, pressure gradient increases with gas flowrate, as frictional pressure gradient increases. Figure 8 also shows that, for the conditions evaluated by Govan et al. (1991), the point of minimum pressure gradient, which has also been considered as transition criterion between churn and annular flows, and the flow reversal point almost coincide.

Figure 10 shows the pressure gradient, the gravitational pressure gradient, considering only the liquid phase, and the wall shear stress. It shows that the assumption that the point of zero wall shear stress coincides with the minimum pressure gradient (OWEN, 1986) is not true in these cases.

Figure 10 – Total measured pressure gradient, gravitational and frictional contributions for liquid mass flux of 47.7 kg/m²s.

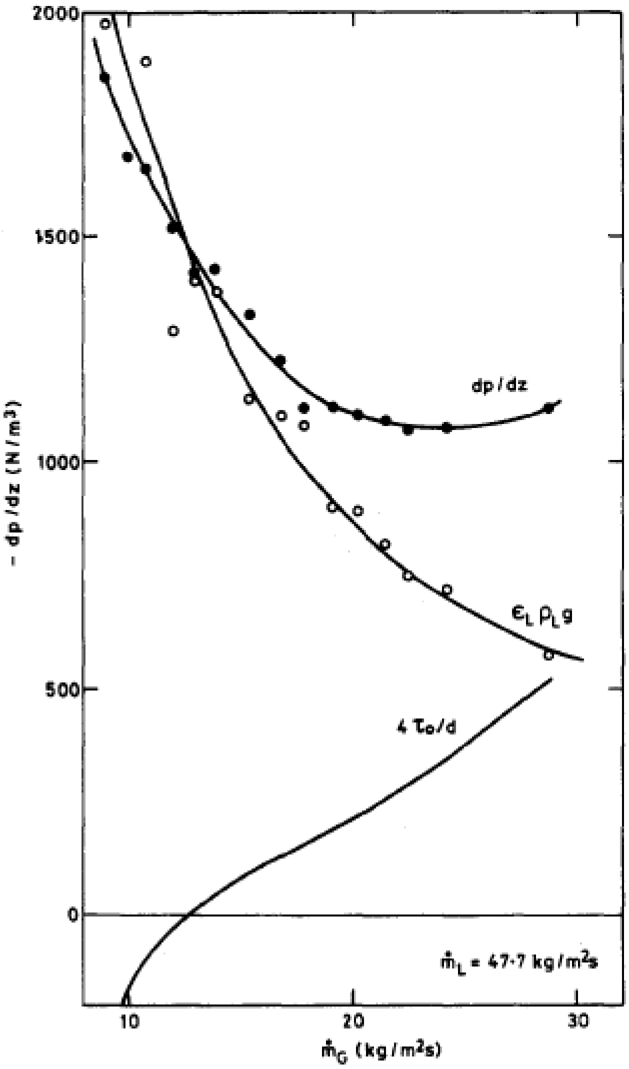

Source: Govan et al. (1991).

The Govan et al. (1991) experiments elucidated some phenomena on flooding and churn flow. Experimental data provided by the authors are still used as reference on churn flow modelling and are used in the present work to compare results from simulations with experiments to validate the method.

2.4 NUMERICAL MODELS

Despite frequently seen in various applications, gas-liquid flows are still a challenge for CFD. Transport equations are used in simulations to describe mass, momentum, and energy transport in different systems. In two-phase flows, more information is required to describe the flow, as fluid properties must be determined for both phases, and the interaction between phases must be modelled. The coupling of both phases is not a trivial task (ROSA, 2012).

Various methods have been proposed to model gas-liquid flows. In mixture models, the mixture of the two-phases is treated as a homogeneous fluid. Governing equations are obtained for the mixture, in an equivalent form of a single-phase flow. This model is based on many simplifications, which reduce the accuracy of the solution. It also requires additional modelling of the interaction between phases (ROSA, 2012). Slippage effects must be modelled, since they are not accounted for initially, as both phases share the same momentum equation.

Gas liquid flows can be modelled considering both phases separately. An Eulerian-Lagrangian approach can be used to model dispersed flows with small phase fractions. In this method, the continuous phase is modeled with an Eulerian approach, in which the fluid properties are calculated in a determined spatial coordinate and time. The dispersed phase is modeled with a Lagrangian particle tracking approach, in which every fluid particle is followed along the flow.

For dispersed flows with high phase fractions, a multi-fluid Eulerian-Eulerian approach can be used. In this case, both phases are treated with Eulerian approaches, in which transport equations are solved for each phase separately in all the domain. This method requires less computational effort for flows with higher phase fraction, although in flows in which both phases are strongly coupled, it can suffer from numerical instabilities (ROSA, 2012). In this method, an average process is required for the dispersed phase fraction, which generates uncertainties on the solution and forbids interface-tracking.

For stratified flows with well-defined interfaces, an interface-capturing can be applied. This is case of the Volume of Fluid (VOF) method, which accompanies the interface by using a scalar indicator which varies between one and zero, depending on which phase is present. In the cells of the mesh where interface is present, the scalar assumes the value of the volumetric fraction of the phase. This method provides a way of following the interface in the cases it is necessary, however, in dispersed flows, it requires a mesh thin enough to capture the interface, which precludes its use. A mesh size of at most 10 times less the size of the smallest droplet is required for an accurate simulation of dispersed flows (WARDLE; WELLER, 2013).

Pham, Jeon and Choi (2020) compared the application of the VOF and the two-fluid methods in the simulation of two-phase flows. VOF was coupled with a Lagragian discrete bubble model for the simulation of sub-grid scale bubbles. The two-fluid provided worse results in the single bubble rising case and better results for a bubbly flow and a free surface flow.

For flows with dispersed and stratified regions, as are the annular and churn flows, a method that combines the multi-fluid Eulerian-Eulerian method with an interface-capturing approach is desired. Cerne, Petelin and Tiselj (2001) provided a coupled method between the two-fluid and VOF models. Later, Wardle and Weller (2013) developed the multiphaseEulerFoam algorithm in the OpenFOAM® CFD software utilizing a hybrid approach. The hybrid methodology is used in the present research, in which simulations are performed using the multiphaseEulerFoam code.

2.4.1 State of The Art on Two-Phase Flow Simulations

Da Riva and Del Col (2009) simulated churn flow in air-water and R134a vapor-liquid mixtures using the VOF method, comparing the results with experiments from Barbosa, Govan and Hewitt (2001). Simulations allowed the observance of liquid waves in the near-inlet region. After reaching a certain thickness, these waves were carried up with the gas core. Authors showed that higher gas velocities result in lower amplitude of the interfacial waves; higher liquid velocities are related to higher wave frequency and film thickness and disturbance. In simulations with R134a, besides the large interfacial waves, smaller secondary waves were seen. This might be an effect of the lower surface tension of the fluid, in comparison to air-water mixtures.

Liu, Li and Quan (2011) investigated countercurrent annular flow applying the VOF method with and additional equation for the droplet mass fraction, considering the core a homogeneous mixture. Results for entrainment fraction, pressure gradient, wall shear stress and film thickness are in accordance with experimental data.

Thaker and Banerjee (2013) simulated air-water flows in small horizontal pipes using the VOF method. The flow patterns visualized in the simulations agree with the flow pattern map obtained experimentally by Vaze and Banerjee (2011), reinforcing the capability of this method to capture gas-liquid flow phenomena.

Karami et al. (2014) used the VOF method to investigate the liquid loading phenomenon. Results for velocities and phase fractions were similar to experiments, while wall shear stress results showed big discrepancies in comparison to the model from Taitel and Dukler (1976), which might be explained by the transient characteristics of the interfacial waves. A mesh refinement analysis was performed, and even the most refined meshes were not able to capture liquid filaments and droplets on the gas core.

Wardle and Weller (2013) develop a hybrid method for the simulation of multiphase flows, combining an Eulerian approach with the VOF method. Qualitative analysis of the flow behavior and quantitative analysis of the flow properties indicate the ability of the method to simulate two-phase and three-phase flows. A further analysis of the convergence of the method and the interfacial compression in different applications is brought by the authors. Parsi et al. (2016) also used a hybrid Eulerian and VOF methodology to simulate churn and annular flows. Simulations allowed the visualization of physical phenomena characteristics of these flows, and void fraction results agreed with experimental data.

Alves (2014) investigated churn and annular flows, and the transition between them. The authors applied the Split Coefficient Matrix Method (SCMM) from Chakravarthy, Anderson and Salas (1980). This method had been used by Städtke (2006) to solve the hyperbolic system of equations which resulted from a one-dimensional transient two-field formulation of two-phase flow. Alves (2014) expanded the application of these method for a three-field formulation, i.e., a model in which governing equations are derived for the gas core, the liquid film, and the entrained droplets. Results for void fraction and pressure gradient were compared with eight different experimental sources, showing agreement with the experiments. The algorithm proposed by the authors, called HyTAF, is also used in the present research for comparison of results.

Bochio et al. (2021) perform a numerical and experimental study of stratified oil-water flow. Simulations are performed in OpenFOAM® using the VOF method. Turbulence is modeled with the $k - \omega$ SST model and with Large Eddy Simulations (LES). Oil flow is considered laminar, and turbulence damping is applied in the $k - \omega$ SST model to avoid the spread of the eddy viscosity to the oil phase. Results for pressure drop, volumetric fraction and phase distribution are similar in the experiments and in the simulations.

Tekavcic, Koncar and Kljenak (2019) used the hybrid method to investigate interfacial wave frequency and amplitude in churn flow. The simulated results showed good agreement with experimental data from Barbosa, Govan and Hewitt (2001) and Wang, Bai and Ma (2013). Authors showed that, without interface compression, the periodic motion of the interfacial waves could not be reproduced in coarse meshes.

Zhao et al. (2020) also investigated interfacial waves on the onset of flooding in inclined pipes. Authors used the VOF method on the simulations and addressed the influence of the contact angle on the gas velocity required for flooding to occur. Results for gas velocity on the onset of flooding and the visualization of flow characteristics show that the method can accurately simulate the flooding phenomenon.

Freitas (2021) used the code proposed by Wardle and Weller (2013) to simulate churn and annular flows, and the transition between them. Simulations reproduced the upper region of the Govan et al. (1991) experiments, above the liquid inlet. The results for the void fraction and pressure gradient were compared to the experimental data and to the HyTAF model from Alves (2014). A mesh analysis was performed. The less refined mesh was not able to capture details of the flow, such as liquid filaments. On the other side, the most refined mesh did not provide the most accurate results in comparison to the experiments and to the HyTAF simulations. The author indicates this is due to the poor aspect ratio of the most refined mesh. Churn flow simulations showed best results than the other cases, which is explained by the lower difference between the velocity of the two phases, which results in less numerical diffusion. Results for pressure gradient were accurate in comparison to the experiments and the HyTAF, while the void fraction was significantly overestimated by the simulations.

2.5 SCIENTIFIC CONTRIBUITIONS

In the present research, simulations of churn and annular flow, and the transition between them are performed using the algorithm proposed by Wardle and Weller (2013), which combines the two-fluid modelling with the volume of fluid method for interface capturing. Freitas (2021) used a similar methodology to simulate the upper region of the Govan et al. (1991) experiments. Here, the liquid inlet region is also simulated, to reproduce the porous-wall liquid inlet from the experiments and evaluate the influence of this region in the results. The present research also expands the analysis, assessing the influence of the Courant number, the turbulence models, the drag force coefficient, and the wall lubrication force modelling in the results.

3 NUMERICAL METHOD

This chapter approaches the hybrid numerical methodology used in the present research. The methodology is based mainly on the works of Tocci (2016), Salles (2020), and Freitas (2021).

The simulations are performed in the free open-source CFD software OpenFOAM®, using the multiphaseEulerFoam algorithm, proposed by Wardle and Weller (2013). It consists of applying the two-fluid model for the simulations, combined with the volume of fluid method for interface capturing, allowing the tracking of the interface between phases, which is crucial for the complete knowledge of annular and churn flows.

This chapter is organized as follows: the transport equations of the two-fluid and volume of fluid models are discussed, followed by the modelling of surface tension, drag forces, wall lubrication forces, and turbulence in the flow; the Courant number, used for time step control in the simulations is then addressed; finally, the numerical procedure performed in the OpenFOAM® algorithm multiphaseEulerFoam and the discretization models required are presented.

3.1 TRANSPORT EQUATIONS

3.1.1 Two-Fluid Model

In the two-fluid method, the transport equations are solved for both phases. This results in a system with two mass conservation equations and two momentum conservation equation for each velocity component.

The assumptions adopted in this work are of tridimensional transient flow, with incompressible, immiscible, and non-reactive fluids, with constant characteristics throughout the pipe.

Equation 10 represents the instantaneous mass conservation, or the continuity equation, for phase k, in which α_k and $\vec{u}_k$ represent the volumetric fraction of the phase and the phase velocity, respectively.

$$\frac{\partial \alpha_k}{\partial t} + \vec{u}_k \nabla \alpha_k = 0 \tag{10}$$

Momentum balance is given by equation 11, with ρ_k and μ_k being the phase density and dynamic viscosity, and p and $\vec{g}$ being the pressure and acceleration of gravity on the flow.

$$\frac{\partial(\rho_k \alpha_k \vec{u}_k)}{\partial t} + (\rho_k \alpha_k \vec{u}_k \cdot \nabla)\vec{u}_k = -\alpha_k \nabla p + \nabla \cdot (\mu_k \alpha_k \nabla \vec{u}_k) + \rho_k \alpha_k \vec{g} + \vec{F}_S + \vec{M}_k \quad (11)$$

The term $\vec{F}_S$ represents the surface tension force and $\vec{M}_k$ represents the interfacial momentum transfer. In the present work, the interfacial forces considered are the drag forces, $\vec{F}_{D,k}$, and the wall lubrication forces, $\vec{F}_{W,k}$, which will be addressed in the following sections along with the surface tension modelling. Lift, virtual mass, and interfacial turbulence dispersion forces are neglected. According to Newton's third law, in a gas-liquid system, the sum of the interfacial forces acting on each phase is given by $\vec{M}_l + \vec{M}_g = 0$.

3.1.2 Interface Capturing

The two-fluid method is not able to follow sharp interfaces, as occur in annular flow. To allow the visualization of the interface, the volume of fluid method with interface compression is used. Other methods can be used for interface tracking, but interface compression is the simplest method for implementation, and requires less computational capacity (WARDLE; WELLER, 2013).

In the VOF method with interface compression, the continuity equation becomes equation 12, with the addition of an artificial compression term (WARDLE; WELLER, 2013)

$$\frac{\partial \alpha_k}{\partial t} + \vec{u}_k \nabla \alpha_k + \nabla \cdot \big(\vec{u}_c \alpha_k (1 - \alpha_k)\big) = 0 \quad (12)$$

The term $\vec{u}_c$ corresponds to an artificial compression velocity, normal to the interface, which compresses the volumetric fraction keeping the interface sharp. The multiplication $\alpha_k(1 - \alpha_k)$ guarantees that compression is only applied on the interface, where $0 < \alpha_k < 1$. In the regions where there is only one phase present, equation 12 becomes equation 10. This compression velocity is calculated by:

$$\vec{u}_c = min\left(C_\alpha|\vec{u}|, max(|\vec{u}|)\right)\frac{\nabla\alpha}{|\nabla\alpha|} \tag{13}$$

The term $\nabla\alpha/|\nabla\alpha|$ is the unitary vector normal to the interface, which determines the direction of the interface compression. The coefficient C_α controls the compression. If its value is restricted to $0 \leq C_\alpha \leq 1$, equation 13 becomes (WARDLE; WELLER, 2013):

$$\vec{u}_c = C_\alpha|\vec{u}|\frac{\nabla\alpha}{|\nabla\alpha|} \tag{14}$$

Coefficient C_α might become then simply a binary coefficient, which controls the use of compression. When it assumes the value of 1, compression is performed. When it becomes zero, compression is not used, and the equations used are from the two-fluid method.

The main difficulty of this method is on determining the value of C_α. The objective of the hybrid formulation is to allow interface capturing where it is clear and can be visualized by the mesh. Cerne, Petelin and Tiselj (2001) proposed that compression would be used depending on the magnitude of the normalized volumetric fraction gradient, γ, defined as:

$$\gamma = \frac{|\nabla\alpha|}{max(|\nabla\alpha|)} \tag{15}$$

With this, in the regions where the volumetric fraction gradient is high, a sharp interface is considered, and the method is applied. Cerne, Petelin and Tiselj (2001) provide a reference value for γ of 0.4. In this approach, sharp interfaces are maintained sharp, and smooth interfaces keep smooth (WARDLE; WELLER, 2013).

Tocci (2016) simply kept constant the value of C_α as 1 (one). Wardle and Weller (2013) used 1 (one) for the gas-liquid interfaces and zero for liquid-liquid interfaces. Despite using a constant value of 1, the method does not become a pure VOF, as the momentum balance is still calculated for both phases with the interfacial terms, characteristics of the two-fluid method. In the present work, C_α is kept as 1 always.

3.1.3 Surface Tension

The surface tension on the interface between phases is calculated with the method proposed by Brackbill, Kothe e Zemach (1992):

$$\vec{F}_{S,k} = \sigma\kappa\,\nabla\alpha \tag{16}$$

in which σ represents the surface tension between the fluids e κ is the local curvature of the interface, given by:

$$\kappa = -\nabla\cdot\left(\frac{\nabla\alpha}{|\nabla\alpha|}\right) \tag{17}$$

Accurately determining the surface tension requires, therefore, the precise calculation of the volumetric fractions.

3.1.4 Drag Force

Interfacial drag force represents the resistance to relative motion between phases. Generally, models for drag forces consider a dispersed flow, in which the drag force depends on the particle size and relative velocity between the phases (ROLLINS, 2018). Wardle and Weller (2013) provide a relation for the drag forces acting on phase k, $\vec{F}_{D,k}$, where d and c correspond to the dispersed and continuous phases, respectively:

$$\vec{F}_{D,c} = -\vec{F}_{D,d} = \alpha_c\alpha_d K(\vec{u}_d - \vec{u}_c) \tag{18}$$

$$K = \frac{3}{4}\rho_c C_D \frac{|\vec{u}_d - \vec{u}_c|}{d_d} \tag{19}$$

where d_b is the particle diameter of the dispersed phase and C_D is the drag coefficient. Various models for drag coefficient are implemented in OpenFOAM®. The dispersed and continuous phases can be predetermined in OpenFOAM®, however, for the cases in which there is no obvious dispersed phase, a blended scheme can be used. In this approach, the drag coefficient is calculated twice considering each phase as dispersed. Then, the final drag coefficient is obtained through an average of the two coefficients calculated, weighted by the volumetric fraction of the continuous phase in each case.

The Schiller and Naumann relation for the drag coefficient is shown in equation 20 (WARDLE; WELLER, 2013).

$$C_D = \begin{cases} \frac{24(1+0{,}15Re^{0{,}687})}{Re}, & Re \geq 1000, \\ 0{,}44, & Re > 1000 \end{cases} \tag{20}$$

$$Re = \frac{\rho_c|\vec{u}_d - \vec{u}_c|d_d}{\mu_c} \tag{21}$$

The Ishii and Zuber model differs from the Schiller and Naumann model is that it uses a mixture dynamic viscosity for calculating the Reynolds number, instead of considering only the continuous phase viscosity.

$$Re = \frac{\rho_c|\vec{u}_d - \vec{u}_c|d_d}{\mu_m} \tag{22}$$

$$\mu_m = \mu_c\left(1 - \frac{\alpha_d}{\alpha_{max}}\right)^{\frac{-2.5\alpha_{max}}{\mu^*}} \tag{23}$$

$$\mu^* = \frac{\mu_d + 0.4\mu_c}{\mu_d + \mu_c} \tag{24}$$

The term α_{max} is the maximum phase fraction, which is 1 for flows with fluid particles (ROLLINS, 2018; RUSCHE, 2003).

The Wen and Yu drag model was developed for solid particles and consists in multiplying the Schiller and Naumann drag coefficient by $\alpha_c^{-2.65}$ (ROLLINS, 2018). The Gidaspow model is similar to the Wen and Yu model, with the difference that Re is multiplied by α_c (GIDASPOW, 1994).

$$Re = \frac{\alpha_c\rho_c|\vec{u}_d - \vec{u}_c|d_d}{\mu_m} \tag{25}$$

The Gidaspow model is valid when $\alpha_c > 0.8$.

In the Ergun model, the drag coefficient is obtained with equation 26 (ROLLINS, 2018). This model is valid for $\alpha_c < 0.8$.

$$C_D = 150\frac{4}{3}\frac{\alpha_d}{\alpha_c^{-2}Re_b} + 1.75\frac{4}{3}\frac{1}{\alpha_c} \tag{26}$$

$$Re_b = \frac{\rho_c|\vec{u}_d - \vec{u}_c|d_d}{\mu_m} \tag{27}$$

OpenFOAM® has the GidaspowErgunWenYu model implemented, which consists of using the Ergun model when $\alpha_c < 0.8$ and the Gidaspow model when $\alpha_c > 0.8$ (ROLLINS, 2018).

In the present work, an analysis of the influence of the drag coefficient model in the results of the simulation is performed. The drag coefficient models analyzed are the SchillerNaumann, IshiiZuber and GidaspowErgunWenYu. A constant diameter is considered for the dispersed phase. Salles (2020) analyzed two different droplet's diameters (5×10^{-5} and 1×10^{-5}), and small differences were seen. Smaller droplet's diameter is related with higher void fractions, due to a decrease in the liquid film thickness. Here, the value of 5×10^{-5} is used, as it allowed a better visualization of the liquid film in the work from Salles (2020).

3.1.5 Wall Lubrication Force

The wall lubrication forces, $\vec{F}_{W,k}$, are used to predict peaks of void fraction near the walls. This force is responsible for driving bubbles away from the walls (ROLLINS, 2018). It is given by equation 28 (FRANK, 2005), where c and d correspond to the continuous and dispersed phase, respectively; $\hat{n}_W$ is the vector normal to the wall; $\vec{U}_r = \vec{U}_d - \vec{U}_c$ is the relative velocity between phases; the multiplication $\vec{U}_r - \left(\vec{U}_r \cdot \hat{n}_W\right)\hat{n}_W$ is the projection of the relative velocity on the wall; and C_W is the wall lubrication coefficient.

$$\vec{F}_{W,c} = -\vec{F}_{W,d} = C_W \rho_d \alpha_c \left|\vec{U}_r - \left(\vec{U}_r \cdot \hat{n}_W\right)\hat{n}_W\right|^2 (-\hat{n}_W) \tag{28}$$

Many models have been proposed to calculate the wall lubrication coefficient, C_W. This parameter depends on the distance to the wall, and is always positive, meaning that bubbles are always pushed away from the wall by this force.

Antal, Lahey and Flaherty (1991) proposed the following correlation for the wall lubrication coefficient:

$$C_W = \max\left(0, \frac{C_{W1}}{D_b} + \frac{C_{W2}}{y_W}\right) \tag{29}$$

where D_b is the bubble diameter; and y_W is the distance to the wall.

This relation ensures that wall lubrication is only active in the near-wall region, until a cut-off distance of:

$$y_W \leq -\frac{C_{W2}}{C_{W1}} D_b \tag{30}$$

The authors provide the following values for the coefficients: $C_{W1} = -0.01$ and $C_{W2} = 0.05$.

Frank (2005) provides another model for C_W, as in equation 31.

$$C_W = C_{Wl} \max\left(0, \frac{1}{C_{Wl}} \frac{1 - \frac{y_W}{C_{Wc} D_b}}{C_{Wd} y_W \left(\frac{y_W}{C_{Wc} D_b}\right)^{p-1}}\right) \tag{31}$$

The coefficients C_{Wc}, C_{Wd} and p are equal to 10.0, 6.8 and 1.7, respectively, and C_{Wl} is given as function of the Eotvos number, Eo, as in equation 32.

$$C_{Wl} = \begin{cases} 0.47, & Eo < 1, \\ \exp(-0.933 Eo + 0.179), & 1 < Eo < 5 \\ 0.00599 Eo - 0.0187, & 5 < Eo < 33 \\ 0{,}44, & Eo > 33 \end{cases} \tag{32}$$

$$Eo = \frac{(\rho_d - \rho_c) g D_b^2}{\sigma} \tag{33}$$

The Tomiyama wall lubrication model is given by equation 34 (TOMIYAMA et al., 1998):

$$C_W = \frac{1}{2} C_{Wl} D_b \left(\frac{1}{y_W^2} - \frac{1}{(D - y_W)^2}\right) \tag{34}$$

where D is the pipe diameter and C_{Wl} is calculated as in equations 32 and 33. This correlation is based on glycerol-water experiments with Morton number of $Mo = \frac{g\mu_d^4(\rho_d - \rho_c)}{\rho_d^2 \sigma^3} = -2.8$, which is out of the range of most air-water systems. The applicability of this model is, therefore, limited. However, it has been widely used in CFD simulations.

The three models discussed – Antal, Frank and Tomiyama – are implemented in the OpenFOAM®. This research assesses the influence of the wall lubrication models in the results of the simulation, evaluating the difference on the results considering no-wall lubrication and each of the previous models.

3.1.6 Turbulence

The solution of the instantaneous transport equations without simplifications or average procedures is called Direct Numerical Simulation (DNS). This method allows the simulation of the smallest levels of the flow, such as the small vortices behind bubbles. It computes turbulence and interfacial effects without the need for closure relations. However, it requires enormous computational capacities, restricting it to simple applications (FERZIGER; PERIC, 2002).

To avoid these high computational costs, the Reynolds Averaged Navier-Stokes (RANS) equations can be used. In this case, an average procedure is performed, and the instantaneous equations are turned into average equations. This process introduces the Reynolds Stress Tensor into the momentum conservation, which accounts for the turbulent fluctuations of the flow velocity (WILCOX, 2006).

Using the Boussinesq eddy viscosity approximation, the Reynolds Stress Tensor can be computed as the product of an eddy viscosity and the main strain-rate tensor (WILCOX, 2006). Many models for assessing this eddy viscosity have been proposed. The most common are the two-equation models, such as the $k - \omega$ and $k - \varepsilon$ models, which introduce two new partial differential equations for determining turbulence parameters, all based on the Boussinesq approximation. In these equations, as in traditional balance equations, there are convective, diffusive, source and dissipations terms.

The $k - \omega$ SST model was developed after the $k - \omega$ and $k - \varepsilon$ models. The $k - \varepsilon$ model was less sensible to free-stream conditions, however it yielded poor results in near-wall regions. The $k - \omega$ model, on the other hand, provided good results in the boundary layer, but was too sensible to the boundary conditions of free-stream flow. To overcome this drawback of the existing models, Menter (1994) developed the $k - \omega$ SST model, which uses damping functions to transit between both previous models. With this method, it is possible to apply the $k - \omega$ model near the walls of the flow and the $k - \varepsilon$ model away from the walls, getting the best of each, with a damping function that guarantees the transition between the two models is smooth.

These two equation models were firstly developed for single phase flows. The first applications of the two-equation models in two-phase flows considered that turbulence was dictated by the continuous phase, so the equations should be derived using the continuous phase properties (HILL et al., 1994). For flows with no obvious dispersed phase, as annular and churn flows, this approximation is not accurate. Thus, models that account for both phases have been proposed (BEHZADI; ISSA; RUSCHE, 2004). Although most of these models are proposed for dispersed flows, which is not the case of the annular and churn patterns, they provide more physical meaning than models which account only for the continuous phase. Rezende et al. (2015) provides a more complete formulation considering a two-fluid model with an interfacial tensor. However, its implementation is restricted to Ansys Fluent®. Implementing this method in OpenFOAM® is beyond the scope of this work.

Many models for assessing turbulence effects are implemented in OpenFOAM®. In the present research, the chosen ones are the $k-\varepsilon$, $k-\omega$ SST model and the mixture $k-\varepsilon$ model. The equations and constants for the $k-\varepsilon$ and the $k-\omega$ SST models can be found in Launder and Sharma (1974) and Menter (1994), respectively. For the mixture $k-\varepsilon$ model, which adds to the original $k-\varepsilon$ model a source term for the turbulence due to inter-phase forces, details can be found in Behzadi, Issa and Rusche (2004).

In the points close to the pipe walls, turbulence parameters are calculated with wall functions. OpenFOAM® has different wall functions implemented in its libraries. Here, the `nutkWallFunction` is used, in which the turbulent viscosity is obtained based on the turbulent kinetic energy (OPENFOAM, 2012).

3.2 COURANT NUMBER

An important aspect on the convergence of simulations is the timestep. In the present research, the Courant-Friedrichs-Lewis (CFL) number, or Courant number, Co, is used for determining the timestep. This criterium provides the maximum distance a flow property can be transported in one timestep in relation to the characteristic length of the elements of the mesh. It is given by equation 34, in which Δt corresponds to the timestep, U_i and Δx_i are the velocity and the cell characteristic length in the direction $i = x, y, z$.

$$Co = \Delta t \sum_{i=1}^{n} \frac{U_i}{\Delta x_i} \tag{35}$$

Wardle e Weller (2013) provide a maximum value of 0.25 for the Courant number in a multiphase flow. This means that any information of the flow travels, in one timestep, at most one quarter of the distance between two points in the grid. Freitas (2021) uses a maximum value of 0.005 and a maximum timestep of 10^{-6}, requiring long simulations.

In the present research, the influence of the Courant number in the simulation results is assessed. For this, simulations are performed using different maximum Courant numbers, varying between 0.25, 0.125, 0.05 and 0.01. The results are compared in order to evaluate the need to limit timestep to small values such as done by Freitas (2021).

3.3 NUMERICAL PROCEDURE

The whole procedure for solution of the system of differential equations is performed in the OpenFOAM®. Discretization is performed with the finite volume method. Discretization and interpolation models must be provided, from a list of available models implemented in the software.

In every OpenFOAM® case, there are three initial folders: “0”, “constant” and “system”. In the “0” folder, the initial conditions, and the boundary conditions for the flow variables (pressure, velocity, and turbulent parameters) are provided. In the “constant” folder the fluid properties (density, viscosity, and surface tension) and turbulence models ($k - \omega$ and mixture $k - \varepsilon$) are defined. The “system” folder is where the numerical method is controlled, i.e., the interpolation and discretization schemes are defined, with the maximum Courant number and other important parameters for the simulations.

3.3.1 The Algorithm

Figure 11, from Freitas (2021), illustrates the numerical procedure employed in the algorithm multiphaseEulerFoam, developed by Wardle e Weller (2013).

Initially, the timestep is updated, limited by the maximum Courant number based on the velocity of the previous iteration. Then, the volumetric fraction equations are solved with the interface capturing method. After this, the drag and lubrication coefficients are computed, and the system of balance equations is generated. For the pressure-velocity coupling, the Pressure-Implicit with Splitting of Operators (PISO) method is applied. Finally, turbulence effects are calculated, and velocity is corrected.

In the PISO method, initially the momentum equation is solved to estimate the velocity using the pressure gradient from the previous iteration. With this velocity, a new pressure field is obtained, used for correcting the velocity estimation. This method is frequently used in transient problems because it does not require external loops in its solution, as the SIMPLE method would. This decreases the simulation time, which is important in transient simulations that require very small timesteps. More detail about solution methods for the pressure-velocity coupling can be found in Jasak (1996).

Figure 11 – Solution procedure of the multiphaseEulerFoam algorithm.

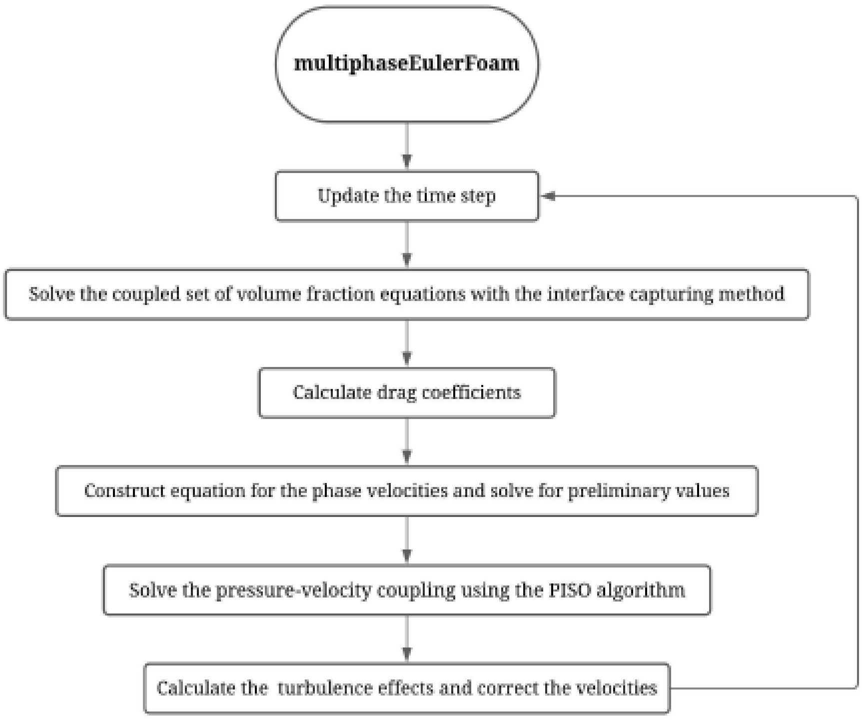

Source: Freitas (2021).

3.3.2 Discretization

The system of transport equations is discretized in OpenFOAM® using the finite volume method. It is necessary to provide to OpenFOAM® the discretization schemes and interpolation schemes, used to obtain the flow properties in the cell faces. This research uses the same schemes as in Tocci (2016) e Freitas (2021). Transient discretization uses the implicit Euler method; gradients and Laplacians are discretized with the least squares and the Gauss methods, respectively. The convective terms and the divergence of the turbulent parameters are discretized with the Gauss limited linear schemes, while the volumetric fraction divergent is discretized with the Van Leer method.

Volumetric fraction requires an additional limiter, to ensure that non-physical values does not arise, i.e., volumetric fractions higher than one or lower than zero. For that, OpenFOAM® uses the Multidimensional Universal Limiter with Explicit Solution (MULES) algorithm. More detail about this limiter can be found in Tocci (2016).

4 NUMERICAL SIMULATIONS

4.1 GEOMETRY OF THE PROBLEM

The geometry used in the simulations of this research aims to reproduce the test section used in the Govan *et al.* (1991) experiments, which consists on a vertical pipe with a porous wall liquid inlet and outlet. The influence of the geometry is assessed by comparison with the work from Freitas (2021), which simulated only the upper region of the pipe, above the liquid inlet. Here, the radial liquid inlet and a development region right above the air inlet are also considered.

Simulating the liquid inlet geometry would ideally require a complex geometry, that allowed the simulation of the flow through the porous wall. As no information was given about the porous wall geometry and pressure gradient, coupling the wall to the geometry would become a challenge, besides significantly increasing the number of cells in the mesh, requiring much higher simulation time and computational memory. Therefore, the liquid inlet is considered as an open wall, with a defined liquid mass flow rate corresponding to the experiments.**Erro! Fonte de referência não encontrada.**Figure 12 shows the geometry used. It consists of a 1.932 m long pipe with 31.8 mm of internal diameter. Above the pipe inlet, there is a 20 cm long development region. Liquid inlet is 50 mm long and the final region of the pipe is 1.682 m long, as in the experiments (GOVAN et al., 1991). The air inlet corresponds to the lower pipe inlet. Although the pipe inside diameter is 31.8 mm, the air inlet corresponds to a 28.8 mm ID region. This allows that in the region close to the pipe wall a liquid outflow can occur, so, if there is liquid downflow, it will not accumulate in the bottom of the pipe or restrict the air inlet.

4.1.1 Computational Grid

Hernandez-Perez, Abdulkadir e Azzopardi (2011) analyzed the influence of the mesh used in two-phase flow simulations in cylindrical pipes. According to the authors, the butterfly mesh, in which the pipe center has cartesian coordinates and the external region has cylindrical coordinates, provides the best results for these cases. Figure 13 illustrates the cross-sectional view of the butterfly mesh used in the simulations of the present research.

Freitas (2021) evaluated mesh refinement influence. The most refined mesh simulated by the author did not provide the most accurate results for pressure gradient and void fraction, however it was the only mesh that allowed the visualization of flow effects such as the presence of filaments. For this reason, the cross-sectional refinement used in the present research is the same as the most refined mesh from the work of Freitas (2021). The axial refinement is also proportional to the Freitas (2021) simulation. The mesh used has a total of 237600 cells.

Figure 12 – Geometry of the simulations.

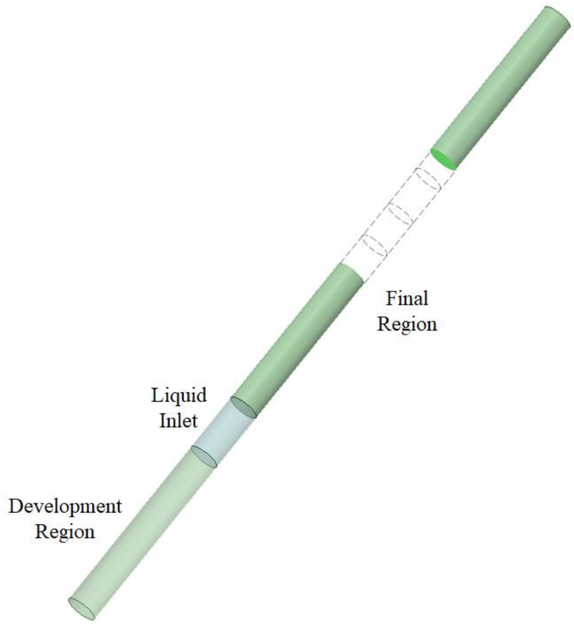

Source: The author (2022).

Figure 13 – Horizontal section of the mesh grid used in the simulations.

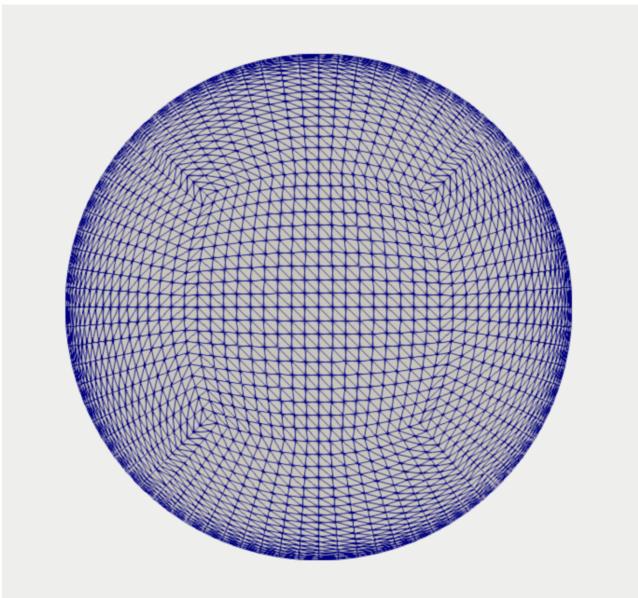

Source: the author (2021).

4.2 FLUID PROPERTIES

Simulations are performed with air and water. The initial and boundary conditions for the fluid properties are the same used in Freitas (2021) simulations are shown in Table 1.

Table 1 – Fluid properties.

	Air	**Water**
ρ [kg/m³]	1.58	997
μ [Pa.s]	1.84×10^{-5}	0.001

Source: Adapted from Freitas (2021).

4.3 BOUNDARY CONDITIONS

The boundary conditions for velocity and pressure are based on the experiments. For the air and water inlets, the mass flow rates of each phase are defined, from which OpenFOAM® automatically calculates the velocities. Three cases from the Govan *et al.* (1991) experiments are simulated: a churn flow; an annular flow; and one case in the transition between patterns, which will be named hereafter, for simplicity, transition flow. Table 2 provides the mass flow rate of both fluids in each case.

Table 2 – Air and water mass fluxes at churn and annular flows, and the transition between them.

	Churn		**Transition**		**Annular**	
	Air	**Water**	**Air**	**Water**	**Air**	**Water**
$\dot{m}$ [kg/s]	1.56×10^{-2}	2.43×10^{-2}	1.73×10^{-2}	2.53×10^{-2}	1.87×10^{-2}	2.53×10^{-2}

Source: The author (2021).

The turbulence parameters k, ω and ε must be defined also in the inlet regions. Turbulent kinetic energy in the inlet region can be calculated as in equation 36.

$$k = \frac{3}{2}\left(I\left|U_{ref}\right|\right)^2 \tag{36}$$

in which, U_{ref} is the reference inlet velocity , and I turbulence intensity, calculated as in equation 37 (VERSTEEG; MALALASEKERA, 1995):

$$I = 0{,}16Re^{-\frac{1}{8}} \tag{37}$$

The turbulent parameters ω and ε are calculated in the inlet by equations 38 and 39, respectively.

$$\omega = \frac{k^{0.5}}{C_{\mu}^{\frac{1}{4}} l} \tag{38}$$

$$\varepsilon = \frac{C_{\mu}^{\frac{3}{4}} k^{1.5}}{l} \tag{39}$$

where C_{μ} equals 0,09 e l is a turbulent scale given by (VERSTEEG; MALALASEKERA, 1995):

$$l = 0{,}07D \tag{40}$$

4.4 SUMMARY OF THE SIMULATIONS

In the next chapter (Chapter 5) the influence of the Courant number is evaluated. For this, simulations of different maximum Courant numbers are performed for churn, transition, and annular flows. Results for pressure gradient and void fraction are compared to the experiments from Govan et al. (1991) and to the simulations from Freitas (2021), in order to evaluate the effects of different liquid inlet geometries. Also, the different interface dynamics in each case are visualized with void fraction isosurfaces.

The later chapters present respectively: turbulence model analysis; with a comparison between results from versions 7 and 9 of the OpenFOAM® software; the influence of wall lubrication models and drag coefficient comparison

5 COURANT NUMBER ANALYSIS

This section presents the results for the analysis of the maximum Courant number. Simulations were performed for churn, transition, and annular flows, each with different Courant numbers, varying between 0.01, 0.05, 0.125, and 0.25. The three patterns are simulated with the mass fluxes that correspond to their respective pattern in the experiments from Govan et al. (1991).

These simulations considered no wall lubrication and used the Schiller and Naumann drag coefficient. Turbulence modelling was performed with the $k-\omega$ SST model, which computes turbulence using the mixture properties.

5.1 CHURN FLOW

First, the average air volumetric fraction in each time step is presented for churn flow. These values were computed by performing a volume integral of the air volumetric fraction in the volume between two planes located at heights of 0.494 m and 1.42 m. These planes correspond to the simultaneous closing valves used in the Govan et al. (1991) experiments for measuring void fraction.

Figure 14 shows the void fraction for each of the maximum Courant numbers analyzed, together with the results from Freitas (2021), the simulations of the HyTAF code (ALVES et al., 2017) and the average values from Govan et al. (1991). In comparison to the experiments, all simulations overestimate the void fraction value; the case with maximum Courant number of 0.01 provides the most accurate results, while the cases with Courant of 0.05 and 0.25 provide the least accurate. Simulations with maximum Courant of 0.01 and 0.125 also reach “steady-state” sooner, at a time of approximately 2.5 s, while the other cases reach it at approximately 3.5 s. The wavy characteristic of churn flow is well represented by the simulations, as all cases capture this behavior and provide the wavy results for the air volumetric fraction.

In comparison with the simulation from Freitas (2021), which significantly overestimated the void fraction, the simulations performed in the present research provide better results. This indicates that the liquid inlet geometry might influence the results and correctly reproducing the desired geometry is crucial for obtaining accurate results. It can be seen that the simulation from Freitas (2021) reached “steady-state” sooner. This happens because “steady-state” is reached at a higher value than the simulations performed in the present research, so that the initial condition of pure air in the pipe is a closer approximation, and also because the inlet dynamics are simpler. Freitas (2021) results for void fraction also does not have the clear oscillatory behavior as seen in the simulations of the present research, which indicates that these oscillations probably emerge in the inlet region and are transported with the flow.

In comparison to the average value provided by the HyTAF, only the case with Courant number of 0.01 provides more accurate results; the other ones overestimate this parameter.

Table 3 provides the average values for each case, calculated in the last second of the simulation, after simulations have reached “steady-state”, and the relative error in comparison to the experiments.

Figure 14 – Void fraction in churn flow as function of time for the different maximum Courant numbers.

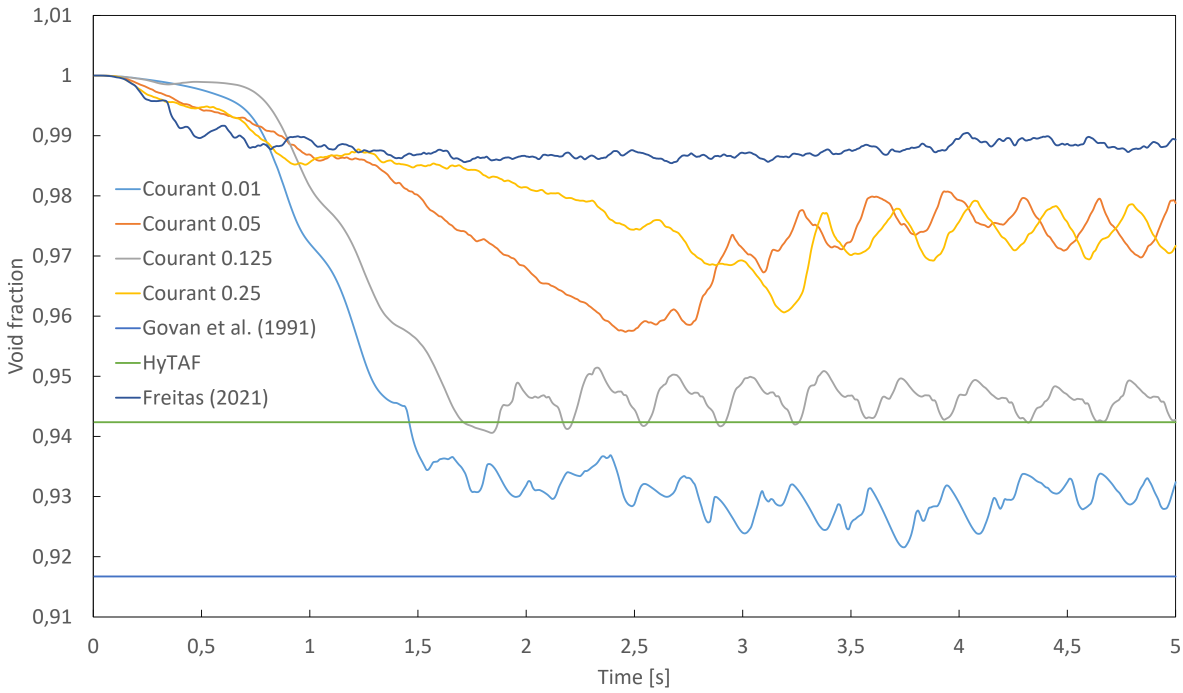

Source: The author (2022).

Table 3 – Average values of void fraction in churn flow at each case, with the relative errors in comparison to the experiments.

Courant	0.01	0.05	0.125	0.25	Freitas (2021)	Govan et al. (1991)
Average	0.930	0.975	0.946	0.975	0.989	0.917
Error	1.46%	6.37%	3.19%	6.31%	7.87%	-

Source: The author (2022).

The maximum Courant number of the simulation influences substantially the results. However, a smaller Courant number does not indicate necessarily better results, as the relative error from the simulations with Courant of 0.05 was higher than the case with Courant of 0.125. While the case with Courant of 0.01 decreases the relative error by more than half, in comparison to every other case, it also increases the simulation time significantly. The best choice depends on the relation between accuracy and simulation time required. In general, as indicated by the relative errors, both the cases with maximum Courant number of 0.01 and 0.125 can predict well the void fraction in the flow.

Figure 15 presents the results for pressure gradient in each case, with the results from Freitas (2021), from HyTAF, and the average values from Govan et al. (1991). Pressure gradient is calculated by computing the pressure in two planes located at 0.631 and 1.477 m height.

Table 4 shows the average values for the last second of the simulation in each case and the relative error in comparison to the experiments.

Figure 15 – Pressure gradient in churn flow as function of time for the different maximum Courant numbers.

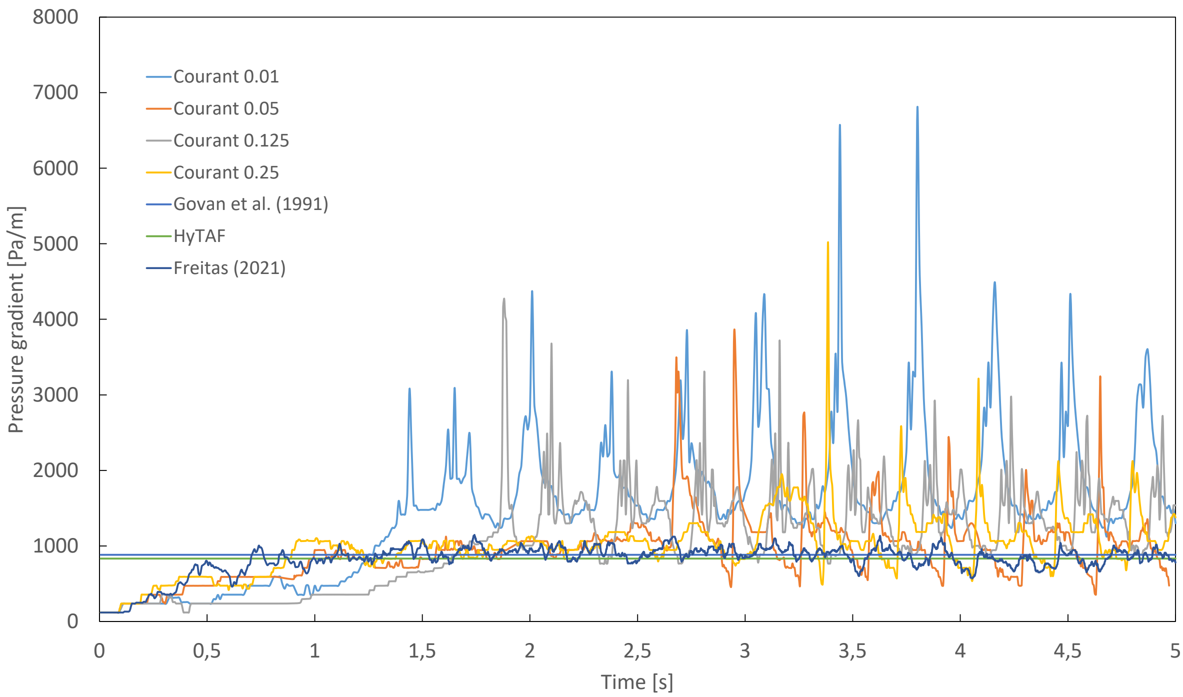

Source: The author (2022).

Table 4 – Average values of pressure gradient in churn flow at each case, with the relative errors in comparison to the experiments.

Courant	**0.01**	**0.05**	**0.125**	**0.25**	**Freitas (2021)**	**Govan et al. (1991)**
Average	1979	1022	1376	1139	768	883
Error	124%	15.8%	55.8%	29.0%	13.0%	-

Source: The author (2022).

All simulations performed overestimate significantly the pressure gradient, in comparison to the experiments, reaching peaks up to more than 7 times higher than expected. At all cases, huge oscillations can be seen. Unlike the previous results for void fraction, here the maximum Courant number of 0.01 provides the least accurate results, while the Courant of 0.05 provides the most accurate. Simulations from Freitas (2021) provided good results for pressure gradient. The change in the liquid inlet geometry, despite improving results for void fraction, worsen the results for pressure gradient in every case, indicating that this change generates higher pressure gradients in the flow. The one-dimensional simulations performed on HyTAF also provide very accurate results for the pressure gradient.

It is expected that the simulations that provide lower void fraction results also provide the highest results for pressure gradient, due to the increase in the gravitational pressure gradient in the cases with higher water volumetric fraction. These results indicate an inability of the method to estimate the correct pressure gradient on the flow. The use of more accurate drag coefficient, wall lubrication and turbulence models might improve them.

For a better understanding of the phenomena occurring during flow in each simulation, the next subsections show the external and internal view of the void fraction. The cases with maximum Courant number of 0.01 and 0.05 were chosen for this visualization. As the other two cases present a similar visualization, they were omitted.

5.1.1 Courant 0.01

Figure 16 shows the external view at different times of the void fraction in the simulation with maximum Courant number of 0.01. The red color represents air, while blue represents water. Initially, water is present only in the inlet region. As air starts flowing upwards, it is able to carry up all the liquid in the form of a liquid film adjacent to the wall. In the Govan et al. (1991) experiments, for the mass fluxes used in this simulation, there is a small downflow of liquid. That means that not all liquid is carried upwards. This phenomenon is not captured by the simulations, probably due to an overestimation of the interfacial drag, which means that air needs a lower velocity than expected to drag the liquid along with it.

After the first second of simulation, the liquid film continues to flow upwards, until reaching a limiting height of approximately 0.65 m, i.e., 0.4 m above the end of the liquid inlet. Above this height the film pulverizes (same phenomena observed by Salles (2020) and Freitas (2021)), and liquid is carried up in the form of waves which detach from the liquid film.

Figure 16 – External view of the air volumetric fraction in churn flow with maximum Courant number of 0.01.

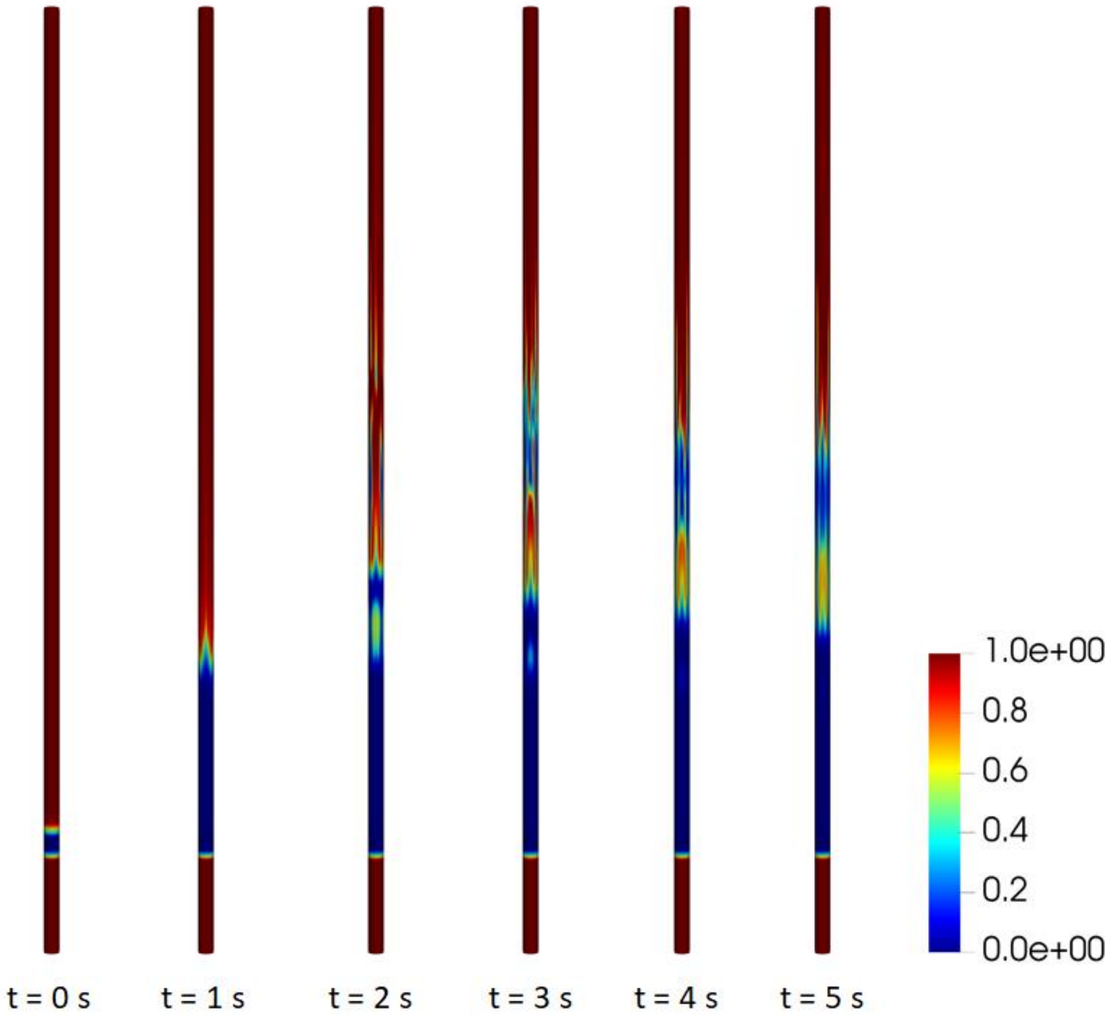

Source: The author (2022).

For a more detailed visualization of the flow, a horizontal slice of the pipe is used. Figure 17 shows the void fraction in a horizontal section at a height of 0.4 m at 4, 4.5, and 5 seconds. The liquid flows upwards only as a film that encircles the gas core. The small differences in film thickness show that small waves are present on the interface. Although these waves could indicate the passage of disturbance waves, seen in annular flow, in this case, their frequency is approximately 2.8 Hz, which is significantly lower than the frequency of the disturbance waves (LIN et al., 2020). One can speculate that a cause for this lower value may be the mesh size in the axial direction, that is distorting the wave amplitude and frequency.

Figure 17 – Horizontal section of void fraction in churn flow at a height of 0.4 m at different times for the maximum Courant number of 0.01.

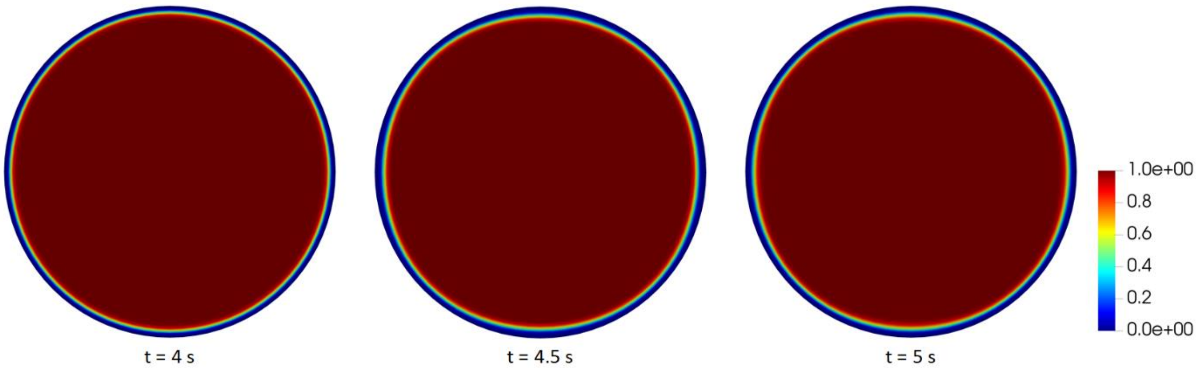

Source: The author (2022).

Figure 18 – Horizontal section of void fraction in churn flow at a height of 0.8 m at different times for the maximum Courant number of 0.01.

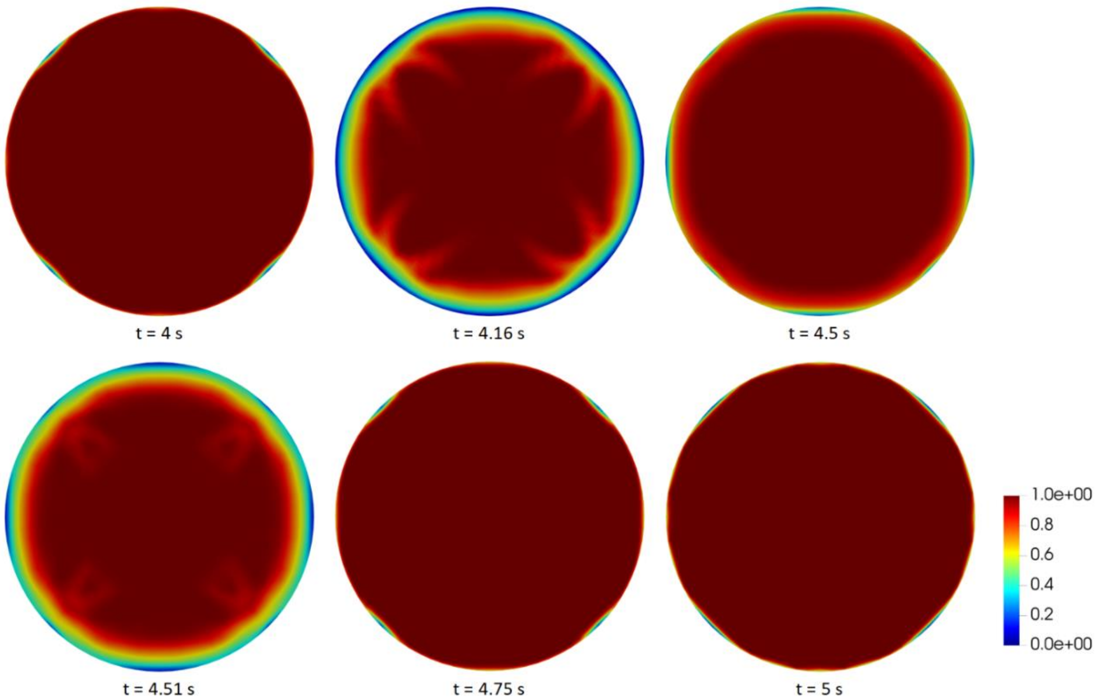

Source: The author (2022).

Figure 18 presents the void fraction in a horizontal section at a height of 0.8 m for different times. At this height, liquid film is almost completely pulverized, and the presence of waves is more noticeable, as they have higher amplitude than the at the height of 0.4 m. In this section, some small filaments can also be seen being carried upwards.

Although some characteristic aspects of churn flow can be seen in the simulation, as the wavy motion of the interface, is the simulations cannot capture some phenomena which were expected. The oscillatory movement of liquid and a high presence of liquid filaments and droplets, characteristics of churn flow, are not seen. In fact, the region right above the liquid inlet presents a behavior more like annular flow. A more accurate prediction of droplets and filaments formation might be achieved with a finer mesh. The film pulverization after a certain height is also not reported in the experiments and was not expected. This phenomenon probably happens in the simulations due to numerical diffusion. However, in fully transient experiments, where there are abrupt changes in the flow rates this phenomenon is known to occur as demonstrated by Waltrich et al. (2015) and Alves (2014).

5.1.2 Courant 0.05

Figure 19 presents the external view of the void fraction for the simulation with maximum Courant number of 0.05. In this case, maximum liquid film height is approximately 0.5 m, lower than in the previous one. Also, above this height, liquid flows upwards as filaments, and not liquid waves.

Figure 20 shows the cross-sectional view of the void fraction at a height of 0.4 m. In this case, the difference in film thickness at different times is more noticeable, showing interfacial waves of higher amplitude, while their frequency is very similar to the former case. Again, no filaments or droplets are seen.

Figure 21 shows the horizontal section at a height of 0.8 m. As the external view indicated, in this case no liquid waves are seen at this height. But there is a higher presence of liquid filaments inside the gas core. This difference explains why the simulation with maximum Courant number of 0.05 provided much higher values for the void fraction than the case with Courant of 0.01, as the liquid waves transport a higher volume of liquid than the filaments.

Figure 19 – External view of the air volumetric fraction in churn flow with maximum Courant number of 0.05.

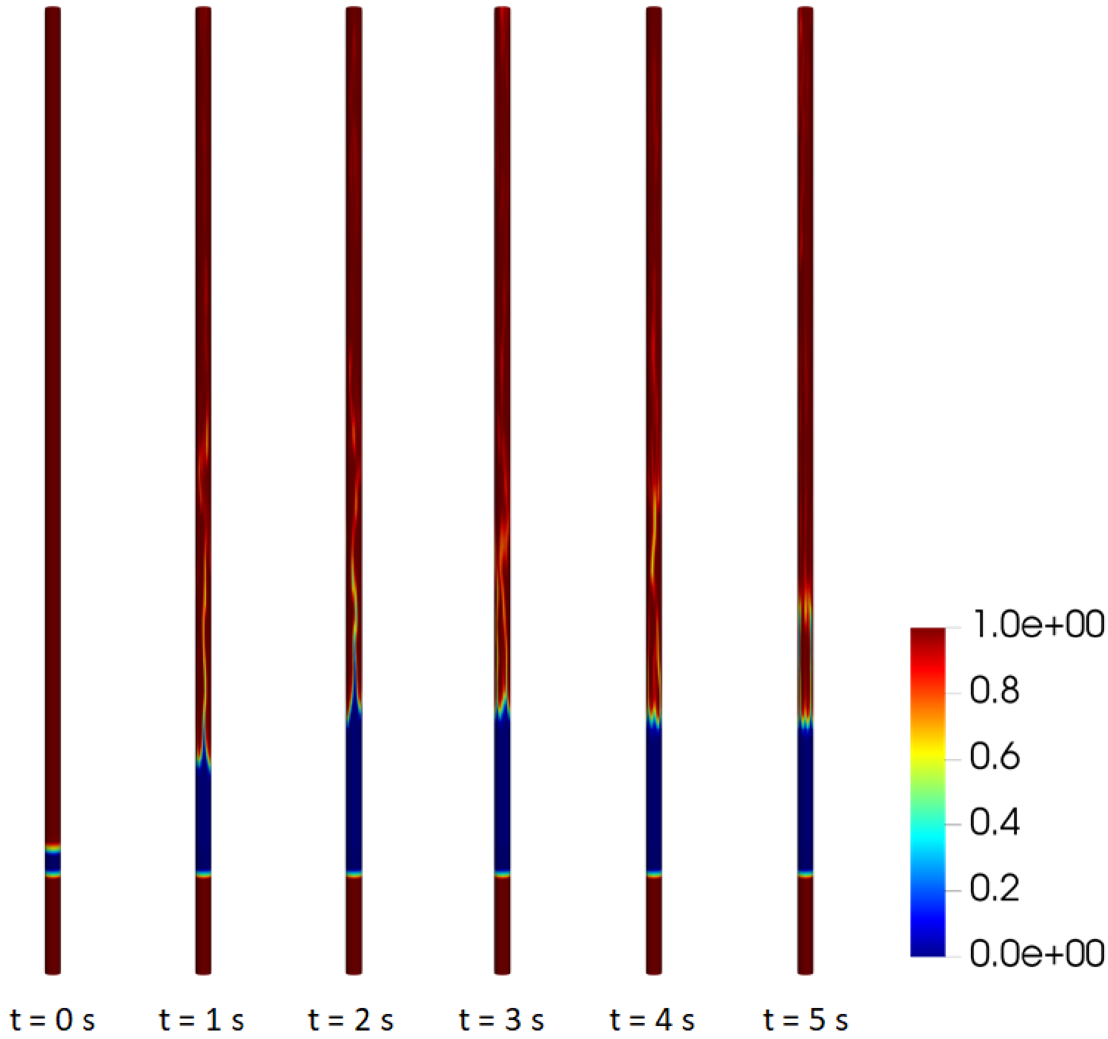

Source: The author (2022).

Figure 20 – Horizontal section of void fraction in churn flow at a height of 0.4 m at different times for the maximum Courant number of 0.05.

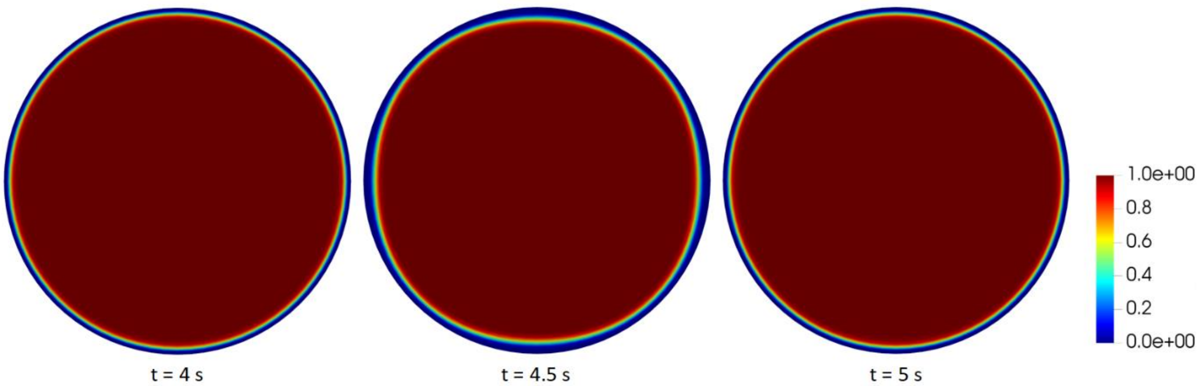

Source: The author (2022).

Figure 21 – Horizontal section of void fraction in churn flow at a height of 0.8 m at different times for the maximum Courant number of 0.05.

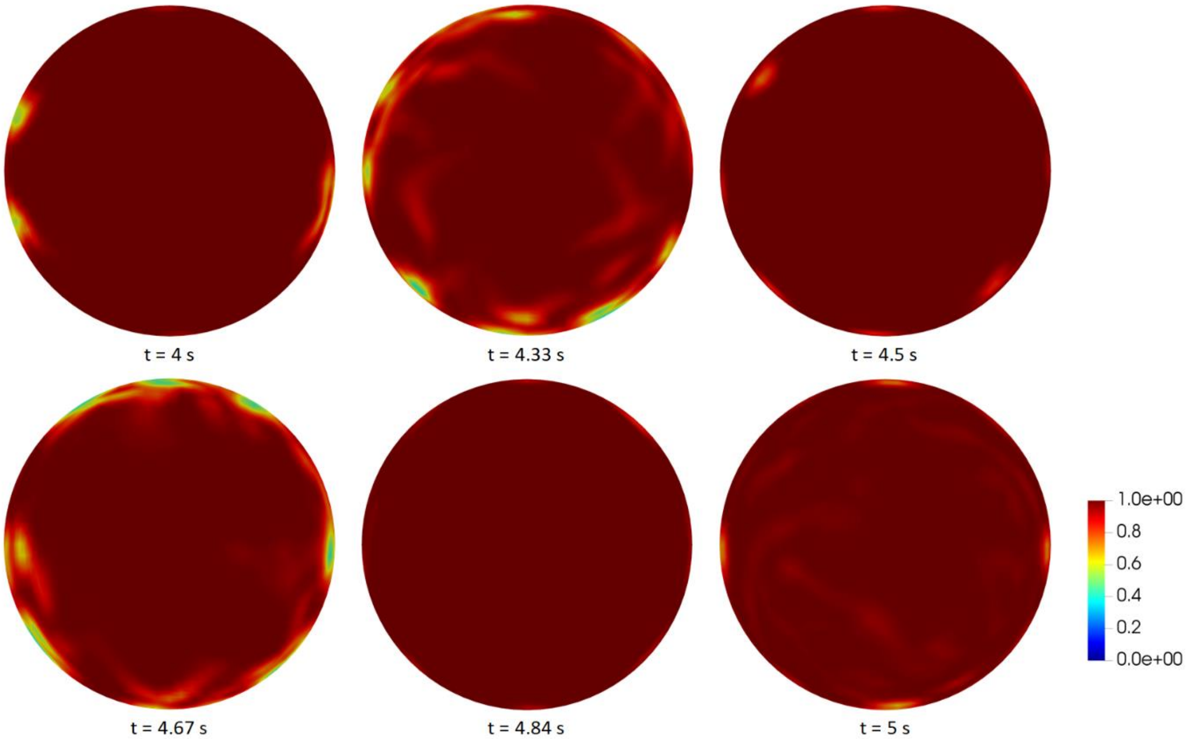

Source: The author (2022).

5.2 TRANSITION FLOW

Figure 22 shows the average air volumetric fraction in the flow at the transition between churn and annular patterns, with the results from Freitas (2021) and the Govan et al. (1991) experiments. In comparison to the experiments, simulations with maximum Courant number of 0.01 and 0.05 slightly underestimate the average value of the void fraction, while the cases with Courant of 0.125 and 0.25 overestimate it. In comparison to the simulations from Freitas (2021), all cases provide more accurate results. Results for the maximum Courant numbers of 0.25 and 0.125 are similar to the results from HyTAF.

Figure 22 – Void fraction in transition flow as function of time for the different maximum Courant numbers.

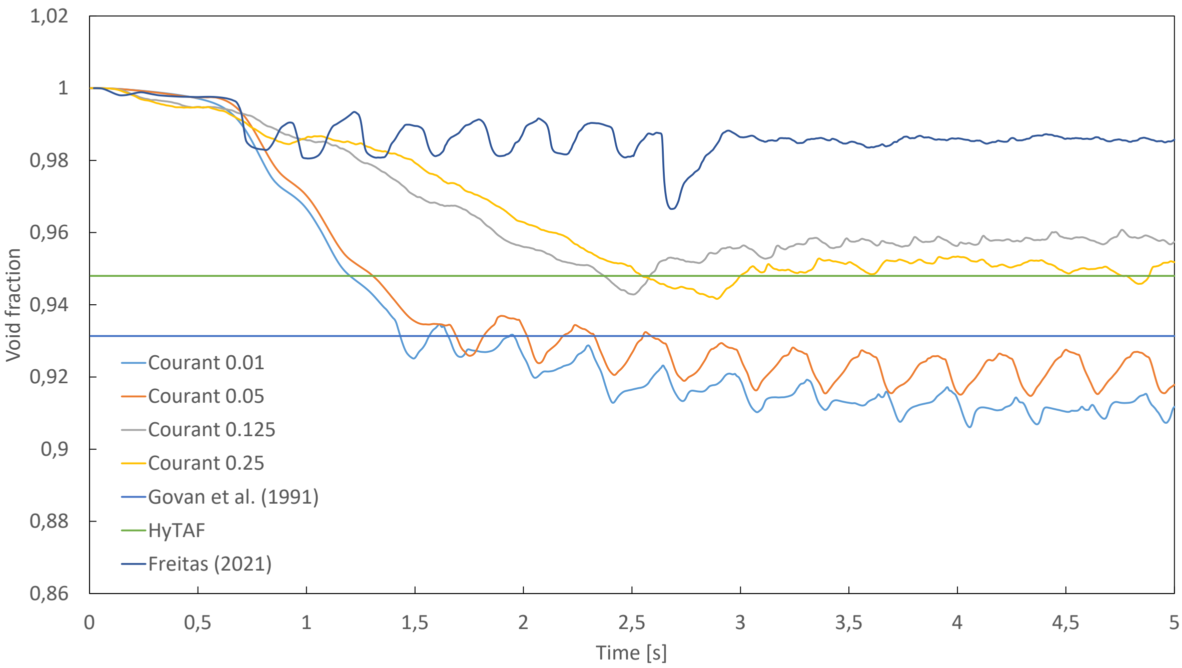

Source: The author (2022).

In these simulations, only the cases with maximum Courant of 0.01 and 0.05 show a significant oscillatory behavior. This indicates that smaller values of Courant, and consequently smaller time steps, allow a more detailed prediction of the flow.

Table 5 shows the average values of the void fraction, calculated at the last second of the simulation, for every case, and the relative errors in comparison to the experiments. In average, errors are lower than for churn flow. The case with maximum Courant number of 0.05 provides the best results, while the case with Courant of 0.125 provides the worst, although still in an acceptable range. Again, the smallest Courant number does not provide the most accurate results, in comparison to the experiments.

Table 5 – Average values of void fraction in transition flow at each case, with the relative errors in comparison to the experiments.

	0.01	**0.05**	**0.125**	**0.25**	**Freitas (2021)**	**Govan et al. (1991)**
Average	0.911	0.921	0.958	0.950	0.986	0.931
Error	2.18%	1.06%	2.88%	2.04%	5.85%	-

Source: The author (2022).

Figure 23 presents the flow pressure gradient at the transition between patterns. As in churn flow, pressure gradient is highly oscillatory and overestimated in the simulations. Table 6 shows the average values for each case, and the relative errors in comparison to the experiments. Even the most accurate case, with Courant of 0.125, provides inaccurate results. Again, the simulation performed by Freitas (2021) show a better prediction of the pressure gradient, showing that the radial liquid inlet generates higher pressure gradients in the flow than the axial inlet. Also, the HyTAF code can predict much more accurately the pressure gradient of the flow.

Figure 23 – Pressure gradient in transition flow as function of time for the different maximum Courant numbers.

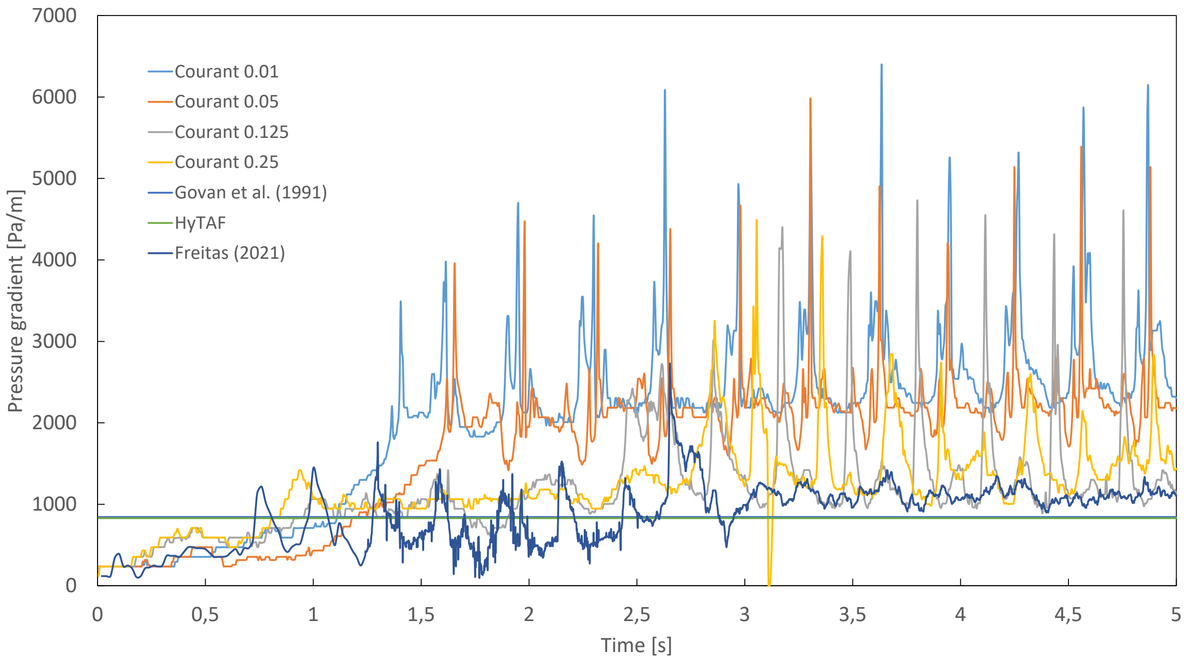

Source: The author (2022).

Table 6 – Average values of pressure gradient in transition flow at each case, with the relative errors in comparison to the experiments.

	0.01	**0.05**	**0.125**	**0.25**	**Freitas (2021)**	**Govan et al. (1991)**
Average	2750	2298	1394	1516	1111	844
Error	226%	172%	65.3%	79.7%	31.7%	-

Source: The author (2022).

In terms of visualization, flow at the transition between patterns is very similar to churn flow. For this reason, it was decided not to present the figures with the external and internal view of the void fraction in the flow, as it would not add new information to the analysis.

5.3 ANNULAR FLOW

Figure 24 shows the void fraction in annular flow for the different maximum Courant numbers, along with the results from Freitas (2021) and the Govan et al. (1991) experiments. In this case, the oscillations of void fraction are not as prominent as in the previous two; as expected for the annular flow pattern.

Table 7 shows the average values in the last second of the simulation for every case, and the relative errors. In comparison to the experiments, the simulation with maximum Courant of 0.125 provides the most accurate results. The simulation with Courant of 0.01 severely underestimate the void fraction in the flow, providing the least accurate values, even worse than the simulations from Freitas (2021), which significantly overestimate this parameter. Besides this case, all other simulations provide more accurate results for void fraction than the simulation from Freitas (2021), indicating again the advantages of using a proper geometry.

Figure 24 – Void fraction in annular flow as function of time for the different maximum Courant numbers.

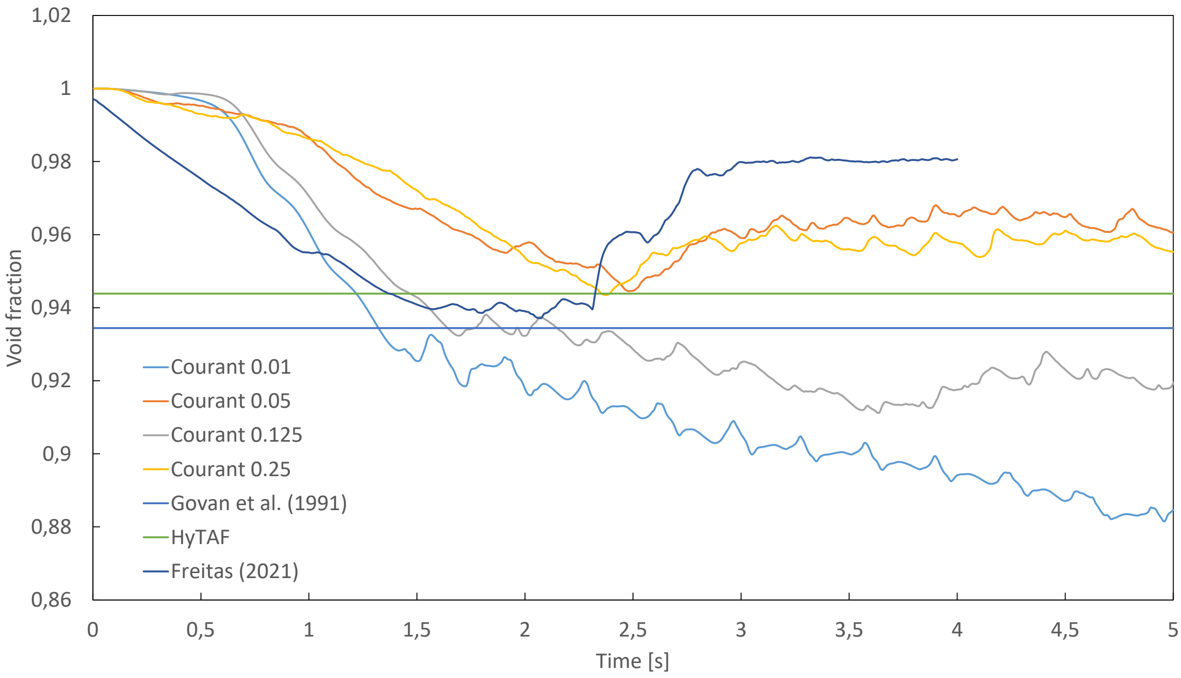

Source: The author (2022).

Table 7 – Average values of void fraction in annular flow at each case, with the relative errors in comparison to the experiments.

	0.01	0.05	0.125	0.25	Freitas (2021)	Govan et al. (1991)
Average	0.888	0.964	0.921	0.958	0.980	0.934
Error	4.94%	3.50%	1.41%	2.54%	4.90%	-

Source: The author (2022).

It is interesting to notice that the case with Courant of 0.01 does not reach "steady-state" in the first five seconds of simulation, as its void fraction is still decreasing at the end of the 5 s simulation. Of all simulations for the Courant number analysis, this is the only case where this happens. At all cases, the simulation with this value for maximum Courant number provides the lowest results for void fraction.

Figure 25 shows the pressure gradient in annular flow for different Courant numbers, and Table 8 provides the average values and the relative error in comparison to the experiments. Again, the case with maximum Courant number of 0.01 provides the worst results, severely overestimating the pressure gradient in the flow. The most accurate results are from the simulations with Courant of 0.05 and 0.25, although they also overestimate this parameter significantly. As in the previous cases, these simulations have shown a worse ability to predict the pressure gradient in the flow than the simulation from Freitas (2021).

Figure 25 – Pressure gradient in annular flow as function of time for the different maximum Courant numbers.

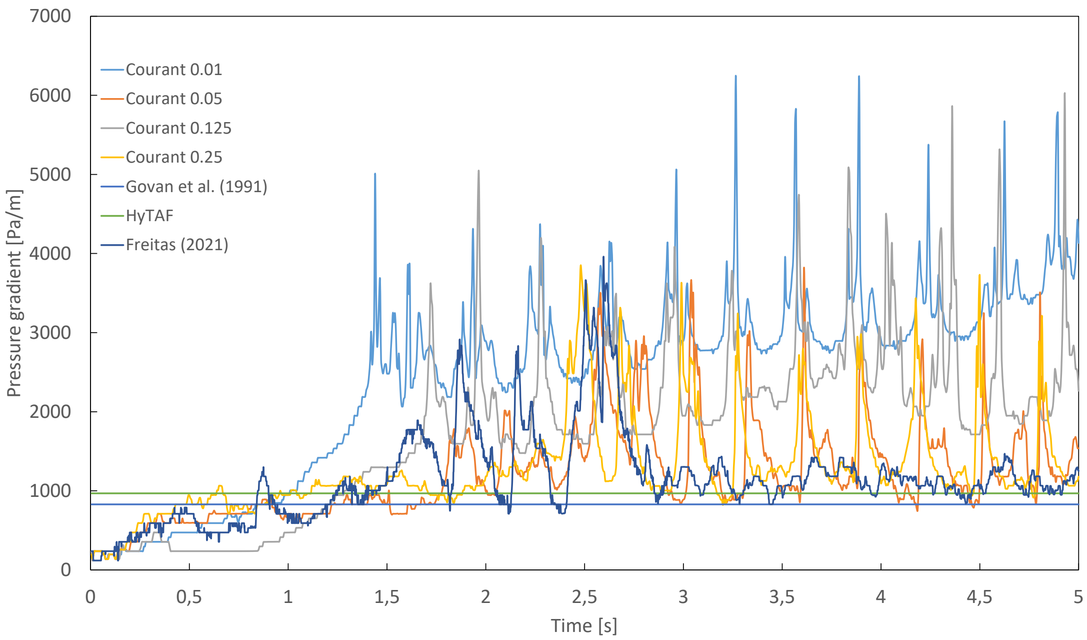

Source: The author (2022).

Table 8 – Average values of pressure gradient in annular flow at each case, with the relative errors in comparison to the experiments.

	0.01	**0.05**	**0.125**	**0.25**	**Freitas (2021)**	**Govan et al. (1991)**
Average	3446	1346	2463	1445	1113	828
Error	316%	62.5%	197%	74.5%	34.4%	-

Source: The author (2022).

Again, it was chosen not to present the figures with the external and internal view of the void fraction, as the visualization of annular flow was very similar to the two previous cases.

5.4 COMPUTATIONAL COSTS

Simulations were performed in computation capacities with 8 AMD ZEN 2 cores, with 16 GB of RAM. Cases with maximum Courant number of 0.01 took up to three months to conclude the simulations, while cases with Courant of 0.25 took less than two weeks. Therefore, although the Courant number influences the results of the simulations, using very small values might not be necessary, as they do not always improve the results, and require impracticable simulation times.

5.5 CONCLUDING REMARKS

Among many results and analysis obtained in the simulations presented, it was stated that the inlet geometry significantly influences the results, as expected. A more proper geometry, which represents better the experiments, yield better results for the void fraction in the flow, although overestimating the pressure gradient. This indicates that the method applied is not able to correctly predict the pressure gradient of the flow, which might be amended with the use of different models for drag coefficients, wall lubrication, and turbulence.

All simulations presented were performed using no wall lubrication and the Schiller and Naumann drag coefficient model, in version 7 of OpenFOAM®. This version was chosen in order to compare results with the simulations from Freitas (2021), who also used this version. Version 7 of the OpenFOAM® algorithm multiphaseEulerFoam has also implemented some other models for computing drag coefficient; two of them were tested in this research: the Ishii and Zuber model, and GidaspowErgunWenYu model, presented in section 3.1.4. Simulations with both these models generated instabilities that made the time step reach values on the order of 10^{-14} s, precluding the conclusion of the simulations and the analysis of results. Also, no wall lubrication models were implemented in the version 7 of the algorithm. The implementation of these models would require too much time, which was not available in the scope of this master's dissertation. For these reasons, it was preferred to update the software to version 9, that has a new version of the multiphaseEulerFoam already implemented with these enhancements.

Based on the results presented on this chapter, the maximum Courant number of 0.125 was chosen for the upcoming simulations, as it provides relatively accurate results, without the need for high computational times.

From the many differences between the algorithm multiphaseEulerFoam between the two versions, one of the most crucial is the turbulence modelling. Simulations performed in the first part of this work used the $k-\omega$ SST model implemented as a mixture model, so considering mixture thermophysical and flow properties. Version 9 of OpenFOAM® changes the implementation of the turbulence models, and does not consider mixture properties (except for the standard $k-\epsilon$ model); instead, it computes the turbulence for both phases separately (using a two-fluid approach). Thus, to begin the transition between versions, a comparison between them and an analysis of the turbulence models was required.

The other differences between the two versions are that version 9 considers an energy balance equation for each phase, even though in the present research it could be neglected due to the incompressibility of the phases and the absence of heat transfer. This version does not consider incompressible fluids; the gas-phase density follows the ideal-gas law. There are also differences in the numerical implementation, that include taking advantage of the hyperbolic nature of the full set of conservation equations as discussed by Alves (2014) and Städtke (2006), which make the solution more stable in version 9 (OPENFOAM, 2012).

6 TURBULENCE ANALYSIS

In this chapter, a comparison between versions 7 and 9 of the algorithm multiphaseEulerFoam is performed, with an analysis of different turbulence models. Again, simulations are performed for churn and annular flows, and the transition between them. For each pattern, three cases are analyzed. Case 1 consists of the simulations performed in version 7 of OpenFOAM® using the mixture $k-\omega$ SST model with averaged properties. It is the same case as presented in the previous section, with the maximum Courant number of 0.125. Case 2 used the mixture $k-\varepsilon$ model. In case 3, water is considered laminar, while air is modelled with the $k-\omega$ SST model, computed only for the air properties. Both cases 2 and 3 were simulated in version 9 of OpenFOAM®.

6.1 CHURN FLOW

Figure 26 – Void fraction in churn flow as function of time for cases 1, 2 and 3.

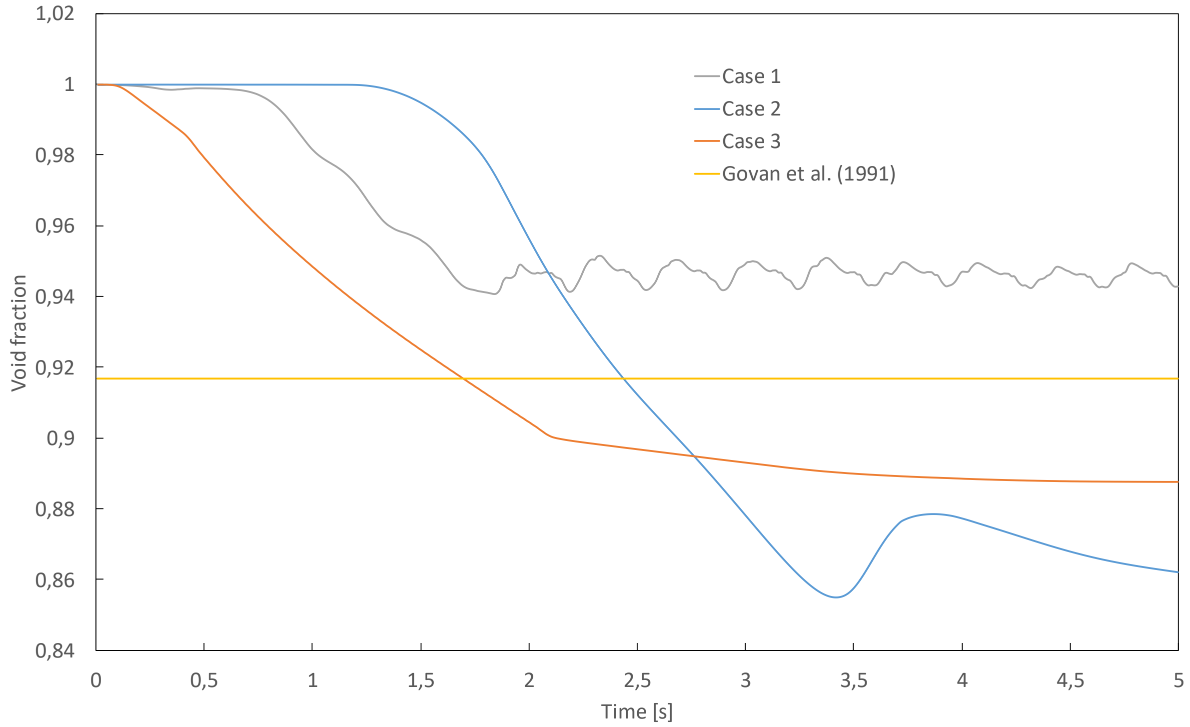

Source: The author (2022).

Figure 26 presents the void fraction in churn flow for the three cases with the average value from the Govan et al. (1991) experiments. Both simulations performed in version 9 of OpenFOAM® – cases 2 and 3 – underestimate the void fraction in comparison to the experiments, while the simulation in version 7 overestimates it. Also, it is interesting to notice that the simulations in version 9 do not present the wavy behavior as in Case 1, and that case 2 does not reach "steady-state" in the first five seconds of simulation.

Table 9 shows the average values for void fraction in each case, and the relative errors to the experiments. The simulation performed with the mixture $k - \varepsilon$ model provides the least accurate result, while Cases 1 and 3 both provide relatively good results for void fraction.

Table 9 – Average values of void fraction in churn flow at each case, with the relative errors in comparison to the experiments.

Case	**1**	**2**	**3**	**Govan et al. (1991)**
Average	0.946	0.868	0.888	0.917
Error	3.19%	5.30%	3.15%	-

Source: The author (2022).

Figure 27 presents the pressure gradient for each case, with average values from the experiments. It is obvious that the Case 2, that uses the mixture $k - \varepsilon$ model for turbulence , severely overestimates this parameter, reaching a peek more than 20 times higher than in the experiments. On the other hand, Case 3, that considers water laminar and models air with the $k - \omega$ SST model, provides highly accurate results, indicating that this might be a plausible consideration for simulating churn flow, although it is a highly turbulent pattern. Table 10 shows the average values and relative errors for each case, reaffirming that this model predicts best the pressure gradient in the flow.

It is known that the $k - \varepsilon$ model overpredicts the shear stress in the flow and is not ideal to model internal flows (SILVEIRA NETO, 2020). This, along with a possible poor modeling of the near-wall region, which is critical for this model, might be the source of the non-physical result obtained. On the other hand, considering the liquid laminar eliminates the need to treat turbulence in the near-wall region. A bad near-wall modelling could be the cause of inaccurate results when using only the $k - \omega$ SST model. This explains why, even though churn flow is turbulent, considering the liquid as laminar provides more accurate results.

Figure 27 – Pressure gradient in churn flow as function of time for cases 1, 2 and 3.

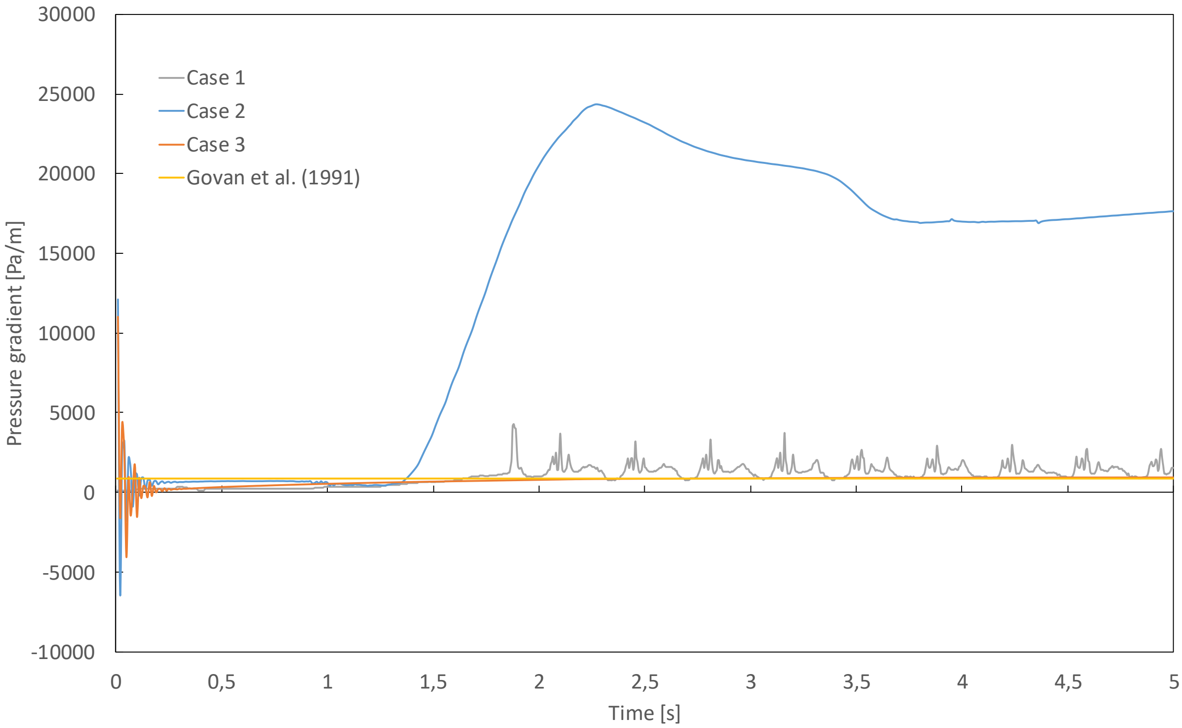

Source: The author (2022).

Table 10 – Average values of pressure gradient in churn flow at each case, with the relative errors in comparison to the experiments.

Case	**1**	**2**	**3**	**Govan et al. (1991)**
Average	1376	17203	933	883
Error	55.8%	1848%	5.65%	-

Source: The author (2022).

Besides the average values, a considerable difference in the solution behavior can be seen between the two versions. Simulations performed in version 9 present a highly oscillatory behavior at the beginning of the solution, until converging. At "steady-state", no wavy behavior is seen for void fraction and pressure gradient. The simulations performed in version 7, on the other hand, begin with a smooth solution, but provide oscillatory results at "steady-state".

For a better understanding of the phenomena present in these flows, the external and internal view of the void fraction are presented for Case 3 in the next subsections.

6.1.1 Case 3

Figure 28 shows the external view of the void fraction in churn flow for case 3, which considers water laminar and models air with the $k-\omega$ SST model. As in case 2, liquid film does not pulverize, however, here it ascends with a higher velocity, reaching the pipe outlet sooner. At 5 seconds, almost all cells adjacent to the wall, above the liquid inlet, contain only liquid. The cells adjacent to the pipe outlet present high air volumetric fractions as a numerical effect due to the boundary conditions.

Figure 28 – External view of the air volumetric fraction in churn flow for case 3.

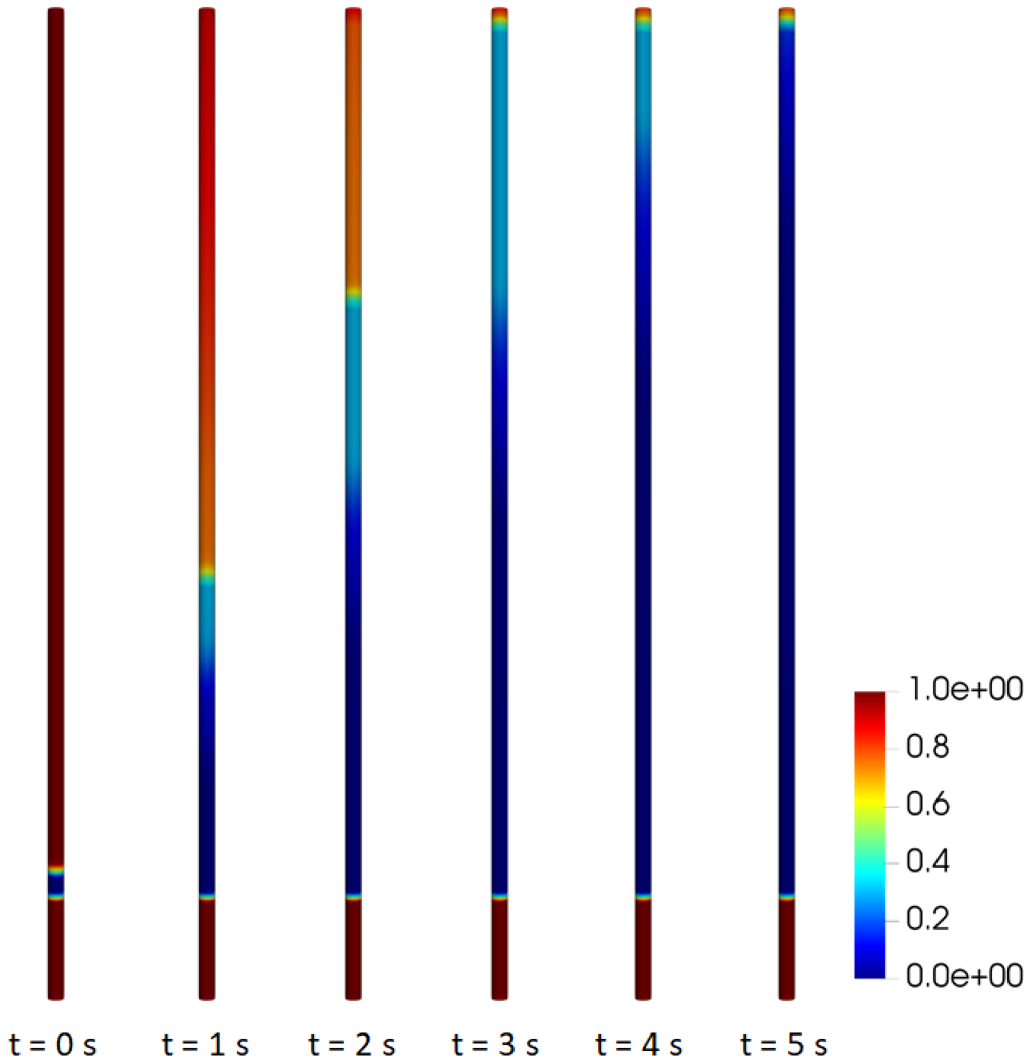

Source: The author (2022).

Figure 29 and Figure 30 show the cross-sectional view of the void fraction at heights of 0.4 m and 0.8 m, respectively. In this case, film thickness is significantly lower than in all previous simulations, which explains the higher liquid velocity. Also, the water film does not pulverize, no water droplets or filaments are seen, and interface is not wavy. Flow pattern is more like annular than churn.

Figure 29 – Cross section of void fraction in churn flow at a height of 0.4 m at different times for case 3.

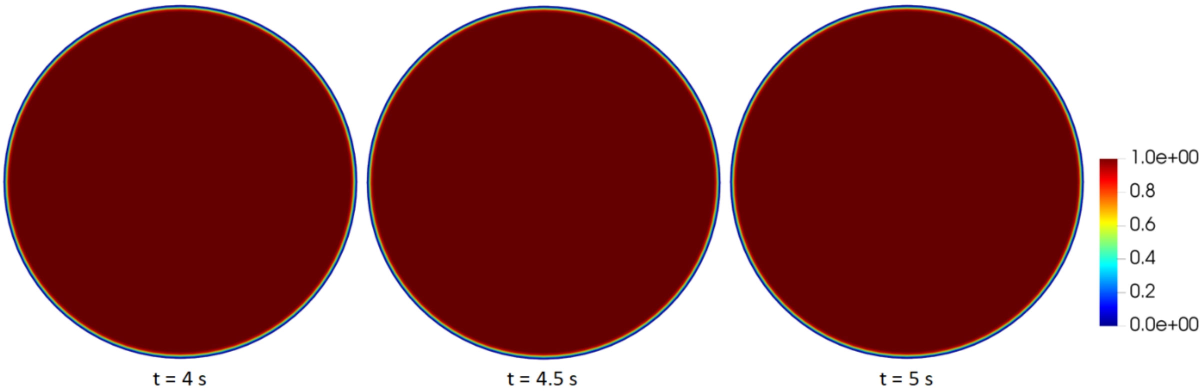

Source: The author (2022).

Figure 30 – Cross section of void fraction in churn flow at a height of 0.8 m at different times for case 3.

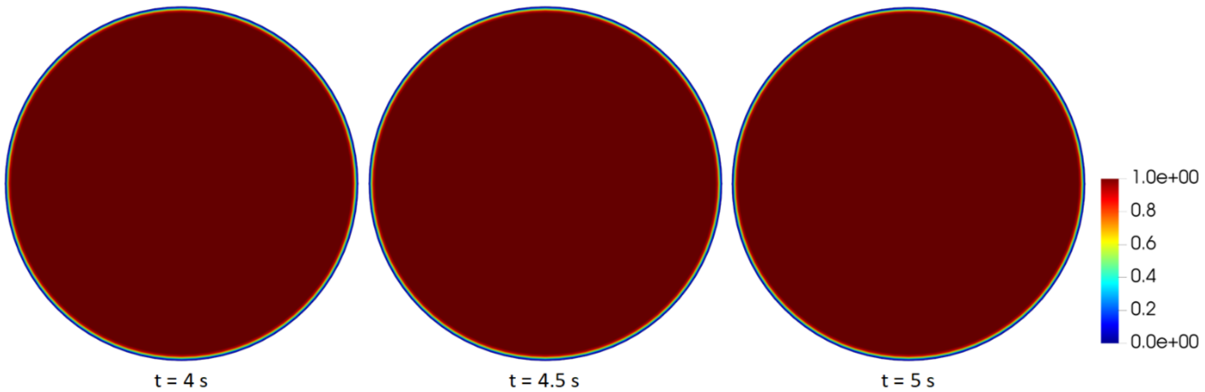

Source: The author (2022).

6.2 TRANSITION FLOW

Figure 31 shows the void fraction as function of time for each case in the transition between patterns. Simulations of case 3 were only performed for 4 seconds due to computational time constraints. Again, simulations in version 9 of OpenFOAM®

underestimate the void fraction in comparison to the experiments and to version 7, and no oscillatory behavior is seen in the void fraction for these cases.

Table 11 presents the average values for each case and relative errors in comparison to the experiments. As for churn flow, case 2 provides the least accurate results. Here, case 1 provides the most accurate.

Figure 31 – Void fraction in transition flow as function of time for cases 1, 2 and 3.

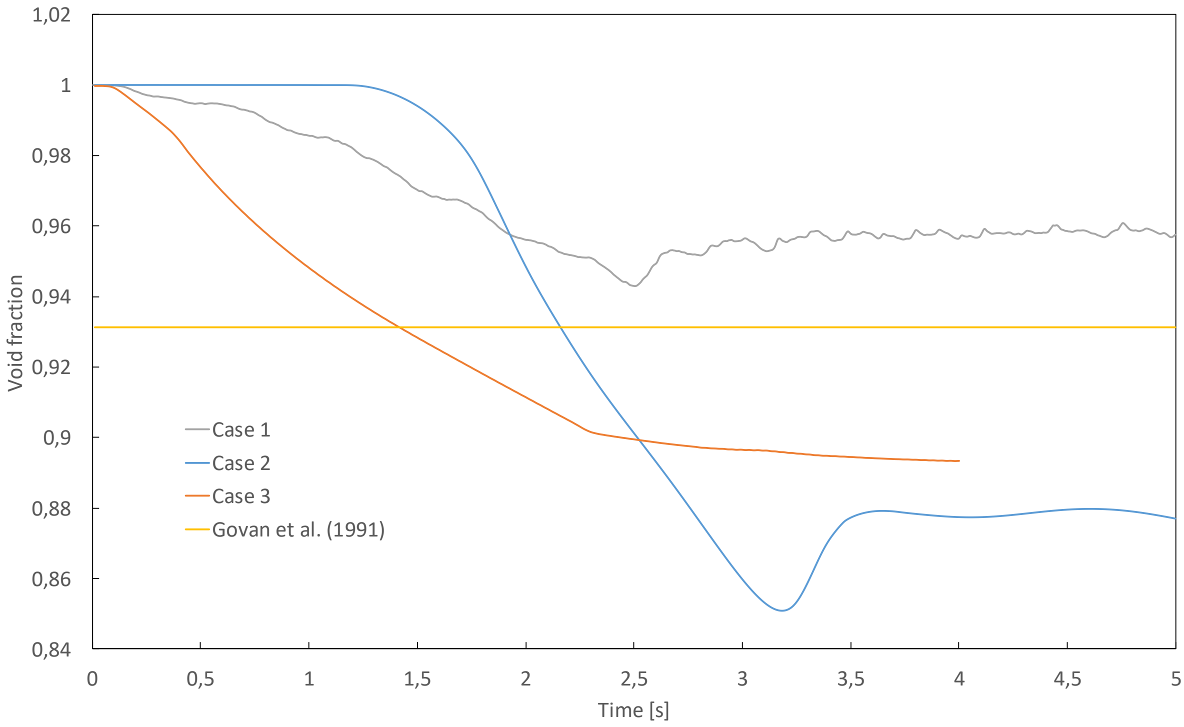

Source: The author (2022).

Table 11 – Average values of void fraction in transition flow at each case, with the relative errors in comparison to the experiments.

Case	**1**	**2**	**3**	**Govan et al. (1991)**
Average	0.958	0.878	0.895	0.931
Error	2.88%	5.67%	3.94%	-

Source: The author (2022).

Figure 32 presents the pressure gradient for each case. Case 2, as in the previous case, significantly overestimate this parameter, indicating again that the $k - \varepsilon$ model does not provide accurate results for these flows. Table 12 shows the average values and relative errors for each case, showing that, again, considering water as laminar significantly improves the pressure gradient prediction.

Figure 32 – Pressure gradient in transition flow as function of time for cases 1, 2 and 3.

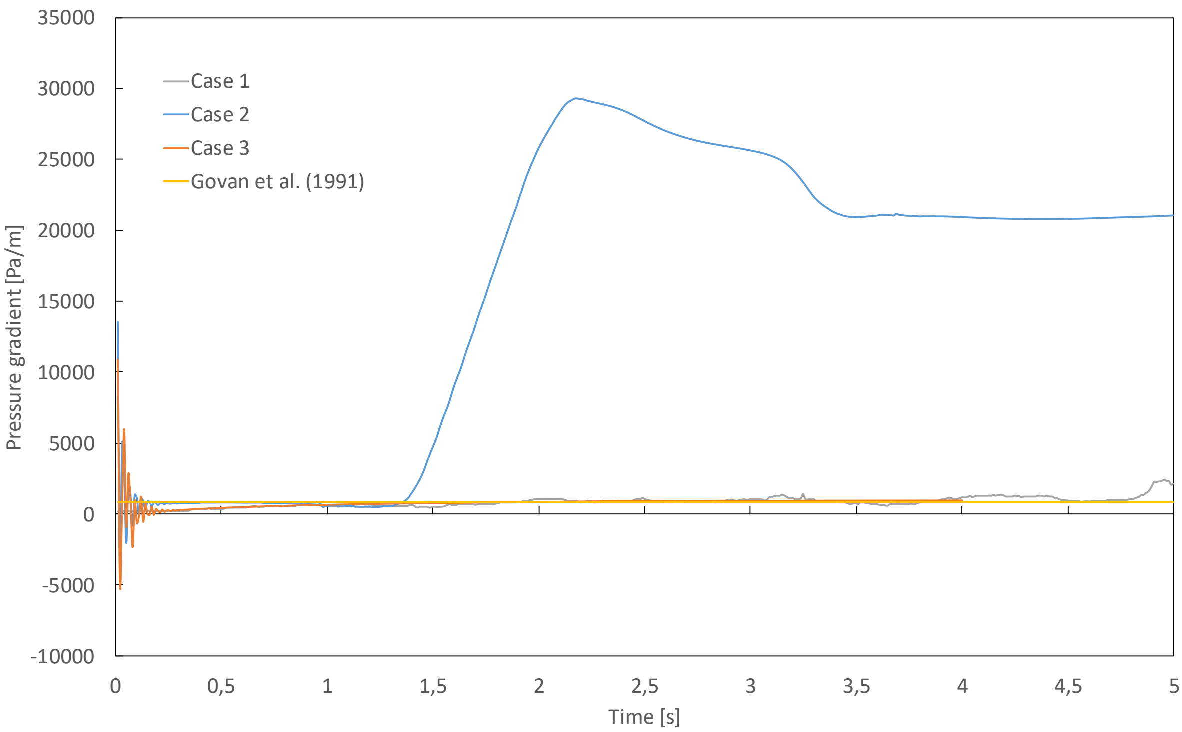

Source: The author (2022).

Table 12 – Average values of pressure gradient in transition flow at each case, with the relative errors in comparison to the experiments.

Case	**1**	**2**	**3**	**Govan et al. (1991)**
Average	1394	20871	939	843
Error	65.2%	2374%	11.31%	-

Source: The author (2022).

In terms of flow visualization, the transition between patterns was very similar to the churn flow, so a more detailed visualization of the void fraction is omitted here.

6.3 ANNULAR FLOW

Figure 33 shows the air volumetric fraction at each case in annular flow. Table 13 shows the average values at the last second of simulation and the relative errors in comparison to the experimental data from Govan et al. (1991). For annular flow, all cases underestimate the void fraction, with case 1 providing the most accurate results, and case 3, the least accurate. As in the previous cases, simulations performed in version 9 of OpenFOAM® do not show a wavy behavior.

Figure 33 – Void fraction in annular flow as function of time for cases 1, 2 and 3.

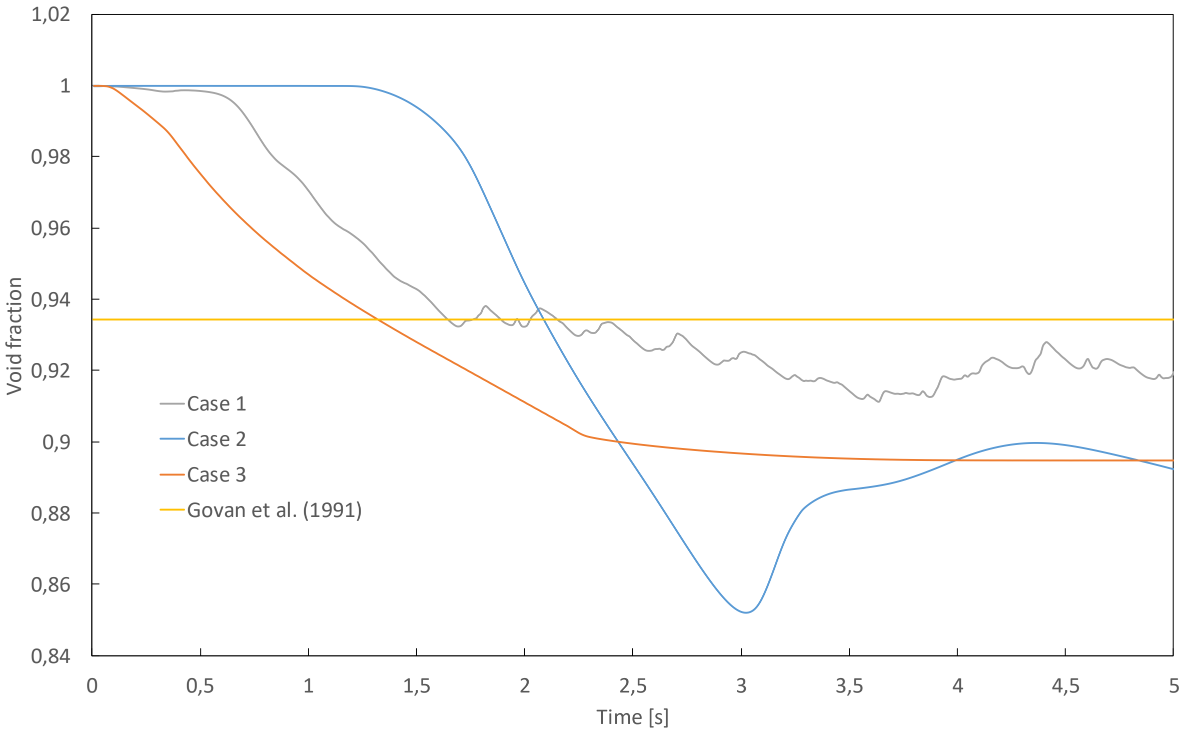

Source: The author (2022).

Table 13 – Average values of void fraction in transition flow at each case, with the relative errors in comparison to the experiments.

Case	**1**	**2**	**3**	**Govan et al. (1991)**
Average	0.921	0.897	0.894	0.934
Error	1.41%	3.98%	4.24%	-

Source: The author (2022).

Figure 34 shows the pressure gradient in annular flow for each case. Again, case 2, that uses the $k-\varepsilon$ model, provides absurd results. Case 3, that considers water laminar and uses $k-\omega$ SST to model turbulence in the air, provides the most accurate pressure gradients, as can be seen in Table 14, which presents the average values and relative errors for each case.

Figure 34 – Pressure gradient in annular flow as function of time for cases 1, 2 and 3.

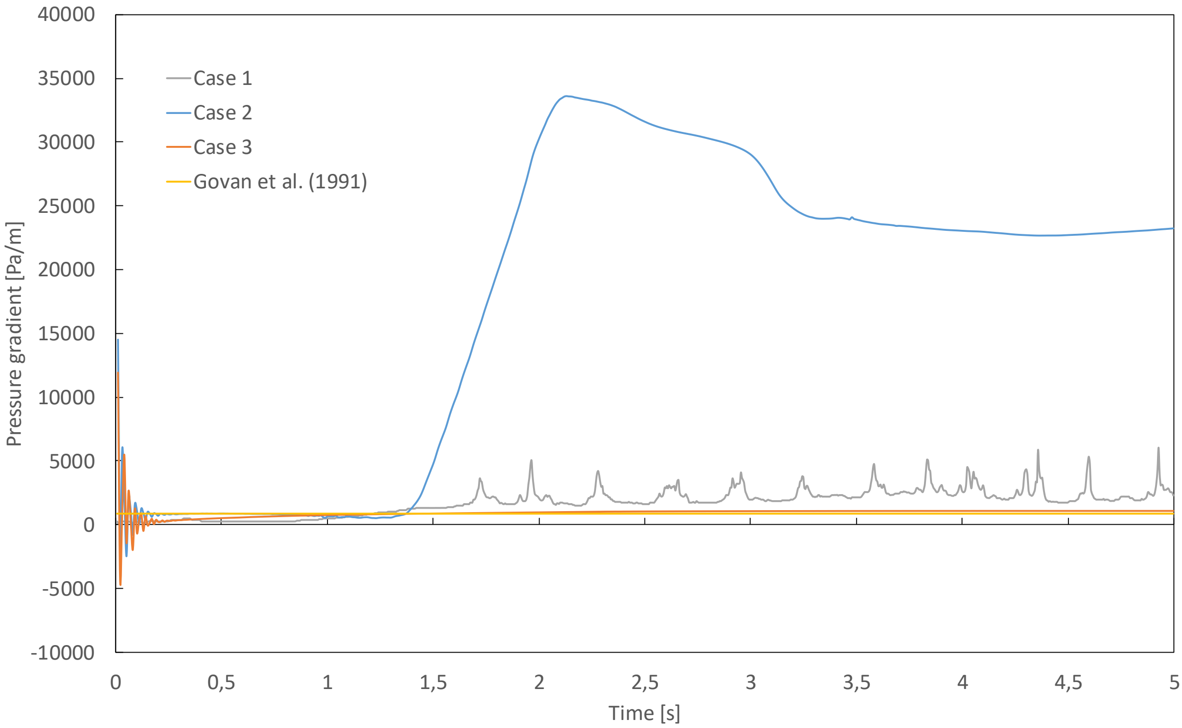

Source: The author (2022).

Table 14 – Average values of pressure gradient in transition flow at each case, with the relative errors in comparison to the experiments.

Case	1	2	3	Govan et al. (1991)
Average	2463	22874	1066	828
Error	197%	2662%	28.8%	-

Source: The author (2022).

6.4 CONCLUDING REMARKS

The case in which water is considered laminar and air is modelled with the $k - \omega$ SST model provides the best results for pressure gradient, while still yielding acceptable results for void fraction. Thus, this model was chosen for the next set of simulations performed in version 9 of OpenFOAM®, which intend to assess the influence of the wall lubrication and drag coefficient models. These simulations are still in a preliminary phase, as using these models tend to bring instabilities to the simulations, causing its divergence after a certain time. The solution to this problem is not clear yet. Some simulation parameters – as relaxation factors, number of iterations, solver type and preconditioner – and discretization and interpolation schemes have been tested, however, no satisfactory setup has been achieved.

Appendixes A and B bring the preliminary results for the wall lubrication and drag coefficient analysis, respectively, in churn flow, showing that these parameters, especially the wall lubrication, barely influence the results.

7 CONCLUSIONS

In the present work, a numerical investigation of air-water vertical flows was conducted. Simulations were performed for three different mass fluxes, corresponding to the churn and annular patterns, and the transition between them, according to the experiments performed by Govan et al. (1991). A hybrid methodology, which combines the two-fluid and volume of fluid models, was used to capture both the dispersed and segregated characteristics of churn and annular flows. The OpenFOAM® algorithm multiphaseEulerFoam was used for the simulations.

In the first part of this research, simulations were performed in OpenFOAM® version 7, using the $k-\omega$ SST model for turbulence. The main objectives were to evaluate the ability of the method applied to simulate gas-liquid flows, analyzing the aspects and phenomenon of these flows, and comparing important parameters with experimental data. Also, the influence of the maximum Courant number of the simulation and the geometry of the liquid inlet in the results were addressed.

Simulations were able to capture some phenomena observed in churn and annular flows, as the formation of a liquid film and the wavy interface between phases. However, liquid film was only present in the near-entry region, pulverizing after reaching a certain height, which was not expected. Also, the presence of liquid droplets and filaments was significantly underestimated in the simulations, which might be a consequence of using a coarse mesh. The visualization of the flow in the churn and annular patterns, and the transition between them, provided very similar results. In fact, in the three cases, flow presented characteristics more like annular flow than to churn, especially in the near-inlet region. Churn flow characteristics as the high presence of filaments and the oscillatory movement of liquid were not observed.

In comparison to the Govan et al. (1991) experiments, the simulations performed in the first part of this research provided relatively accurate results for the void fraction, with a maximum relative error of 6.37%, although significantly overestimating the pressure gradient of the flow, with maximum error of 316%. This indicates a poor ability to predict the pressure drop, which might be consequence of a poor modelling of the momentum exchange between the two phases, between phases and wall, or even a poor turbulence modelling.

It is known that the pressure gradient of the flow tends to decrease from churn to annular flow (GOVAN et al., 1991; OWEN, 1986). Yet, in the simulations, it increased with the mass fluxes. However, this was not unexpected, as simulations of churn flow presented, in fact, a behavior like the annular pattern, without the oscillatory movement and high presence of filaments which increase pressure gradient.

A comparison to the simulations performed by Freitas (2021) was also conducted in order to assess the influence of the liquid inlet geometry on the results. Freitas (2021) simulated the same mass fluxes considering only the upper region of the test section from Govan et al. (1991), above the liquid inlet, ignoring the effects of the radial liquid injection. The simulations performed in the present research present accurate results for void fraction, but severely overestimate the pressure gradient, while the results from Freitas (2021) are the opposite. The use of a proper geometry increases the ability of predicting the void fraction in the flow. However, it worsens the prediction of the pressure drop, by increasing both the frictional and gravitational pressure gradient – since in these simulations void fraction is lower and mixture density is higher.

Furthermore, the simulations performed by Freitas (2021), despite using a lower maximum Courant number than in the present work, present a much lower oscillatory behavior. This indicates that the waves present in the flow arise at the inlet region and are transported with the flow, since only with a proper representation of the liquid inlet this phenomenon is seen.

An analysis of the maximum Courant number of the simulation was conducted, considering Courant values of 0.01, 0.05, 0.125, and 0.25. The Courant number is an important parameter on the convergence of the solution in CFD simulations. It was shown that, for the three cases analyzed, this simulation parameter significantly influences the results and behavior of the solution. The use of lower maximum Courant numbers does not always provide more accurate results, and all simulations performed presented good convergence. These results indicate that it might not be necessary to use extremely small values for the maximum Courant number, as it might not provide more accurate results, despite requiring much longer simulations. For the objectives of the present work, the Courant of 0.125 was considered the best, and was chosen for the simulations of the second part of the research.

Searching for a better prediction of the flow pressure gradient, an evaluation of other models for computing drag forces, wall lubrication and turbulence was desired. First, simulations of the other drag coefficient models implemented in OpenFOAM® version 7 were conducted. However, these models introduce severe instabilities to the flow, which precluded the convergence of the simulations. Wall lubrication models were implemented only in version 9 of the software and implementing them in version 7 would require too much time, which was not available. For these reasons, it was chosen to update the software to version 9.

There are many differences between the solution procedure of the multiphaseEulerFoam algorithm in versions 7 and 9. One of the most important, is the turbulence modelling, which, in version 9, is computed for each phase separately. Thus, in the second part of the present work, an analysis of the turbulence models was performed, with a comparison between results from the two versions of the OpenFOAM® software. Three cases were considered for each of pattern analyzed: case 1, which is the simulation used in the Courant number analysis, was simulated in version 7, with the $k-\omega$ SST turbulence model; case 2 was simulated in version 9, using the mixture $k-\varepsilon$ model; and case 3, also simulated in version 9, considered water as a laminar fluid and air was modelled with $k-\omega$ SST.

Significant differences were found between the results from the two different versions of the OpenFOAM®. While version 7 of the algorithm provided oscillatory results for the void fraction and pressure gradient, in version 9 solution is highly oscillatory at the beginning, converging to a smooth solution after a certain time. Both cases simulated in version 9 showed less liquid film pulverization than in version 7. Also, in version 9, the interface between phases is not wavy and no filaments are seen in the gas core.

The comparison between turbulence models also provided interesting results. Case 1, as already stated, provided accurate results for void fraction, while overestimating the pressure gradient. The mixture $k-\varepsilon$ model, used in case 2, provided even worst results than case 1, overestimating the pressure gradient by more than 20 times, and providing also the least accurate results for void fraction. These results reiterate that the $k-\varepsilon$ model is not accurate for internal flows. Case 3, which considered water laminar and modelled air with the $k-\omega$ SST model, despite providing slightly worse results for the void fraction than case 1, provided the most accurate results for pressure gradient, decreasing the relative error to the experiments by up to more than 10 times, in comparison to case 1.

In summary, the method used in the present research was capable of providing relatively accurate results, despite not being able to capture all phenomena involved in churn and annular flows, especially away from the inlet region. The main conclusions that can be drawn from this work are:

- Extremely small values for the maximum Courant number are not necessary. A Courant of 0.125 provides accurate results and good convergence;
- Using an accurate geometry, as expected, allows a better prediction of the flow properties;

- Versions 7 and 9 of the multiphaseEulerFoam algorithm provide significantly different results, and the selection between them should be made carefully. At each case, some aspects of the two-phase flows are captured, while others are not;
- Turbulence modelling is crucial for an accurate prediction of the flow pressure gradient. Modelling water as laminar and air using the $k - \omega$ SST model provides the most accurate results from the models compared.

7.1 RECOMMENDATIONS FOR FUTURE WORK

During this research, some interesting topics were identified as relevant for further investigation. Simulating the entire test section used in the experiments could provide more accurate and detailed results, allowing a better understanding of the phenomena involved in these flows. Also, the use of a finer mesh, with better aspect ratio, might allow a more detailed visualization of flow phenomena. To conclude, it would be interesting to use the methodology applied at this work, with the conclusions obtained, to investigate the phenomena of flooding and flow reversal, which constitute serious problems of gas-liquid flows and might be better understood with adequate simulations.

REFERENCES

AHMAD, M.; PENG, D. J.; HALE, C. P.; WALKER, S. P.; HEWITT, G. F. Droplet Entrainment in Churn Flow. *In*: 7TH INTERNATIONAL CONFERENCE OF MULTIPHASE FLOW (ICMF-2010) 2010, Florida, USA. **Anais** [...]. Florida, USA

ALIYU, Aliyu Musa; BABA, Yahaya Danjuma; LAO, Liyun; YEUNG, Hoi; KIM, Kyung Chun. Interfacial friction in upward annular gas–liquid two-phase flow in pipes. **Experimental Thermal and Fluid Science**, *[S. l.]*, v. 84, p. 90–109, 2017. DOI: 10.1016/J.EXPTHERMFLUSCI.2017.02.006.

ALVES, Marcus Vinícius C.; WALTRICH, Paulo J.; GESSNER, Tobias R.; FALCONE, Gioia; BARBOSA, Jader R. Modeling transient churn-annular flows in a long vertical tube. **International Journal of Multiphase Flow**, *[S. l.]*, v. 89, p. 399–412, 2017. DOI: 10.1016/j.ijmultiphaseflow.2016.12.001.

ALVES, Marcus Vinícius Canhoto. **Modelagem numérica do escoamento transiente churnanular em tubulações verticais e sua aplicação na simulação de carga de líquido em poços de gás**. 2014. Universidade Federal de Santa Catarina, *[S. l.]*, 2014.

ANTAL, S. P.; LAHEY, R. T.; FLAHERTY, J. E. Analysis of phase distribution in fully developed laminar bubbly two-phase flow. **International Journal of Multiphase Flow**, *[S. l.]*, v. 17, n. 5, p. 635–652, 1991. DOI: 10.1016/0301-9322(91)90029-3.

AZZOPARDI, B. J. Disturbance wave frequencies, velocities and spacing in vertical annular two-phase flow. **Nuclear Engineering and Design**, *[S. l.]*, v. 92, n. 2, p. 121–133, 1986. DOI: 10.1016/0029-5493(86)90240-2.

AZZOPARDI, B. J. **Gas-liquid flows**. New York: Begell House, 2006.

AZZOPARDI, Barry; HILLS, John. Flow Patterns, Transitions and Models for Specific Flow Patterns. *[S. l.]*, p. 1–77, 2003. DOI: 10.1007/978-3-7091-2538-0_1.

BARBOSA, J. R.; GOVAN, A. H.; HEWITT, G. F. Visualisation and modelling studies of churn flow in a vertical pipe. **International Journal of Multiphase Flow**, *[S. l.]*, v. 27, n. 12, p. 2105–2127, 2001. DOI: 10.1016/S0301-9322(01)00048-9.

BEHZADI, A.; ISSA, R. I.; RUSCHE, H. Modelling of dispersed bubble and droplet flow at high phase fractions. **Chemical Engineering Science**, *[S. l.]*, v. 59, n. 4, p. 759–770, 2004. DOI: 10.1016/J.CES.2003.11.018.

BELT, R. J.; VAN’T WESTENDE, J. M. C.; PORTELA, L. M. Prediction of the interfacial shear-stress in vertical annular flow. **International Journal of Multiphase Flow**, *[S. l.]*, v. 35, n. 7, p. 689–697, 2009. DOI: 10.1016/J.IJMULTIPHASEFLOW.2008.12.003.

BELT, R. J.; VAN’T WESTENDE, J. M. C.; PRASSER, H. M.; PORTELA, L. M. Time and spatially resolved measurements of interfacial waves in vertical annular flow. **International Journal of Multiphase Flow**, *[S. l.]*, v. 36, n. 7, p. 570–587, 2010. DOI: 10.1016/J.IJMULTIPHASEFLOW.2010.03.004.

BHARATHAN, D.; WALLIS, G. B. Air-water countercurrent annular flow. **International Journal of Multiphase Flow**, *[S. l.]*, v. 9, n. 4, p. 349–366, 1983. DOI: 10.1016/0301-9322(83)90093-9.

BOCHIO, Gustavo; CELY, Marlon M. H.; TEIXEIRA, Arthur F. A.; RODRIGUEZ, Oscar M. H. Experimental and numerical study of stratified viscous oil–water flow. **AIChE Journal**, *[S. l.]*, v. 67, n. 6, p. e17239, 2021. DOI: 10.1002/AIC.17239.

BRACKBILL, J. U.; KOTHE, D. B.; ZEMACH, C. A continuum method for modeling surface tension. **Journal of Computational Physics**, *[S. l.]*, v. 100, n. 2, p. 335–354, 1992. DOI: 10.1016/0021-9991(92)90240-Y.

BROWN, D. J.; JENSEN, A.; WHALLEY, P. B. **Non-Equilibrium Effects in Heated and Unheated Annular Two-Phase Flow**. [s.l: s.n.].

CERNE, Gregor; PETELIN, Stojan; TISELJ, Iztok. Coupling of the Interface Tracking and the Two-Fluid Models for the Simulation of Incompressible Two-Phase Flow. **Journal of Computational Physics**, *[S. l.]*, v. 171, n. 2, p. 776–804, 2001. DOI: 10.1006/jcph.2001.6810.

CHAKRAVARTHY, Sukumar R.; ANDERSON, Dale A.; SALAS, Manuel D. SPLIT COEFFICIENT MATRIX METHOD FOR HYPERBOLIC SYSTEMS OF GASDYNAMIC EQUATIONS. **AIAA Paper**, *[S. l.]*, 1980. DOI: 10.2514/6.1980-268.

CIONCOLINI, Andrea; THOME, John R. Prediction of the entrained liquid fraction in vertical annular gas–liquid two-phase flow. **International Journal of Multiphase Flow**, *[S. l.]*, v. 36, n. 4, p. 293–302, 2010. DOI: 10.1016/J.IJMULTIPHASEFLOW.2009.11.011.

COSTIGAN, G.; WHALLEY, P. B. Slug flow regime identification from dynamic void fraction measurements in vertical air-water flows. **International Journal of Multiphase Flow**, *[S. l.]*, v. 23, n. 2, p. 263–282, 1997. DOI: 10.1016/S0301-9322(96)00050-X.

DA RIVA, Enrico; DEL COL, Davide. Numerical simulation of churn flow in a vertical pipe. **Chemical Engineering Science**, *[S. l.]*, v. 64, n. 17, p. 3753–3765, 2009. DOI: 10.1016/j.ces.2009.04.049.

DALLMAN, John C. Investigation of separated flow model in annular gas-liquid two-phase flows. *[S. l.]*, p. 207, 1979.

DOBRAN, Flavio. Hydrodynamic and heat transfer analysis of two-phase annular flow with a new liquid film model of turbulence. **International Journal of Heat and Mass Transfer**, *[S. l.]*, v. 26, n. 8, p. 1159–1171, 1983. DOI: 10.1016/S0017-9310(83)80170-7.

FERZIGER, Joel H.; PERIC, Milovan. **Computational Methods for Fluid Dynamics third, rev. edition**. 3. ed. Berlin: Springer, 2002.

FRANK, T. Advances in computational fluid dynamics (CFD) of 3-dimensional gas-liquid multiphase flows. *In*: NAFEMS SEMINAR “SIMULATION OF COMPLEX FLOWS (CFD)” 2005, Wiesbaden, Germany. **Anais** [...]. Wiesbaden, Germany p. 1.

FREITAS, Larissa Steiger De. **NUMERICAL SIMULATION OF VERTICAL ANNULAR AND CHURN AIR-WATER TWO-PHASE FLOWS**. 2021. Universidade do Estado de Santa Catarina, *[S. l.]*, 2021.

GIDASPOW, Dimitri. **Multiphase flow and fluidization : continuum and kinetic theory descriptions**. [s.l.] : Academic Press, 1994.

GOVAN, A. H.; HEWITT, G. F.; RICHTER, H. J.; SCOTT, A. Flooding and churn flow in vertical pipes. **International Journal of Multiphase Flow**, *[S. l.]*, v. 17, n. 1, p. 27–44, 1991. DOI: 10.1016/0301-9322(91)90068-E.

HALL TAYLOR, Nicholas Simon. **Interfacial wave phenomena in vertical annular two-phase flow**. 1967. University of Cambridge, Cambridge, 1967. Disponível em: https://www.repository.cam.ac.uk/handle/1810/251043. Acesso em: 4 out. 2021.

HERNANDEZ-PEREZ, V.; ABDULKADIR, M.; AZZOPARDI, B. J. Grid generation issues in the CFD modelling of two-phase flow in a pipe. **Journal of Computational Multiphase Flows**, *[S. l.]*, v. 3, n. 1, p. 13–26, 2011. DOI: 10.1260/1757-482X.3.1.13.

HEWITT, G. F. **Analysis of annular two-phase flow: application of the Dukler analysis to vertical upward flow in a tube**. [s.l: s.n.].

HEWITT, G. F.; GOVAN, A. H. Phenomenological modelling of non-equilibrium flows with phase change. **International Journal of Heat and Mass Transfer**, *[S. l.]*, v. 33, n. 2, p. 229–242, 1990. DOI: 10.1016/0017-9310(90)90094-B.

HEWITT, G. F.; HALL-TAYLOR, N. S. **Annular two-phase flow**. 1. ed. [s.l.] : Pergamon, 1970.

HEWITT, G. F.; JAYANTI, S. To churn or not to churn. **International Journal of Multiphase Flow**, *[S. l.]*, v. 19, n. 3, p. 527–529, 1993. DOI: 10.1016/0301-9322(93)90065-3.

HEWITT, G. G.; ROBERTS, D. N. **Studies of two-phase flow patterns by simultaneous x-ray and flast photography (Technical Report) | OSTI.GOV**. Harwell, England.

HILL, D. P.; WANG, D. M.; GOSMAN, A. D.; ISSA, R. I. Numerical predictionof Bubble dispersion in shear layers. *In*: THIRD INTERNATIONAL SYMPOSIUM ON MULTI-PHASE FLOW AND HEAT TRANSFER 1994, Xian, China. **Anais** [...]. Xian, China p. 110–117.

HUTCHINSON, P.; WHALLEY, P. B. A possible characterisation of entrainment in annular flow. **Chemical Engineering Science**, *[S. l.]*, v. 28, p. 974–975, 1973.

JASAK, Hrvoje. **Error Analysis and Estimation for the Finite Volume Method With Applications to Fluid Flows**. 1996. *[S. l.]*, 1996.

JAYANTI, S.; BRAUNER, Neima. CHURN FLOW. **Multiphase Science and Technology**, *[S. l.]*, v. 8, n. 1–4, p. 471–521, 1994. DOI: 10.1615/MULTSCIENTECHN.V8.I1-4.90.

JENSEN, M. K. The liquid film and the core region velocity profiles in annular two-phase flow. **International Journal of Multiphase Flow**, *[S. l.]*, v. 13, n. 5, p. 615–628, 1987. DOI: 10.1016/0301-9322(87)90039-5.

JONES, Owen C.; ZUBER, Novak. The interrelation between void fraction fluctuations and flow patterns in two-phase flow. **International Journal of Multiphase Flow**, *[S. l.]*, v. 2, n. 3, p. 273–306, 1975. DOI: 10.1016/0301-9322(75)90015-4.

KARAMI, Hamidreza; TORRES, Carlos F.; PARSI, Mazdak; PEREYRA, Eduardo; SARICA, Cem. CFD simulations of low liquid loading multiphase flow in horizontal pipelines. *In*: AMERICAN SOCIETY OF MECHANICAL ENGINEERS, FLUIDS ENGINEERING DIVISION (PUBLICATION) FEDSM 2014, **Anais** [...]. : American Society of Mechanical Engineers (ASME), 2014. DOI: 10.1115/FEDSM2014-21856.

KATAOKA, I.; ISHII, M.; NAKAYAMA, A. Entrainment and desposition rates of droplets in annular two-phase flow. **International Journal of Heat and Mass Transfer**, *[S. l.]*, v. 43, n. 9, p. 1573–1589, 2000. DOI: 10.1016/S0017-9310(99)00236-7.

LAUNDER, B. E.; SHARMA, B. I. Application of the energy-dissipation model of flow near a spinning disc. **Letters in Heat and Mass Transfer**, *[S. l.]*, v. 1, n. 2, p. 131–138, 1974.

LIN, Ruinan; WANG, Ke; LIU, Li; ZHANG, Yongxue; DONG, Shaohua. Study on the characteristics of interfacial waves in annular flow by image analysis. **Chemical Engineering Science**, *[S. l.]*, v. 212, p. 115336, 2020. DOI: 10.1016/J.CES.2019.115336.

LIU, Y.; LI, W. Z.; QUAN, S. L. A self-standing two-fluid CFD model for vertical upward two-phase annular flow. *In*: NUCLEAR ENGINEERING AND DESIGN 2011, **Anais** [...]. [s.l: s.n.] p. 1636–1642. DOI: 10.1016/j.nucengdes.2011.01.037.

MAO, Z. S.; DUKLER, A. E. The myth of churn flow? **International Journal of Multiphase Flow**, *[S. l.]*, v. 19, n. 2, p. 377–383, 1993. DOI: 10.1016/0301-9322(93)90010-R.

MCQUILLAN, K. W.; WHALLEY, P. B. Flow patterns in vertical two-phase flow. **International Journal of Multiphase Flow**, *[S. l.]*, v. 11, n. 2, p. 161–175, 1985.

MENTER, F. R. Two-equation eddy-viscosity turbulence models for engineering applications. **AIAA Journal**, *[S. l.]*, v. 32, n. 8, p. 1598–1605, 1994. DOI: 10.2514/3.12149.

MICHAELIDES, Efstathios; CROWE, Clayton T.; SCHWARZKOPF, John D. **Multiphase Flow Handbook**. 2. ed. [s.l.] : Taylor & Francis, 2015.

NIGMATULIN, R. I.; NIGMATULIN, B. I.; KHODZHAEV, Ya D.; KROSHILIN, V. E. Entrainment and deposition rates in a dispersed-film flow. **International Journal of Multiphase Flow**, *[S. l.]*, v. 22, n. 1, p. 19–30, 1996. DOI: 10.1016/0301-9322(95)00044-5.

OKAWA, Tomio; KATAOKA, Isao. Correlations for the mass transfer rate of droplets in vertical upward annular flow. **International Journal of Heat and Mass Transfer**, *[S. l.]*, v. 48, n. 23–24, p. 4766–4778, 2005. DOI: 10.1016/J.IJHEATMASSTRANSFER.2005.06.014.

OPENFOAM. **OpenFOAM: API Guide.**, 2012.

OWEN, David. An Experimental and Theoretical Analysis of Equilibrial Annular Flows. *[S. l.]*, n. April, p. 447, 1986.

PARSI, Mazdak; AGRAWAL, Madhusuden; SRINIVASAN, Vedanth; VIEIRA, Ronald E.; TORRES, Carlos F.; MCLAURY, Brenton S.; SHIRAZI, Siamack A.; SCHLEICHER, Eckhard; HAMPEL, Uwe. Assessment of a hybrid CFD model for simulation of complex vertical upward gas-liquid churn flow. **Chemical Engineering Research and Design**, *[S. l.]*, v. 105, p. 71–84, 2016. DOI: 10.1016/j.cherd.2015.10.044.

PHAM, Duc Quy Thinh; JEON, Jichan; CHOI, Sanghun. Quantitative comparison between volume-of-fluid and two-fluid models for two-phase flow simulation using OpenFOAM. **Journal of Mechanical Science and Technology**, *[S. l.]*, v. 34, n. 3, p. 1157–1166, 2020. DOI: 10.1007/s12206-020-0217-1.

REZENDE, Ricardo V. P.; ALMEIDA, Regiani A.; ULSON DE SOUZA, AntÔnio A.; SELENE, Selene M. A. A two-fluid model with a tensor closure model approach for free surface flow simulations. **Chemical Engineering Science**, *[S. l.]*, v. 122, p. 596–613, 2015. DOI: 10.1016/J.CES.2014.07.064.

ROLLINS, C. E. **Development ofMultiphase Computational Fluid Dynamics Solver in OpenFOAM**. 2018. North Carolina State University, *[S. l.]*, 2018.

ROSA, Eugenio S. **Escoamento Multifásico Isotérmico**. São Paulo: Bookman, 2012.

RUSCHE, Henrik. **Computational fluid dynamics of dispersed two-phase flows at high phase fractions**. 2003. Imperial College London (University of London), London, 2003.

SALLES, M. V. **MARCOS VINÍCIUS SALLES NUMERICAL SIMULATION OF THE VERTICAL ANNULAR GAS- LIQUID TWO-PHASE FLOW NUMERICAL SIMULATION OF THE VERTICAL ANNULAR GAS- LIQUID TWO-PHASE FLOW**. 2020. Santa Catarina State University, *[S. l.]*, 2020.

SAWAI, T.; KAJI, M.; KASUGAI, T.; NAKASHIMA, H.; MORI, T. Gas–liquid interfacial structure and pressure drop characteristics of churn flow. **Experimental Thermal and Fluid Science**, *[S. l.]*, v. 28, n. 6, p. 597–606, 2004. DOI: 10.1016/J.EXPTHERMFLUSCI.2003.09.003.

SAWANT, Pravin; ISHII, Mamoru; MORI, Michitsugu. Prediction of amount of entrained droplets in vertical annular two-phase flow. **International Journal of Heat and Fluid Flow**, *[S. l.]*, v. 30, n. 4, p. 715–728, 2009. DOI: 10.1016/J.IJHEATFLUIDFLOW.2009.03.003.

SILVEIRA NETO, Aristeu Da. **Escoamentos Turbulentos: Análise Física e Modelagem Teórica**. 1. ed. Uberlândia: Editora Composer, 2020.

STÄDTKE, Herbert. Gasdynamic aspects of two-phase flow : hyperbolicity, wave propagation phenomena, and related numerical methods. *[S. l.]*, p. 273, 2006.

TAITEL, Yehuda; BARNEA, Dvora; DUKLER, A. E. Modelling flow pattern transitions for steady upward gas-liquid flow in vertical tubes. **AIChE Journal**, *[S. l.]*, v. 26, n. 3, p. 345–354, 1980. DOI: 10.1002/aic.690260304.

TAITEL, Yemada; DUKLER, A. E. A model for predicting flow regime transitions in horizontal and near horizontal gas-liquid flow. **AIChE Journal**, *[S. l.]*, v. 22, n. 1, p. 47–55, 1976. DOI: 10.1002/aic.690220105.

TEKAVČIČ, Matej; KONČAR, Boštjan; KLJENAK, Ivo. Simulation of flooding waves in vertical churn flow. **Nuclear Engineering and Design**, *[S. l.]*, v. 299, p. 214–224, 2016. DOI: 10.1016/j.nucengdes.2015.07.016.

TEKAVČIČ, Matej; KONČAR, Boštjan; KLJENAK, Ivo. Three-dimensional simulations of liquid waves in isothermal vertical churn flow with OpenFOAM. **Experimental and Computational Multiphase Flow**, *[S. l.]*, v. 1, n. 4, p. 300–306, 2019. DOI: 10.1007/s42757-019-0029-7. Disponível em: https://link.springer.com/article/10.1007/s42757-019-0029-7. Acesso em: 20 jun. 2021.

THAKER, Jignesh; BANERJEE, Jyotirmay. CFD SIMULATION OF TWO-PHASE FLOW PHENOMENA IN HORIZONTAL PIPELINES USING OPENFOAM. *In*: 40TH NATIONAL CONFERENCE ON FLUID MECHANICS AND FLUID POWER 2013, **Anais** [...]. [s.l: s.n.]

TOCCI, Francesco. **Assessment of a hybrid VOF two-fluid CFD solver for simulation of gas-liquid flows in vertical pipelines in OpenFOAM**. 2016. *[S. l.]*, 2016. Disponível em: https://www.politesi.polimi.it/handle/10589/127961.

TOMIYAMA, Akio; KATAOKA, Isao; ZUN, Iztok; SAKAGUCHI, Tadashi. Drag Coefficients of Single Bubbles under Normal and Micro Gravity Conditions. **JSME International Journal Series B Fluids and Thermal Engineering**, *[S. l.]*, v. 41, n. 2, p. 472–479, 1998. DOI: 10.1299/JSMEB.41.472.

VAZE, M. J.; BANERJEE, J. Experimental visualization of two-phase flow patterns and transition from stratified to slug flow. **Proceedings of the Institution of Mechanical Engineers, Part C: Journal of Mechanical Engineering Science**, *[S. l.]*, v. 225, n. 2, p. 382–389, 2011. DOI: 10.1243/09544062JMES2033.

VERSTEEG, H. K.; MALALASEKERA, W. An Introduction to Computational Fluid Dynamics: The Finite Volume Method. *In*: EDUCATION, Pearson (org.). 1. ed. Harlow, EN.

WALLIS, Graham B. **One-dimensional two-phase flow**. 1. ed. New York: McGraw-Hill, 1969.

WALTRICH, Paulo J.; FALCONE, Gioia; BARBOSA, Jader R. Axial development of annular, churn and slug flows in a long vertical tube. **International Journal of Multiphase Flow**, *[S. l.]*, v. 57, p. 38–48, 2013. DOI: 10.1016/J.IJMULTIPHASEFLOW.2013.06.008.

WANG, Ke; BAI, Bofeng; MA, Weimin. A model for droplet entrainment in churn flow. **Chemical Engineering Science**, *[S. l.]*, v. 104, p. 1045–1055, 2013. DOI: 10.1016/J.CES.2013.10.028.

WANG, Ke; YE, Jing; BAI, Bofeng. Entrained droplets in two-phase churn flow. **Chemical Engineering Science**, *[S. l.]*, v. 164, p. 270–278, 2017. DOI: 10.1016/J.CES.2017.02.028.

WARDLE, Kent E.; WELLER, Henry G. Hybrid multiphase CFD solver for coupled dispersed/segregated flows in liquid-liquid extraction. **International Journal of Chemical Engineering**, *[S. l.]*, v. 2013, n. 1, 2013. DOI: 10.1155/2013/128936.

WHALLEY, P. B.; HEWITT, G. F. **The correlation of liquid entrainment fraction and entrainment rate in annular two-phase flow: Whalley, P. B: Amazon.com: Books**. Harwell.

WILCOX, David C. **Turbulence modeling for CFD**. 3. ed. California.

WOLF, A.; JAYANTI, S.; HEWITT, G. F. Flow development in vertical annular flow. **Chemical Engineering Science**, *[S. l.]*, v. 56, n. 10, p. 3221–3235, 2001. DOI: 10.1016/S0009-2509(00)00546-7.

ZABARAS, G. J.; DUKLER, A. E. Countercurrent gas-liquid annular flow, including the flooding state. **AIChE Journal**, *[S. l.]*, v. 34, n. 3, p. 389–396, 1988. DOI: 10.1002/aic.690340305.

ZHANG, Zhennan; WANG, Zhiyuan; LIU, Hui; GAO, Yonghai; LI, Hao; SUN, Baojiang. Experimental study on entrained droplets in vertical two-phase churn and annular flows. **International Journal of Heat and Mass Transfer**, *[S. l.]*, v. 138, p. 1346–1358, 2019. DOI: 10.1016/J.IJHEATMASSTRANSFER.2019.04.126.

ZHAO, Jingjing; TAO, Hanzhong; CHENG, Jianjie; LI, Wei; FU, Lijun. A numerical analysis of the characteristics of interfacial waves on the onset of flooding in an inclined pipe. **International Journal of Multiphase Flow**, *[S. l.]*, v. 132, 2020. DOI: 10.1016/j.ijmultiphaseflow.2020.103400.

APPENDIX A – Wall lubrication models in churn flow

Figure 35 and Figure 36 show the void fraction and pressure gradient, respectively, in churn flow, in simulations using no wall lubrication (NWL), and the Tomiyama and Antal models for this force. All simulations were performed with a maximum Courant number of 0.125, modelling turbulence with laminar water and air with the $k - \omega$ SST model, and the drag coefficients with the Schiller and Naumann model. The x-axis was limited to the interval between 2 and 5 seconds to provide a better visualization. It can be seen that the wall lubrication forces barely influence the flow. However, they bring some instabilities to the simulation, causing it to diverge before reaching 5 seconds of simulation.

Figure 35 – Void fraction in churn flow as function of time for the different wall lubrication models.

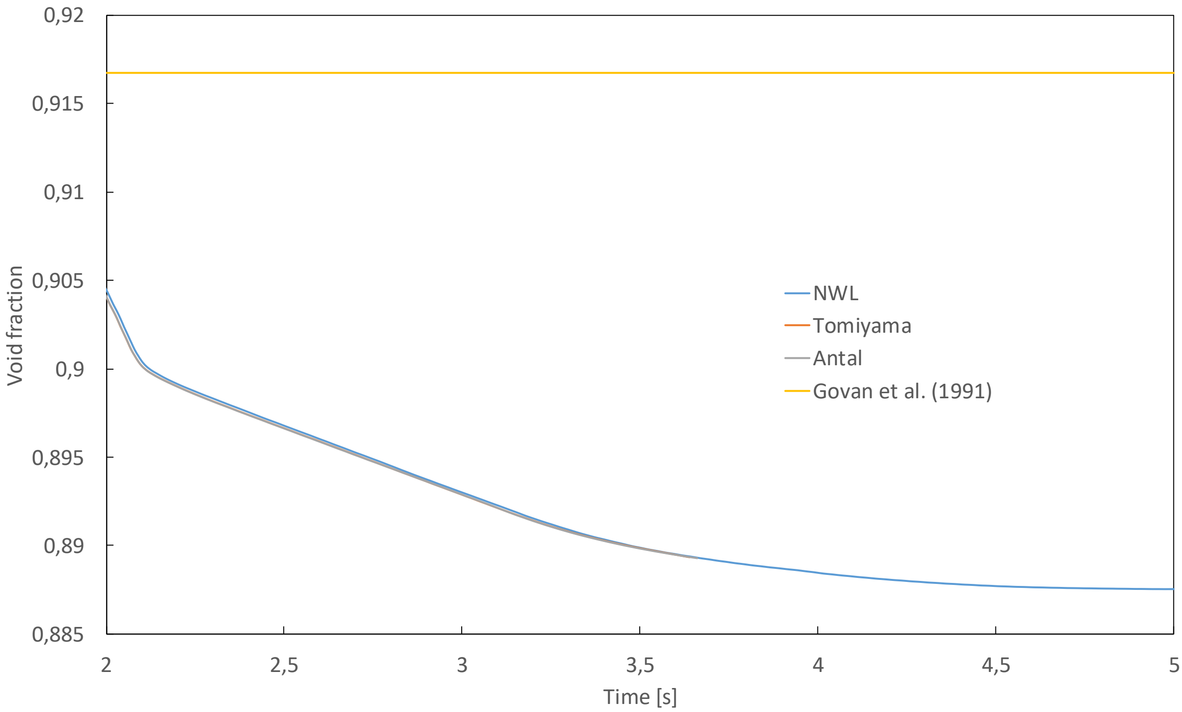

Source: The author (2022).

Figure 36 – Pressure gradient in churn flow as function of time for the different wall lubrication models.

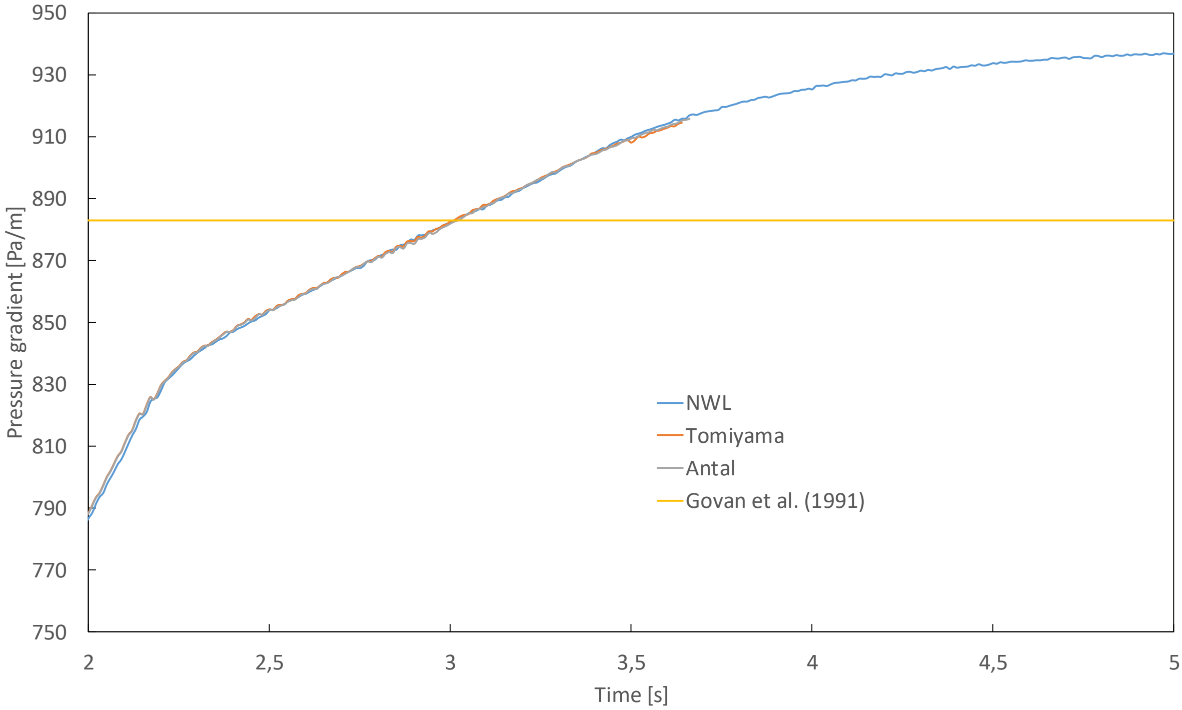

Source: The author (2022).

APPENDIX B – Drag coefficient models in churn flow

Figure 37 and Figure 38 show the void fraction and pressure gradient, respectively, in churn flow, in simulations using no wall lubrication (NWL), and the Tomiyama and Antal models for this force. All simulations were performed with a maximum Courant number of 0.125, modelling turbulence with laminar water and air with the $k - \omega$ SST model, and no wall lubrication. The influence of the drag coefficient models is also very small, although more significant than the wall lubrication models. These models also cause the divergence of the solution before reaching 5 seconds.

Figure 37 – Void fraction in churn flow as function of time for the different drag coefficient models.

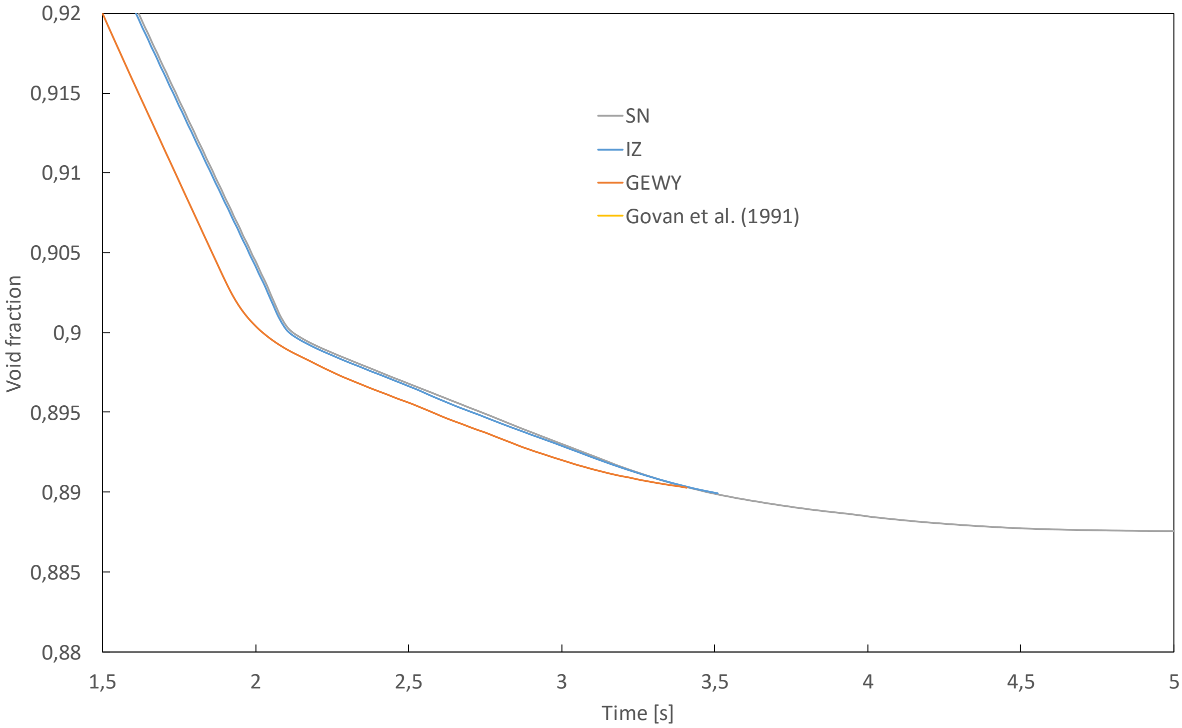

Source: The author (2022).

Figure 38 – Pressure gradient in churn flow as function of time for the different drag coefficient models.

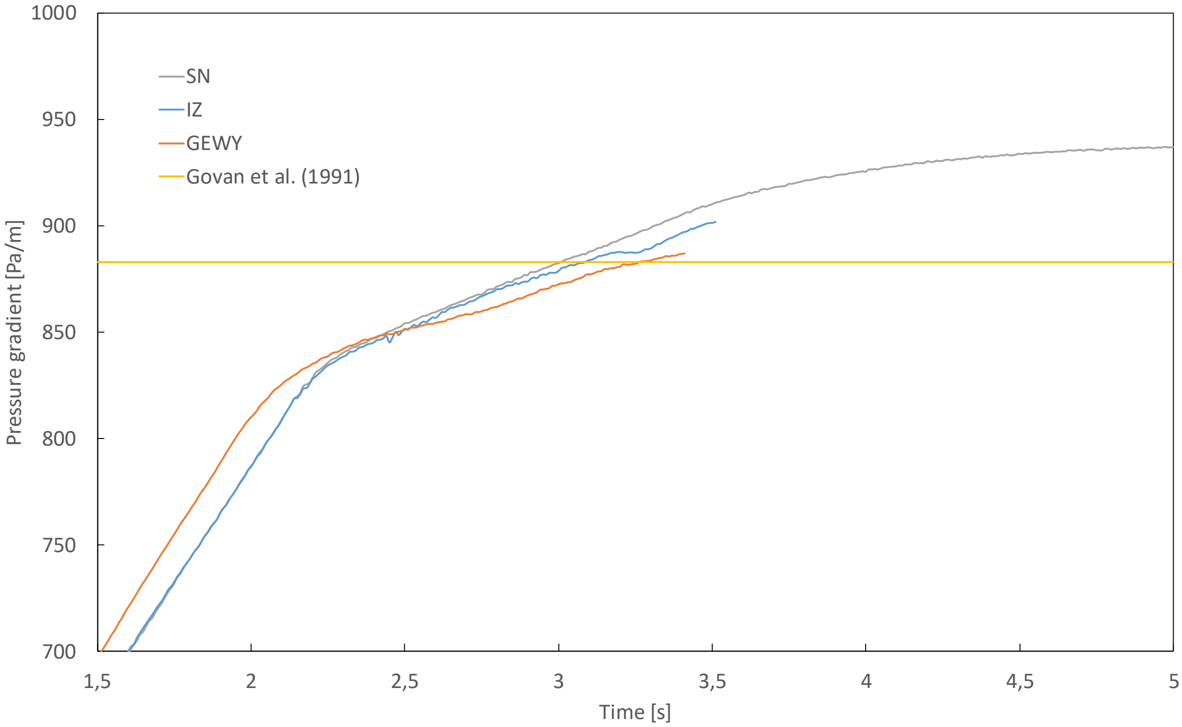

Source: The author (2022).